

GALACTIC NUCLEI IN THE NEAR-IR
PROBING THE IMPACT OF THE CENTRAL ENGINES
ON THEIR HOST GALAXIES

INAUGURAL-DISSERTATION

zur
Erlangung des Doktorgrades
der Mathematisch-Naturwissenschaftlichen Fakultät
der Universität zu Köln



vorgelegt von

KONSTANTINOS MARKAKIS
aus Athen, Griechenland

Köln 2016

Berichterstatter:

Prof. Dr. Andreas Eckart
Prof. Dr. J. Anton Zensus

Tag der letzten mündlichen Prüfung: 21. October 2015



Zusammenfassung

Galaxien bilden auf großen Skalen die Grundbausteine des Universums, gleichzeitig sind sie auf individueller Ebene sehr komplizierte Objekte. Es kann eine große Vielfalt bzgl. Morphologie, Farbe, Größe, sowie anderen allgemeinen Eigenschaften beobachtet werden. Das zurzeit vorherrschende Λ kalte dunkle Materie (Λ CDM) kosmologische Modell nimmt eine hierarchische Bildung solcher Strukturen an. In diesem Rahmen werden lichtschwächere und schneller rotierende elliptische Galaxien aus der Verschmelzung von Spiralgalaxien, die durch Rotation aufrecht erhalten werden und eine hohe Gasdichte haben, erzeugt. Die elliptische Struktur wird dann dynamisch durch eine Kombination von Druck, der durch die zufällige Bewegung der Sterne verursacht wird, und der geordneten Rotationsbewegung der Sterne auf Bahnen, die ein Relikt der Stammgalaxien sind, zusammengehalten. Leuchtschwache elliptische Galaxien fügen sich dann zusammen um gigantische, langsam rotierende, "rote und tote" elliptische Galaxien zu erzeugen, die dynamisch vom Druck der zufälligen Bewegung der überwiegend alten Sterne getragen werden. Während des Zusammenpralls zweier (oder mehrerer) Galaxien werden Prozesse initiiert, die, neben der stochastischen Neuordnung der Sternbahnen, eine wichtige Rolle bei der weiteren Entwicklung spielen. Am Ende dieses Zusammentreffens entstehen ein supermassives Schwarzes Loch (SMBH) Paar und möglicherweise SMBH Recoils (Rückstöße). Beide Ereignisse haben einen beachtenswerten Einfluss auf den zentralen Bereich der Galaxien nach dem Wechselwirkungsprozess. Außerdem können Drehmomente der Gezeiten den Drehimpuls der interstellaren Materie aus den ursprünglichen Galaxien senken, wodurch eine Bewegung zum Zentrum und damit intensive Starbursts hervorgerufen werden. Gleichzeitig ist dieser Effekt sehr wirksam, um das zentrale Schwarze Loch anzutreiben. Dieses Phänomen wird als aktiver galaktischer Kern (AGN) bezeichnet. Ein AGN

kann massive Ausströmungen von Energie (d.h. AGN feedback) in der Form von Strahlung oder mechanischer Arbeit (z.B. Winde und Jets) produzieren. Diese intensiven Strahlungsfelder können einen negativen (z.B. Erliegen der Sternentstehung im Kern) oder positiven Effekt (z.B. Jet-induzierte Sternentstehung) haben.

In dieser Arbeit beschäftige ich mich mit der Analyse von hochauflösenden Daten aus dem nahen Infrarot (NIR), für welche adaptive Optik (AO) benutzt wurde. Diese Daten von den Objekten NGC3718 und NGC5128 wurden vom Subaru Teleskop mit dem High-Contrast Coronagraphic Imager for Adaptive Optics (HiCIAO) Instrument aufgenommen.

NGC3718 ist ein spannendes Objekt. Seine morphologischen Eigenschaften weisen auf eine Klassifikation als Polarring Galaxie hin, die einen seltenen Fall einer Galaxienkollision bildet. Gleichzeitig besitzt sie einen AGN schwacher Helligkeit (LLAGN). Die Analyse, die hier präsentiert wird, zeigt die wahrscheinliche Existenz eines SMBH Recoils. Diese Erkenntnis wird von den Ergebnissen früherer Arbeiten unterstützt. Die Behauptung, dass ein SMBH Recoil präsent ist, wird von den beobachteten räumlichen Verschiebungen der Nahinfrarot- und Radiostrahlung, der relativen Verschiebung zwischen der breiten und schmalen $H\alpha$ Linien, als auch vom Anteil an "verlorenem Licht" in der zentralen Region (d.h. ~ 200 pc), unterstützt. In einem Unterfangen alle diese Befunde in einem physikalisch konsistenten Bild zusammenzufassen, werde ich eine mögliche Interpretation dieser Ergebnisse darlegen.

NGC5128 ist ebenfalls ein sehr interessantes Objekt, da es die leuchtkräftige Radioquelle Centaurus A (Cen A) beherbergt. Hier beschäftige ich mich mit der Analyse einer Region in der Nähe von der nördlichen mittleren Keule (NML) des Cen A Jets, welche einen Abstand von ~ 15 kpc zum Zentrum der Galaxie besitzt. In dieser Region fand vermutlich vor $\sim 10 - 15$ Millionen Jahren Jet-induzierte Sternentstehung statt, die zur Erzeugung von jungen blauen Sternen in OB-Assoziationen geführt hat. Statistische und photometrische Analysen der hochaufgelösten Bilder der Region zeigen die Existenz von Überriesen, deren geschätzte Alter mit dem der Jet-induzierten Sternentstehung übereinstimmen.

In dieser Arbeit betone ich außerdem das große Potenzial hochauflösender, bodengebundener NIR Beobachtungen, um unseren Kosmos zu erforschen. Im Besonderen bezieht sich dies auf physikalische Prozesse in inneren Regionen naher Galaxien oder das Auflösen extragalaktischer dichter Sternpopulationen (z.B. OB-Assoziationen) in individuelle Sterne jenseits unserer Lokalen Gruppe (LG).



Abstract

Galaxies are the building blocks of the large-scale structures of the Universe, but they are also very complicated structures at an individual level. They are observed to have a variety of morphologies, colors, sizes, and general properties. According to the, currently main-stream, Λ cold dark matter (Λ CDM) cosmological model, structures in the Cosmos grow hierarchically. Within this framework, gas-rich, rotationally supported spiral/disk galaxies merge to form the fainter, rapidly rotating ellipticals, objects which are dynamically supported by a combination of pressure due to random motions of stars and ordered rotational motions of the stars from the relic disks of the progenitor galaxies. Fainter elliptical galaxies then merge to form giant, slowly rotating, “red and dead” ellipticals, which are dynamically supported by the pressure of the highly randomized motions of their, mostly, old stars. Galaxy mergers, however, do much more than randomizing the orbits of stars, as they also introduce a variety of important implications to galaxy evolution. The “end story” of mergers is, inevitably, to create supermassive black hole (SMBH) binaries and, possibly, SMBH recoils, both of which can transform the central regions of the remnants. Moreover, tidal torques during mergers can remove angular momentum from the gas of the progenitor galaxies and drive it towards the center, a process which can initiate intense central starbursts, while it is also a very effective way to “turn on” their central engines, in a phenomenon known as an active galactic nucleus or AGN. An AGN, in turn, can produce massive energy outflows (i.e. AGN feedback) both in the form of mechanical energy (e.g. winds and jets), as well as, in the form of intense radiation fields, which can affect the evolution of a galaxy, either in a negative (e.g. quenching nuclear star formation) or in a positive way (e.g. jet-induced star formation).

In this thesis, I present the case studies of two objects, namely, NGC3718 and NGC5128, using near-infrared (NIR), high resolution, adaptive optics (AO) assisted data taken with the Subaru telescope and the High-Contrast Coronagraphic Imager for Adaptive Optics (HiCIAO) instrument.

NGC3718 is an exciting object. Its morphological properties point towards a classification as a polar ring galaxy, which is, likely, the product of a rare case of a galaxy merger, while it is also a low luminosity AGN (LLAGN). The analysis presented here, reveals strong indications for the presence of an SMBH recoil in NGC3718, which is further supported by results from previous studies. Evidence that an SMBH recoil is present include the observed NIR and radio emission spatial offsets, a candidate small-scale X-shaped radio source, an amount of “missing light” in its central region (i.e. ~ 200 pc), and the relative shift between its broad and narrow $H\alpha$ lines. In an effort to incorporate all these findings into one physically consistent scheme, I extensively discuss a possible interpretation of these results.

NGC5128 is also a very interesting object, since it is the host of the powerful radio source Centaurus A (Cen A). Here, I present the analysis of a field located near the northern middle lobe (NML) of the Cen A jet, at a distance of ~ 15 kpc from the center of the galaxy. This region has long been suspected to have undergone a jet-induced star formation $\sim 10 - 15$ Myr ago, which created young blue stars arranged in OB associations. Statistical and photometric analysis of high resolution images of the region reveals the presence of supergiants, with estimated ages consistent with the age of the jet-induced star formation.

Finally, throughout this work I underline the great potential of high resolution, ground-based NIR observations in exploring our Cosmos, either regarding the physical processes that occur in the central regions of nearby galaxies, or in resolving extra-galactic dense stellar populations (e.g. OB associations) into individual stars in galaxies beyond our Local Group (LG).



Contents

Contents	v
1 Introduction	1
1.1 General introduction	1
1.2 Galaxy evolution	3
1.2.1 Large-scale structures	3
1.2.2 Galaxy mergers	5
1.2.3 Active Galactic Nuclei	8
1.3 Observations	11
1.3.1 Observing in the NIR	11
1.3.2 Ground-based AO assisted observations	13
1.4 Dissertation outline	16
1.4.1 Preamble of chapter 2	17
1.4.2 Preamble of chapter 3	17
1.4.3 Preamble of chapter 4	18
2 NGC3718: Diaries of a recoiled SMBH?	19
2.1 Introduction to chapter 2	19
2.2 Observations and data used in chapter 2	22
2.2.1 Subaru data of NGC3718	22
2.2.2 e-Merlin data of NGC3718	24
2.3 Data processing	25
2.3.1 Locating the center of the stellar bulge	25
2.3.2 Pivot and subtract operation	27

2.3.3	Evaluating the centering process	27
2.3.4	Matching the angular resolution and calibrating the flux	30
2.3.5	Astrometric uncertainties	31
2.4	The NIR color maps	31
2.4.1	Decomposing the NIR light	34
2.4.2	The e-Merlin radio map	35
2.5	Scaling relations and classification of NGC3718	40
2.5.1	To bulge or not to bulge?	40
2.5.2	A light “deficit” or a σ “surplus”?	43
2.5.3	Core or coreless?	46
2.6	Observational evidence for an SMBH recoil	48
2.7	Discussion of chapter 2	51
2.7.1	Galaxy evolution and the formation of cores	51
2.7.2	Polar ring galaxies formation	52
2.7.3	Building the big picture	54
2.7.4	An SMBH recoil?	56
3	Cen A: Supergiants in a region of jet-induced star formation?	59
3.1	Introduction to chapter 3	59
3.2	Observations and data used in chapter 3	61
3.2.1	Subaru data of Cen A	61
3.2.1.1	Subaru photometric calibration	61
3.2.2	HST data of Cen A	61
3.3	Locating the FoV	62
3.3.1	Testing the Subaru photometric calibration	63
3.4	Data processing	64
3.4.1	Statistical analysis of the NIR $> 3\sigma$ signal	64
3.4.2	Photometric calibration of the NIR $> 3\sigma$ detections	67
3.4.3	An extra-galactic supergiant or a galactic dwarf?	68
3.4.3.1	Supergiant	70
3.4.3.2	Dwarf	70
3.4.4	What about the B and C HST stars?	71
3.5	Discussion of chapter 3	72
3.5.1	Resolving extra-galactic stars beyond our LG	74
4	Final Remarks	77
4.1	General outline	77
4.2	Summary of chapter 2	79
4.3	Summary of chapter 3	80
A	Appendix A – On the Subaru data reduction	83
B	Appendix B – On the influence of the dust lane	87

<i>CONTENTS</i>	vii
C Appendix C – On the alignment of the z-J bands	89
D Appendix D – On the position of the e-Merlin radio map	91
Bibliography	93
List of Figures	105
List of Tables	110
Acronyms	111
Acknowledgements	115
Erklärung	119

Introduction

1.1 General introduction

Our mainstream perception for the creation of the Cosmos converges to the view that the Universe was created about ~ 13.8 billion years ago in a Big Bang¹. This scenario involves an infinitesimally hot, infinitesimally small, and infinitesimally dense point—a singularity—that expands and cools, in the form of a super-hot primordial plasma. Within the first second of the life of the Universe, protons, neutrons, electrons, and photons constitute this elementary particles “soup”, while within the first few minutes the temperature is sufficiently low to allow the formation of atomic nuclei, mainly of hydrogen (^1H) and helium isotope helium-4 (^4He), along with trace amounts of deuterium (^2H or D), helium isotope helium-3 (^3He), and lithium isotope lithium-7 ^7Li , in a process known as primordial nucleosynthesis.

After ~ 378.000 yr the Universe has cooled down enough to allow protons and electrons to form neutral hydrogen, in an epoch called recombination. Shortly after, the photons were scattered by matter for the last time and were completely free to travel through the Universe, a moment known as the photon decoupling. The cosmic microwave background (CMB) radiation that we observe today is the relic radiation of this event. This process is briefly summarized in the upper figure 1.1.

The tiny initial anisotropies in the temperature of the CMB (i.e. of the order of

¹Like a part of a cosmic irony, this name is attributed to Sir Fred Hoyle, perhaps the biggest opponent of the theory. He coined the term “the Big Bang” during a BBC radio broadcast in 1950.

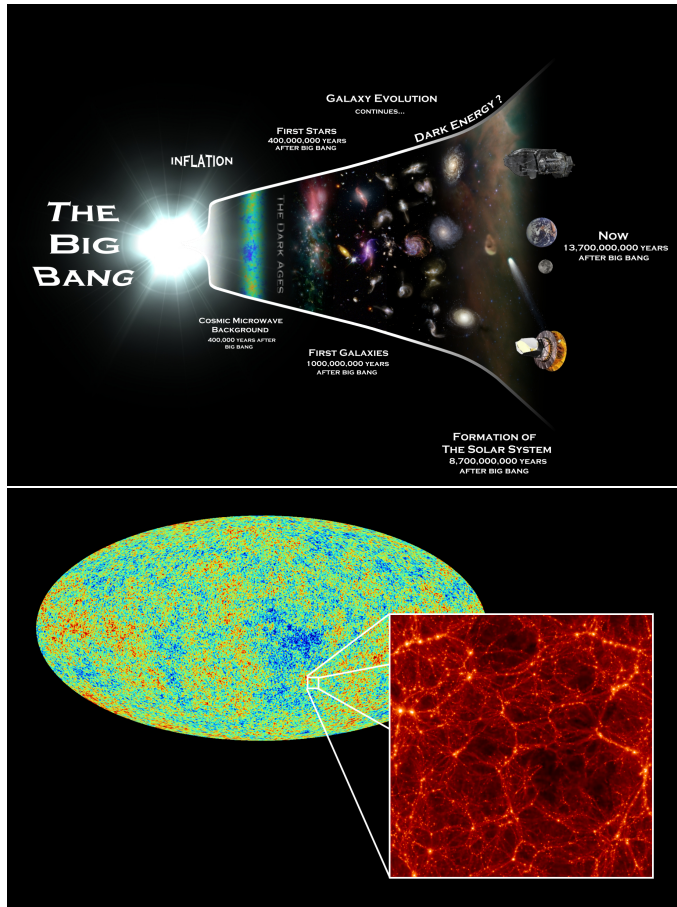


Figure 1.1: Top: A brief history of the Universe from the Big Bang to the present day. Image credit: Rhys Taylor (Cardiff University). Bottom: The CMB temperature map from the WMAP experiment with a small region of it magnified to demonstrate how the initial CMB anisotropies result in the Cosmic Web. Image credit: Berkeley Lab.

$\Delta T T^{-1} \sim 10^{-5}$, demonstrated by the red, yellow, and blue colored regions in the bottom image of figure 1.1) reflect matter density variations, which are amplified by gravity to give rise to the complex large-scale structures that we observe today (see figure 1.3)–in the form of galaxy groups, clusters, and superclusters, organized in sheets, walls, and filaments, which are separated by immense voids– creating what we refer to as the cosmic web (see the zoomed-in region in the bottom image of figure 1.1 and the middle image of figure 1.3).

During the transition from the initial density variations in the CMB to the cosmic web, structures grow hierarchically (e.g. [White and Rees, 1978](#)). Relatively simply put, within

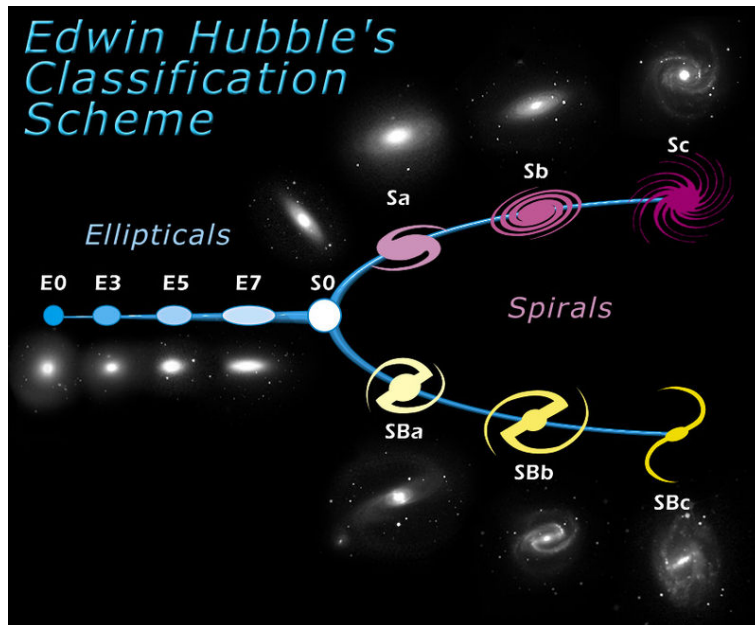


Figure 1.2: The Hubble tuning fork. Galaxy evolution is implied if one attempts to “read” this figure from the right (late-type spiral galaxies) to the left side (early-type elliptical galaxies). Image credit: Sloan Digital Sky Survey (SDSS)

the Λ cold dark matter (Λ CDM) model of structure formation, gas-rich spiral/disk galaxies fall into large dark matter (DM) gravitational potential wells and through a combination of minor and major mergers they eventually form gas-poor, “red and dead”, giant elliptical galaxies. In this sense, the famous Hubble’s tuning fork diagram represents a sequence of galaxy evolution (see figure 1.2).

1.2 Galaxy evolution

1.2.1 Large-scale structures

The basic idea of the current structure formation theory (i.e. Λ CDM) is that regions of the CMB that have higher-than-average matter density expand at a slower pace than regions with average (or less-than-average) matter density because of gravity. Self-consistently, regions that start with lower density expand a little faster. But denser regions are also more massive regions, with DM being their dominant gravity component. This way, the more massive DM halos gravitationally attract the less massive ones, clustering up in a hierarchical way, while the baryonic matter that is embedded in them loses its (kinetic) energy via radiation, cools, and falls freely towards their centers, where it eventually forms rotationally supported disk-like galaxies (e.g. Primack, 2015). This process is known as gravitational collapse, during which the first stars are formed whenever the gas clumps

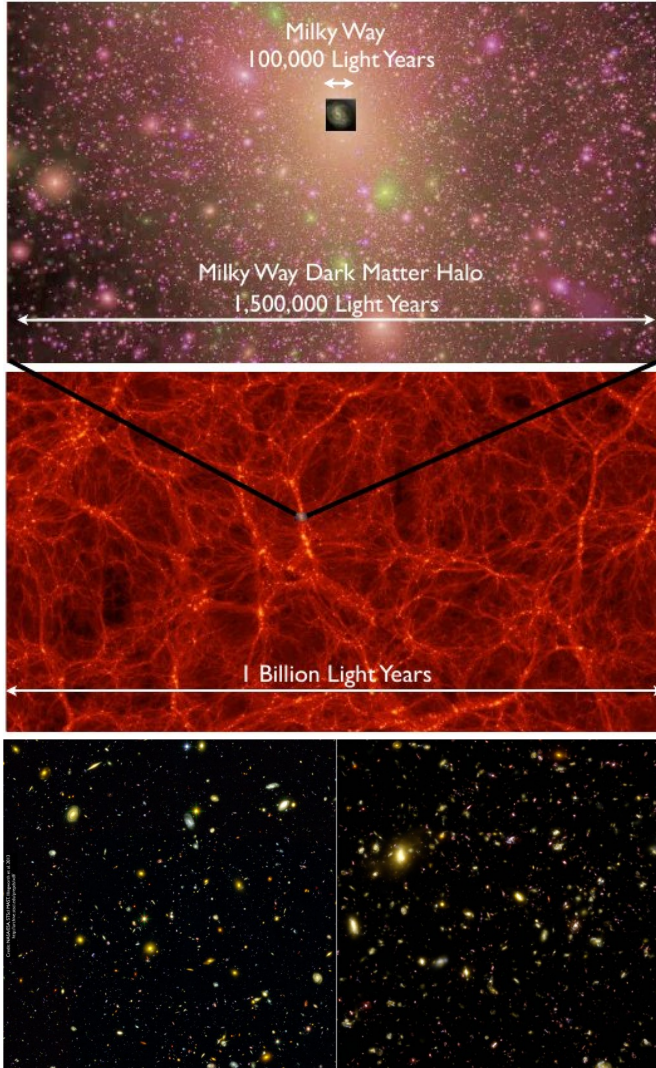


Figure 1.3: Top: A large Milky Way-like spiral galaxy has a disk $\sim 100,000$ light years across and it is very small compared to its DM halo (image from the Aquarius DM simulation [Springel et al. \(2008\)](#)). Middle: The DM halo of such a galaxy is very small compared to the large-scale cosmic web (image from the Bolshoi simulation [Klypin et al. \(2011\)](#)). Bottom: Real versus synthetic Hubble Space Telescope (HST) Ultra Deep Field from [Vogelsberger et al. \(2014b\)](#). Left: HST eXtreme Deep Field image with thousands of galaxies. Right: A similar sight-line through the Illustris Simulation of galaxy formation showing that current simulations produce galaxies with colors and shapes broadly similar to observed ones.

become more massive than the Jeans-mass (i.e. $\sim 10^3 M_{\odot}$) of that era (e.g. [Bromm et al., 2002](#)).

A number of cosmological simulations, such as the Bolshoi (Klypin *et al.*, 2011) and the Illustris (Vogelsberger *et al.*, 2014a) simulations, successfully reproduced many of the observed large-scale properties of the Universe (see figure 1.3), showing that the Λ CDM model provides an accurate physical description of structure formation on these scales. For example, the Illustris simulation (e.g. Vogelsberger *et al.*, 2014b; Torrey *et al.*, 2015) produced $\sim 40 \times 10^3$ galaxies in a volume of $\sim 106.5 \text{ Mpc}^3$ at $z=0$, with realistic galaxy number density, colors, sizes, and morphologies² (see bottom figure 1.3).

Moreover, simulations on smaller scales have also produced very important results. Attempts like the Aquarius simulation (Springel *et al.*, 2008), aimed at studying the structure and substructure of a Milky Way-size DM halo, made specific predictions about e.g. the kinematics of satellite galaxies within such a DM halo, while the ERIS (Guedes *et al.*, 2011) simulation successfully created a realistic Milky Way-type spiral galaxy. These efforts clearly demonstrate that the Λ CDM model can, in principal, provide an accurate description for structure formation also on smaller scales, making it the preferred scenario for galaxy formation.

1.2.2 Galaxy mergers

As it is evident so far, the Λ CDM cosmological model can describe the Universe acceptably accurately, at least, on several different scales and, consequently, the hierarchical growth of structures makes the merger hypothesis (Toomre, 1977) for galaxy formation an inseparable part of the big picture. What the merger hypothesis states is that major mergers between spiral galaxies can result in elliptical galaxies (see figure 1.4), an idea that started to gain ground (e.g. Barnes and Hernquist, 1992) when detailed observations of recent (candidate) merger remnants (e.g. Schweizer, 1982; James *et al.*, 1999) and of shells and/or tidal features around ellipticals (Malin and Carter, 1980; Schweizer, 1980) were conducted.

Early studies of surface brightness profiles of elliptical galaxies (e.g. Kormendy, 1985) showed that a typical elliptical galaxy's surface brightness profile could not be described simply by a uniform $\propto r^{1/4}$ law (de Vaucouleurs, 1948). Interior to $\sim 1 \text{ kpc}$, the surface brightness profile deviated from the $\propto r^{1/4}$ law fitted to its outer part, being either above³ or below⁴ from the outer profile's fit inward extrapolation. The same trend remained even when Sérsic (1968) functions began to replace the De Vaucouleurs law as the standard tool to model surface brightness profiles (Caon *et al.*, 1993), as shown in figure 1.5.

Faber *et al.* (1997) showed that the presence of extra or missing light in the nuclear profile correlates very well with other global properties of elliptical galaxies. Coreless ellipticals tend to rotate more rapidly, have diskly isophotes, and higher ellipticities, while

²In the local Universe (i.e. $z=0$) there are $\sim 60\%$ spiral, $\sim 20\%$ lenticular, $\sim 15\%$ elliptical, and $\sim 5\%$ irregular galaxies (Combes *et al.*, 2002).

³In this case they are called “extra light”, “cusp”, “disky”, or “coreless” ellipticals.

⁴In this case they are called “missing light”, “boxy”, or “core” ellipticals.

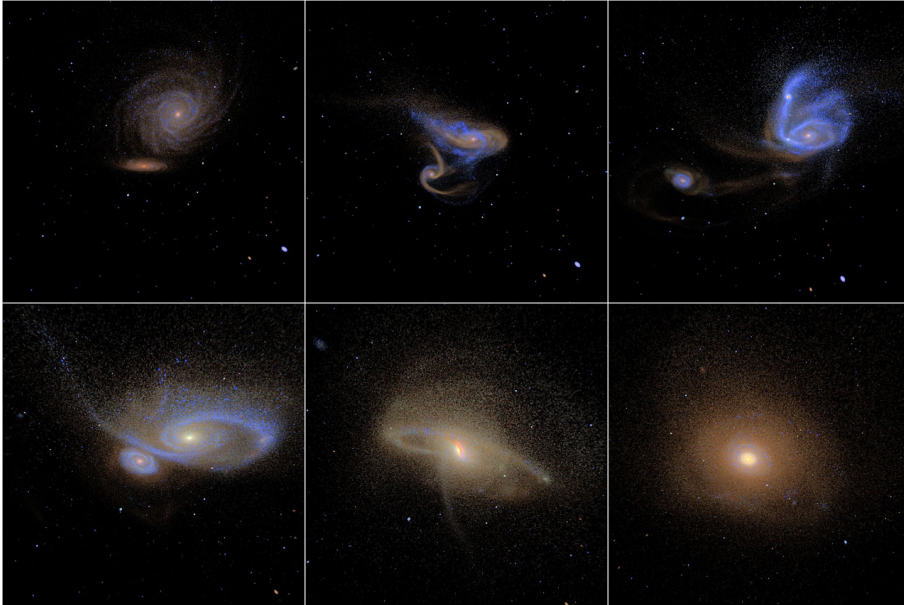


Figure 1.4: An illustration demonstrating how disk galaxies merge to form an elliptical galaxy. The entire formation process takes $\sim 2 - 3$ Gyr to complete. Image credit: P. Jons-son (Harvard-Smithsonian Center for Astrophysics, USA), G. Novak (Princeton University, USA), and T.J. Cox (Carnegie Observatories, Pasadena, Calif., USA).

core ellipticals generally rotate slowly, have boxy isophotes, and lower ellipticities. This split in the properties of the elliptical galaxies led several authors (e.g. [Faber *et al.*, 1997](#); [Kormendy, 1999](#)) naturally to the idea that disk galaxies, rapidly rotating, coreless ellipticals are the direct products of gas-rich (or “wet”) mergers, during which tidal torques (e.g. [Barnes and Hernquist, 1996](#)) drive the gas of the progenitor spiral galaxies towards the centers of the newly formed galaxies, triggering intense central starbursts (e.g. [Mihos and Hernquist, 1996](#)) and rapid supermassive black hole (SMBH) growth (e.g. [Di Matteo *et al.*, 2005](#)). Similarly, boxy, slowly rotating, core ellipticals were formed by the subsequent dissipationless (or “dry”) re-mergers of two or more (initially coreless) fainter ellipticals. However, this posed a serious problem. Nearly all numerical experiments showed that the shapes of the light profiles should be preserved in dissipationless mergers, at least, to a first order (e.g. [Boylan-Kolchin *et al.*, 2005](#)). So, if core ellipticals should look like up-scaled versions of coreless ellipticals, why do they have cores and how did these form?

A first glimpse at a potential answer to the above question came from another old idea. [Begelman *et al.* \(1980\)](#) first suggested that a coalescing binary of SMBHs in a dissipationless galaxy merger can stall at radii larger than the radii at which gravitational waves can efficiently remove energy and merge the system. This is widely known as the last parsec problem. It was noted that a significant amount of gas (e.g. the available nuclear gas in a

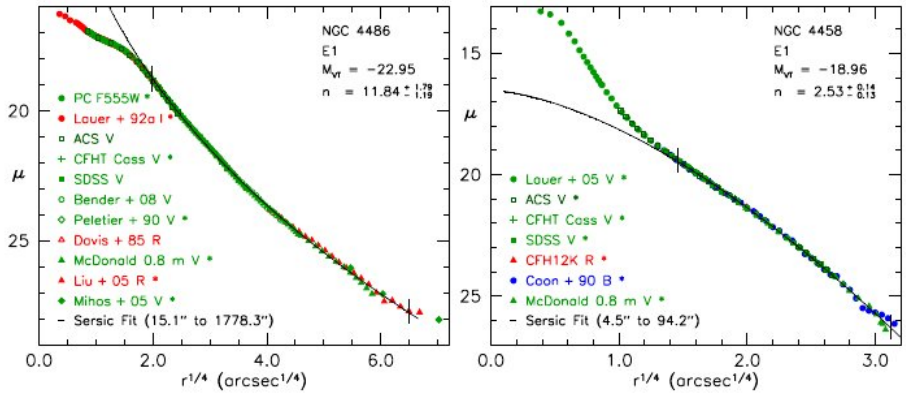


Figure 1.5: Reproduction of figure 1 from [Kormendy \(2009\)](#). Major-axis surface brightness profiles of Virgo ellipticals NGC4486 (left) and NGC4458 (right). The black curve indicates a [Sérsic \(1968\)](#) fit on the outer part of the profile (between the vertical black lines). NGC4486 is a core galaxy, since the fitted function on the outer profile overestimates the data when it is inwardly extrapolated, while NGC4458 is a coreless galaxy, since the inward extrapolation of the outer profile’s fit underestimates the data in the inner region.

wet merger) can provide an effective source of drag to overcome this problem (e.g. [Escala et al., 2005](#)), but in the case of dry mergers, due to the absence of sufficient amounts of nuclear gas, the binary may remain stalled for longer and it will eventually harden by scattering stars at larger radii instead. During this process (known as SMBH “scouring”), the central stellar density is reduced (e.g. [Merritt, 2006](#)). However, once the SMBH binary enters the final approach phase (i.e. in sub-parsec scales), it will shrink further mainly through gravitational wave emission, which—in a realistic case of random SMBH masses, spin magnitudes, and orientations of the two binary members—will likely be anisotropic. As a result, upon the binary coalescence a momentum will be induced on the newly formed SMBH, which, in turn, will recoil (e.g. [Bekenstein, 1973](#); [Fitchett and Detweiler, 1984](#); [Favata et al., 2004](#)) at a velocity that can be comparable to the host galaxy’s escape velocity. If the recoil velocity is smaller than the escape velocity of its host galaxy, the SMBH will oscillate about its core for a period of time and it will slowly decay back to the center (e.g. [Sijacki et al., 2011](#); [Blecha et al., 2011](#); [Komossa, 2012](#)), dumping its motion via dynamical friction against the surrounding medium, while further reducing the central stellar density. Such a process was simulated by [Gualandris and Merritt \(2008\)](#), who estimated that a combination of a pre-coalescence SMBH binary and a subsequent SMBH recoil can remove as much as $\sim 5 M_{BH}$ of central stellar mass, providing a framework to explain the formation of the observed cores.

Major mergers, however, are not the only “flavor” of galaxy collisions. Nowadays, major mergers are considered to be mergers of galaxies with mass ratios of $\sim (1 - 4.5) : 1$. Galaxy mergers with mass ratios of $\sim (1 - 2) : 1$ can directly produce slowly rotating el-

llyptical galaxies, i.e. systems which are mostly random motion pressure supported, while mergers with mass ratios of $\sim (3 - 4.5) : 1$ will, likely, result in disky, rapidly rotating elliptical galaxies (e.g. Naab and Burkert, 2003; Bournaud *et al.*, 2005). These are not disk galaxies, but rather elliptical galaxies with a disky isophotal shape, i.e. systems which are, to some considerable extent, still rotationally supported. Galaxy mergers with mass ratios of $\sim (4.5 - 10) : 1$ will not produce elliptical galaxies at all, but they will create early-type, progressively more disk-dominated systems, such as S0 galaxies. These have been referred to by some authors as intermediate mergers (e.g. Bournaud *et al.*, 2005, 2007). Finally, galaxy mergers with mass ratios $\geq 10 : 1$ are known as minor mergers. These are phenomena of smaller impact on the morphology of the larger galaxy, often producing remnants that can be generally described as disturbed spiral galaxies (e.g. Velazquez and White, 1999).

1.2.3 Active Galactic Nuclei

Another key aspect in the process of galaxy evolution is the activation of the central engine, a phenomenon known as an active galactic nucleus (AGN). Observationally, an AGN can be recognized by the presence of a star-like compact point source, which is superimposed on the central region of the host galaxy and emits higher-than-normal luminosity that can not be directly attributed to light from stars.

Generally, the AGN family can be divided into Seyferts and Quasars/QSOs⁵. The main difference between them is that a typical Seyfert AGN releases as much energy in the visual bands as all the stars of its ($\sim 10^{11} L_{\odot}$) host galaxy, while a typical QSO is by a factor of ~ 100 times brighter than the stars of its host galaxy. Seyferts and QSOs, however, are not the only sub-classes of the AGN family. Below, I briefly summarize the most important characteristics of the basic AGN sub-classes:

- i **Seyfert type-1/Seyfert type-2:** Likely, they are intrinsically the same type of source. Seyfert type-1s show broad line emission in their spectra, while Seyfert type-2s do not (except in polarized light). Presently, it is generally accepted that this distinction is a function of our line-of-sight angle. If we can see directly towards the nucleus, then we can see the broad line region (BLR) and, therefore, we observe a Seyfert type-1 galaxy, otherwise, we observe a Seyfert type-2.
- ii **QSOs:** They have similar spectra with Seyfert galaxies but with weaker stellar absorption features and weaker narrow lines relative to their broad lines. About 5–10% of QSOs are strong radio emitters. The number of QSOs per unit volume reaches a maximum at a redshift of ~ 2 .

⁵Quasar is a sort phrase for quasi-stellar radio source, while QSO is sort for quasi-stellar object. Although initially the two terms were used in order to distinguish between radio-loud and radio-quiet objects, currently the term QSO is used to describe both classes.

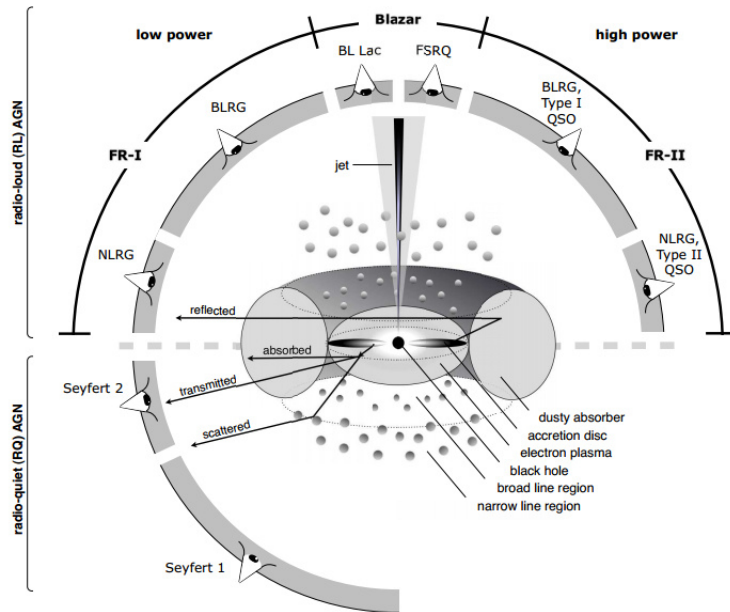


Figure 1.6: Adopted from *Beckmann and Shrader (2012)*. Graphical illustration of our current understanding of the AGN phenomenon. Under this unified scheme, the AGN type we observe is a strong function of the angle of our line-of-sight and the object's power output.

- iii **Radio galaxies:** They are divided in broad line radio galaxies (BLRG – equivalent to a Seyfert type-1) and narrow line radio galaxies (NLRG – equivalent to a Seyfert type-2). In basic terms, these are the radio-loud analogs of Seyferts type-1s and type-2s.
- iv **Low Ionization Nuclear Emission Line Region (LINERs):** LINERs are very common across almost all Hubble types and especially in spirals. Their spectra are similar to Seyfert galaxies except that their low-ionization lines are relatively strong, while ~ 25% of LINERs exhibit broad line emission. All LINERs, however, are not necessarily AGNs, since LINER-type spectra can also be produced by ionization from stars or shocks.
- v **Blazars:** They are radio-loud AGNs that show high variability on short time-scales. It is believed that this is an effect of a relativistically beamed component close to our line-of-sight.

The plethora of common characteristics between the different types of AGNs imply that, at least, a partial unification under one scheme is possible. The current unification scheme for AGNs is shown in figure 1.6.

Under the unified model, the AGN phenomenon originates from the accretion of matter on an SMBH through a hot accretion disk, while the different types of AGNs that we observe originate from a combination of different viewing angles and accretion rates. Moreover, accretion of matter on an SMBH produces strong radiation across the entire electromagnetic spectrum. The infrared (IR) and ultraviolet (UV)/optical continuum emission components are believed to be mainly of thermal origin, arising from the dusty torus and from different radii of the hot accretion disk, respectively. X-ray emission is thought to originate from the inverse-Compton scattering of the UV/optical continuum photons by relativistic electrons in the hot corona that surrounds the accretion disk, in a process that is commonly referred to as “Comptonization” of the input UV/optical spectrum. Finally, the radio emission is, most likely, not of thermal origin but rather Synchrotron radiation, i.e. it is produced by relativistic particles (e.g. electrons) that are accelerated in a magnetic field.

In order for these phenomena to take place, however, matter has to reach the accretion disk and fall into the SMBH, which means that gas orbiting at larger radii of a galaxy has somehow to lose most of its angular momentum⁶. Understanding, therefore, the circumnuclear activity in active galaxies is essential in order to shed some light on the AGN fueling question.

On larger scales ($\geq \sim 3$ kpc) the picture is relatively clear. Large-scale dynamical perturbations like close encounters and major/intermediate mergers are the proposed mechanisms for removing angular momentum from the gas to drive it towards the central region (see section 1.2.2). This appears to be consistent with studies on AGN demographics. At a redshift of ~ 2 , nearly 28% of AGNs reside in spheroids, while $\sim 17\%$ of AGN hosts show clear large-scale interaction signs (Kocevski *et al.*, 2012), implying that large-scale interactions should play an important, although not necessarily dominant, role⁷.

Moreover, in the sample of Kocevski *et al.* (2012), nearly 50% of AGNs reside in disk galaxies, while $\sim 56\%$ of AGN hosts seem to be relatively undisturbed and relaxed, implying that stochastic accretion phenomena are, likely, responsible for fueling the majority of AGNs at $z \sim 2$. This makes the small-scale (sub-kpc) processes extremely important for galaxy evolution. Secular evolution mechanisms ranging from nested bars (e.g. Shlosman *et al.*, 1989) and spirals (e.g. Martini and Pogge, 1999) to warped nuclear disks (Schinnerer *et al.*, 2000a,b), and lopsidedness ($m = 1$) (Kormendy and Bender, 1999; García-Burillo *et al.*, 2000), along with environment related interactions of lower impact, such as minor mergers and intergalactic cold gas accretion, have been proposed over the years as fueling mechanisms for AGNs. Despite the tremendous efforts, however, our understanding

⁶The angular momentum of a particle orbiting the galaxy near our solar system has to be reduced to $\sim 10^{-5}$ of its initial value in order to reach the Galactic Center (GC) (Peterson, 1997).

⁷We have to keep in mind, however, that factors like dust obscured AGNs, limited imaging depth etc. may bias these observational statistical results.

of the underlying physical processes that contribute to the nuclear activity is still far from being complete and conclusive and the discussion remains open.

Finally, the presence of an AGN has also an impact on its host galaxy, via a process known as AGN feedback. Lately, there is significant amount of observations suggesting that, while the fueling of the central engine is mainly controlled by its host galaxy's evolution, its energy output appears to play an important role in (at least, partially) controlling the evolution of its host galaxy as well. Broadly speaking, AGN feedback usually refers to either of the following phenomena: Mechanical feedback in the form of energetic particle outflows, winds, and/or relativistic jets, or radiative feedback in the form of the– radio to X-rays– radiation field that an accreting SMBH produces. Through these mechanisms, the SMBH is thought to self-limit its growth and affect its host galaxy's evolution, since it can, potentially, eject enough amounts of energy into the interstellar medium (ISM) to terminate the gas inflow and quench the nuclear star formation (e.g. [Kormendy and Ho, 2013](#)). In this sense, AGN feedback is usually considered to be a process with a negative impact on the AGN's host galaxy. It can, however, have a positive impact as well, since there are evidence to suggest that mechanical energy from a jet can disturb gas located at larger radii of a galaxy and trigger star formation instead of quenching it (e.g. [Fassett and Graham, 2000](#); [Rejkuba et al., 2001](#); [Salomé et al., 2015](#)). The exact nature of these mechanisms, though, still remains poorly understood.

1.3 Observations

1.3.1 Observing in the NIR

A promising way to study all these very important phenomena is by studying the IR radiation of astronomical objects. Since its discovery by Sir William Herschel in 1800, IR radiation has been increasingly used to explore the Cosmos. It is divided into three main wavelength regimes, namely, the near-IR (NIR) ($0.75\text{-}5\ \mu\text{m}$), the mid-IR (MIR) ($5\text{-}25\ \mu\text{m}$), and the far-IR (FIR) ($25\text{-}350\ \mu\text{m}$)⁸. Our planet's atmosphere, however, is not transparent to all incoming IR wavelengths, so ground-based observations are only possible in specific narrow wavelength windows up to $\sim 26\ \mu\text{m}$, while after that the atmosphere becomes effectively opaque (see top image of figure 1.7).

Although atmospheric opacity is an essential feature for the creation and sustainability of life on Earth, since it blocks most of the (harmful for life) high energy cosmic radiation (i.e. UV, X-rays, and γ -rays), it tends to make ground-based astronomical observations difficult. The principal limitation is that the Earth's atmosphere contains water vapor, carbon dioxide, and oxygen molecules, which absorb a significant amount of the incoming IR radiation. In order to minimize the atmospheric absorption effects, most of the IR telescopes are built in very dry places and at high altitudes. Such locations on Earth include

⁸Wavelengths longer than $\sim 350\ \mu\text{m}$ are considered to be in the sub-millimeter and radio regions of the spectrum.

the Mauna Kea Observatory in Hawaii⁹ (at ~ 4.2 km above sea level) and the Paranal Observatory (at ~ 2.6 km) in Chile, but even at these altitudes the transparency of the atmosphere is, generally, limited to only the few transparent atmospheric windows mentioned earlier. The shorter IR wavelength atmospheric windows are in the NIR regime and are covered by the *J* ($1.25 \mu\text{m}$), *H* ($1.65 \mu\text{m}$), *K* ($2.20 \mu\text{m}$), *L* ($3.50 \mu\text{m}$), and *M* ($4.80 \mu\text{m}$) filters, while the atmospheric windows in the longer IR wavelengths are in the MIR regime and are covered by the *N* ($10 \mu\text{m}$) and *Q* ($20 \mu\text{m}$) filters (see bottom figure 1.7).

But why is NIR radiation an important astronomical tool? At first, it enables us to see through the cosmic dust. Dust blocks the light in the visible part of the electromagnetic spectrum, but for the NIR light the dust is almost transparent¹⁰, a property which is crucial when attempting to observe objects either in dusty environments (e.g. star forming regions, stars with circumstellar envelopes etc.), or obscured by interstellar dust (e.g. the GC, galaxies with dust lanes etc.). Perhaps one of the most important moments of NIR astronomy was the confirmation of the presence of an SMBH at the center of our own Milky Way galaxy, by detecting the NIR counterpart of the SgrA* radio source (see figure 1.8, e.g. [Genzel et al., 1997](#)). Furthermore, observing galaxies in the NIR allows to better probe their old (i.e. cooler) stellar components, which can provide vital information about their evolution, since the distribution of their old stars has been found to be related with the merging histories of galaxies (see section 1.2.2, e.g. [Hopkins et al., 2009b](#)). Secondly, dust gets heated-up and emits in the NIR. Its sublimation temperature is ~ 1500 K, below which (i.e. longward of $\sim 1.9 \mu\text{m}$) the dust absorbs UV/optical light and re-emits a part of it in the NIR. Studying, therefore, nearby galaxies in the NIR can reveal important information about the physical conditions in their central regions (see section 2.4). Finally, NIR observations make the study of objects at extreme cosmological distances, i.e. galaxies in the very early Universe, possible, since their (rest-frame) UV/optical emission is so redshifted—due to the expansion of the Universe—that they can only be detected in the IR (see figure 1.9). Studies of these objects can potentially unlock the mysteries of how the first galaxies were born (see section 1.2.1) and how the primordial SMBHs at their centers have formed and grown to the sizes that we observe today, all of which are related to very important and still open scientific questions.

Over the years, a number of sensitive, whole-sky, low-resolution NIR surveys like the Two Micron All-Sky Survey (2MASS) have been conducted, enriching our knowledge around both point (e.g. brown dwarfs) and extended (e.g. galaxies) sources. In addition, space-based attempts, like the IRAS, ISO, Spitzer, and WISE, have opened a window towards the MIR and FIR parts of the spectrum, extending our perception into previously unexplored wavelength regimes. Finally, recent advancements in the sophistication and efficiency of NIR detectors and in observation assistance modules—i.e. active and adaptive

⁹This is the observatory where the data discussed in this work were taken from, using the Subaru telescope and the High-Contrast Coronagraphic Imager for Adaptive Optics (HiCIAO) instrument.

¹⁰A representative example is that towards the GC the extinction caused by interstellar dust in the *V* band is ~ 30 mag, whereas in the *K_S* band it is only ~ 2.5 mag.

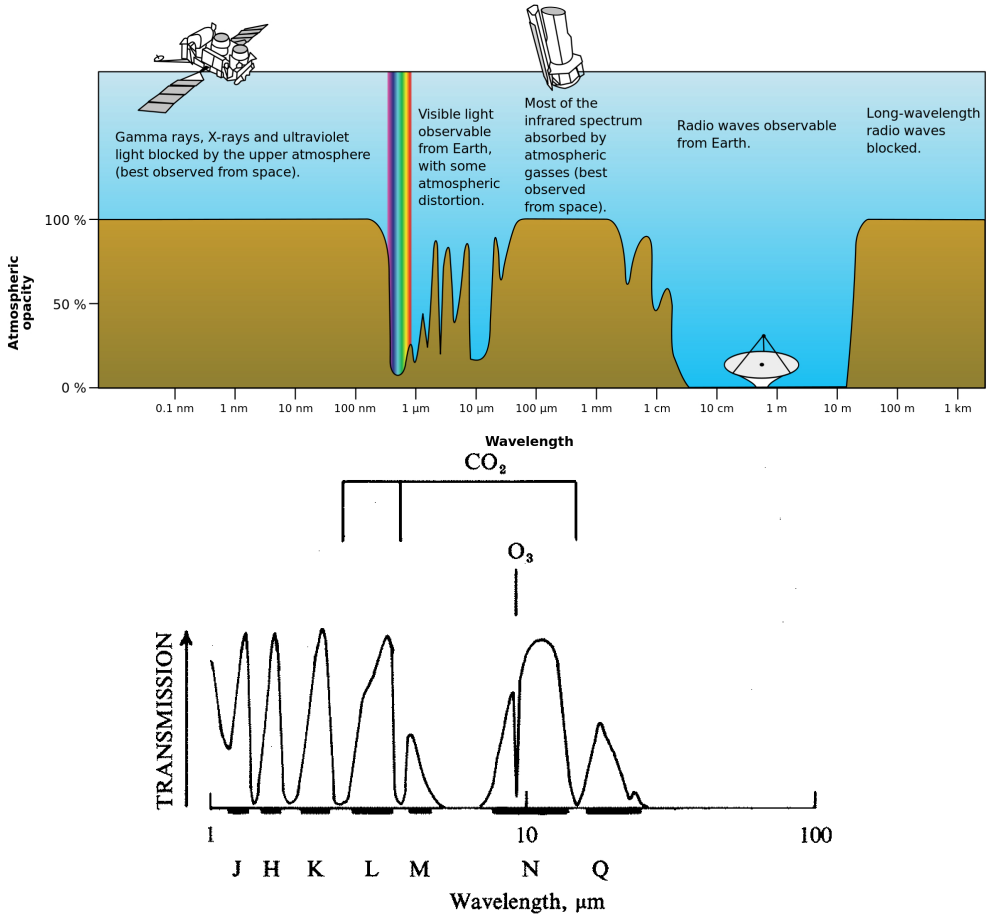


Figure 1.7: Top: Atmospheric opacity across the entire electromagnetic spectrum, indicating the wavelength regimes at which ground-based observations are possible. Image credit: NASA. Bottom: Atmospheric transparency windows in the NIR and MIR. The wavelength windows at which the atmosphere is largely transparent are marked with the corresponding filters names. Image credit: Allen (1975).

optics (AO) systems aboard the top-of-the-range 8-meter class telescopes– have enabled us to reach unprecedentedly high angular resolutions with ground-based observations, providing a very useful (and cheaper compared to space-based missions) tool for unlocking the mysteries of our Universe.

1.3.2 Ground-based AO assisted observations

A telescope's power to resolve neighboring point sources depends only on its primary mirror diameter and the wavelength of the incoming radiation. The angular resolution of a

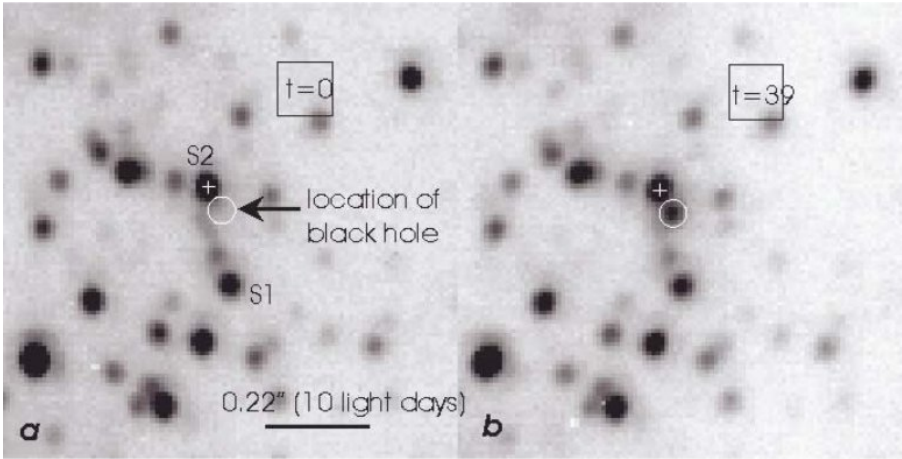


Figure 1.8: NACO/Very Large Telescope (VLT) H band images showing SgrA* in its quiescent (left) and variable states (right). The white circle indicates the position of SgrA*. Image credit: [Genzel et al. \(2003\)](#)

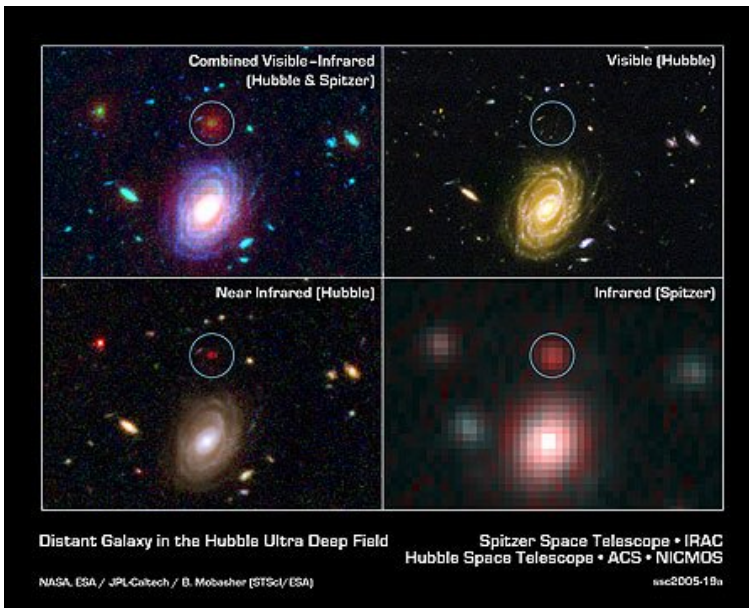


Figure 1.9: Comparison of an optical and a NIR HST image, a perfect example of the NIR imaging potential for studying primordial galaxies. Image credit: NASA/ESA/STScI

telescope can be calculated via the Rayleigh criterion:

$$\theta = 1.22 \times \left(\frac{\lambda}{D} \right), \quad (1.1)$$

where θ (in radians) is the minimum angular separation that two point sources must have in order to be distinguished from each other, λ (in meters) is the wavelength of the incoming radiation, and D (in meters) is the diameter of the primary mirror of the telescope. For example, the Subaru telescope with its 8.2 m primary mirror diameter has diffraction-limited angular resolutions of 0.037 arcsec, 0.049 arcsec, and 0.067 arcsec in the J , H , and K_S bands, respectively. In the ideal case where there is no atmosphere between the target and the observer¹¹, a point source observed through a diffraction-limited telescope would have the size of the Airy disk, which is the dominant component in the point spread function (PSF).

For ground-based observations, however, the atmosphere is present and opacity (see section 1.3.1) is not the only obstacle it introduces. Different temperatures and wind speeds between different layers of the atmosphere cause deformations¹² on the wavefront of the incoming radiation. When we observe a point source for a time period of the order of a few seconds or longer, these distortions average out and the resulting PSF is mostly dominated by the atmospheric turbulence. The full width at half maximum (FWHM) of the PSF is known as the astronomical seeing. The seeing describes the atmospheric conditions of a given night, at a given location and, therefore, it serves as a measure of the degree that the atmospheric distortions affect an astronomical image. In other words, seeing is a direct measurement of the quality of a ground-based observation.

So, can we somehow work around this limitation? This is the role of the AO systems. An AO system tries to trace and correct the atmospheric distortions, using a wavefront sensor to identify the degree of deformation of the input wavefront¹³, a computer to calculate the appropriate corrections¹⁴, and a deformable mirror¹⁵ in the optical path to apply these corrections in order to “straighten” the output wavefront. This process is almost continuous throughout an AO assisted observational session, since it is repeated in timescales of the order of a few tenths of milliseconds. A graphical illustration of the way that a typical AO system works is shown in figure 1.10. The results of this technique are quite impressive. Although in theory the system can deliver diffraction-limited images, in practice the resulting PSF is a combination of the diffraction pattern of the telescope with residual uncorrected atmospheric terms. In the case of the Mauna Kea Observatory in Hawaii, the average seeing is $\sim 0.65 - 0.75$ arcsec, while the average FWHM measured at the Subaru IR Nasmyth platform¹⁶ is of the order of ~ 0.18 arcsec, an improvement in the achieved angular resolution by a factor of ~ 4 . In figure 1.11, I present a clear example of the quality improvement of an AO assisted image.

¹¹I.e. space-based observatories like the HST.

¹²This is relatively similar to trying to observe an object from the bottom of a water pool on a windy day. Surface waves will cause continuous motion of the object’s image on the eye, resulting in a blurry image.

¹³It measures the phase differences across the input wavefront.

¹⁴It uses the phase differences to estimate the curvature across the input wavefront.

¹⁵It is deformed, approximately, to the opposite of the input wavefront’s shape.

¹⁶The focal point where the HiCIAO instrument is mounted on the Subaru telescope.

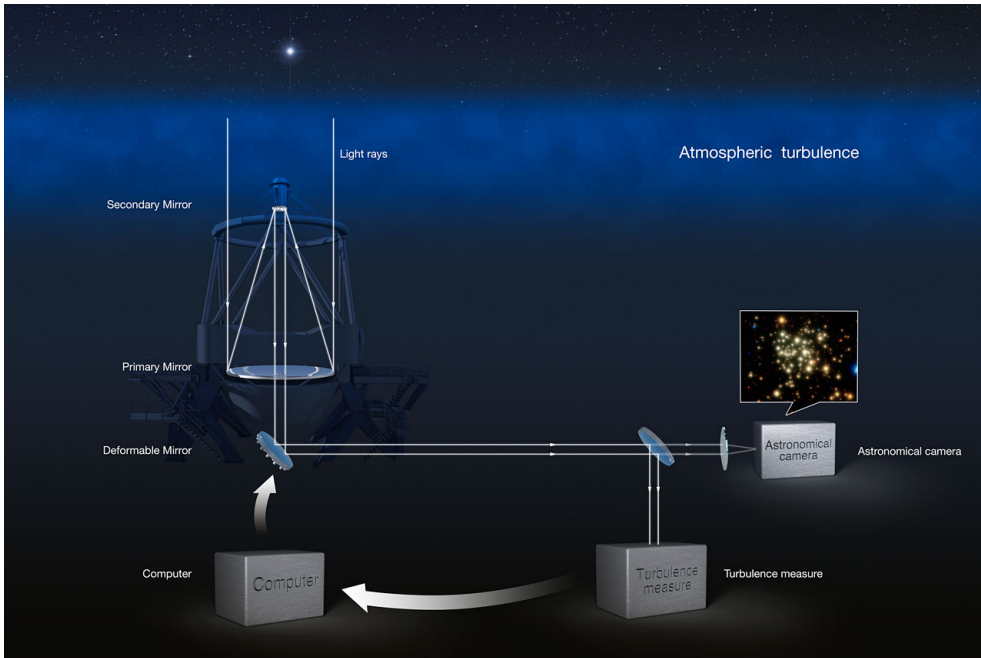


Figure 1.10: A graphical illustration of an AO system. Image credit: ESO



Figure 1.11: Left: The GC without the use of the AO system. Right: The GC and the location of the SMBH (labeled SgrA*) with the use of the AO. Image credit: Keck Observatory/UCLA GC Group.

1.4 Dissertation outline

The studies presented in this dissertation were conducted using mainly NIR, AO assisted data taken with the Subaru telescope at the Mauna Kea observatory in Hawaii. I have performed two case studies using NIR imaging data of NGC3718 (chapter 2) and NGC5128

(chapter 3). Both of these projects deal with the impact that processes related to the central SMBHs can have either on the immediate surroundings (on small-scales – NGC3718), or on the outer parts (on large-scales – NGC5128) of their host galaxies. Chapters 2 and 3 are written in an autonomous way, i.e. both contain introduction, observations and data reduction, data analysis and results, and discussion sections in an effort to be as easily readable as possible. In this introduction, I tried to equip the reader, at least, with qualitative descriptions of the basic tools and definitions that one may need in reading and understanding this dissertation. For reading-friendly reasons, important definitions, descriptions, and theoretical aspects are repeated throughout the text whenever it is deemed necessary. Below, I introduce the reader to key aspects of each chapter.

1.4.1 Preamble of chapter 2

In chapter 2, I analyze high angular resolution Subaru NIR imaging and Multi-Element Radio Linked Interferometer Network (e-Merlin) radio data of NGC3718, in order to obtain a detailed view of the physical processes that take place in its center. The Subaru NIR maps suggest, on one hand, that the dust lane does not cause any large-scale absorption phenomena towards the center of the stellar bulge and, on the other, that there is a significant contribution from hot dust to the NIR emission from the nucleus. The peak of the NIR emission is offset by ~ 4.25 pc from the center of the underlying stellar bulge and potentially coincident with the (also) offset peak of the e-Merlin 6 cm radio emission. Moreover, the shape of the radio emission suggests that there is one (or potentially two, forming an X-shape) candidate bipolar jet(s) extending ~ 1 (~ 0.6) arcsec, which combined with the good agreement between the velocity dispersions of the stars and the gas and the presence of X-ray emission, could point towards feedback processes from the AGN. Additionally, I present evidence that NGC3718 is a core galaxy, despite the fact that it is a gas-rich (on large-scales) object, while its mixed photometric and kinematic characteristics imply that it is a merger remnant. All the above combined with the, independently observed, relative shift between the broad and the narrow $H\alpha$ lines of NGC3718 strongly indicate the presence of an SMBH recoil. Finally, I discuss a potential interpretation that can naturally incorporate all these findings into a physically consistent picture.

1.4.2 Preamble of chapter 3

In chapter 3, I analyze high angular resolution Subaru NIR and archived HST $F555W$ and $F814W$ imaging data of a region close to the northern middle lobe (NML) of the jet of Centaurus A (Cen A), at a distance of ~ 15 kpc from the center of NGC5128 and towards the north-east (NE). The low-pass filtered NIR images show strong ($> 3\sigma$ above the background) signal at the equivalent position of the brightest star in the HST field. Through a detailed statistical analysis of the background noise of the NIR images, I estimate the probability of observing $> 3\sigma$ signal in three independent measurements and at the same position due to random background fluctuations alone to be $\leq 10^{-7}\%$. Since this is negligible, the observed NIR signal, likely, originates from the NIR counterparts of the brightest

HST star. In a subsequent photometric analysis of the NIR $> 3\sigma$ signal/brightest HST star, I calculate its $V - I$, visual-NIR, and NIR color indices, which are consistent with a yellow supergiant (YSG) with an age of $\sim 10_{-3}^{+4}$ Myr. Moreover, the next two brighter stars in the HST field are, probably, also supergiants with ages of $\sim 16_{-3}^{+6}$ Myr and $\sim 25_{-9}^{+15}$ Myr, respectively. The ages of these supergiants are in very good agreement with the ages of the young blue stars that populate the region and are believed to be the result of a jet-induced star formation that occurred $\sim 10 - 15$ Myr ago.

1.4.3 Preamble of chapter 4

In the final chapter, I discuss a general framework that can engulf both of these case studies, I compare the findings of the present work with other known cases of SMBH recoils and jet-induced star forming regions, I discuss the potential that NIR, ground-based, AO assisted observations can have in our effort to understand the Cosmos, and I briefly summarize the key results of this dissertation.

NGC3718: Diaries of a recoiled SMBH?

2.1 Introduction to chapter 2

An ideal object for trying to further study some of the important questions I briefly presented in chapter 1 is NGC3718 (see figure 2.1). NGC3718 and its companion galaxy, NGC3729, belong to the loose Ursa Major group, while NGC3718 is one of the largest members of the group. It is not clear at present if these galaxies interact gravitationally or not and to what extent (Tully *et al.*, 1996). Karachentsev *et al.* (2013) report that both galaxies are members of the NGC3992 subgroup– named after the gravitationally dominant member–, one of the most massive subgroups in Ursa Major. Moreover, they note that the velocities within this subgroup do not show significant correlation with the distances, implying a non-virialized system. Initially, de Vaucouleurs *et al.* (1991) classified NGC3718 as an SB(s)a pec, mainly because of its prominent dust lane, which was considered to be indicative of the presence of a bar that ended in a spiral-arm like feature. Holmberg (1958) classified NGC3718 as an S0p, while numerous authors (e.g. Whitmore *et al.*, 1990; Reshetnikov and Combes, 1994) have classified this galaxy as a polar ring galaxy, perplexing our understanding around its true morphology.

The most characteristic features of NGC3718 are its warped atomic and molecular gas disk and its prominent dust lane, which covers a big portion of its stellar bulge. The gas dynamics of NGC3718 has been extensively studied by several authors. Schwarz (1985) studied the HI dynamics and discovered that the atomic gas distribution formed a complex 3-D warped structure, which they modeled by fitting tilted and concentric rings, orbiting from nearly edge-on closer to the center to nearly face-on at larger distances. Pott *et al.* (2004)



Figure 2.1: An 9.5×4.5 arcmin of NGC3718 from the SDSS survey (*gri* composite image).

and [Krips *et al.* \(2005\)](#) studied the distribution of the molecular gas, tracing it through the $CO(1 \rightarrow 0)$, $CO(2 \rightarrow 1)$ and $HCN(1 \rightarrow 0)$ transitions. They also fitted a tilted rings model on NGC3718 and found that the motion of the molecular gas follows the motion of the atomic gas, but they also saw signatures of the warp down to smaller scales (~ 250 pc). The HI distribution was re-mapped by [Sparke *et al.* \(2009\)](#) using higher-resolution Very Large Array (VLA) data and confirmed the tilted ring models of the previous studies, although with slightly different parameters. They show that the outer part of the warped disk extends out to $\sim 35 - 42$ kpc and they estimate its age to be $\sim 2 - 3$ Gyr, while the inner part of the disk is nearly polar and still under formation. Finally, they promote a classification for NGC3718 as a polar ring galaxy, since they do not find HI gas orbiting in the plane of rotation of the stellar disk, and they attempt to explain the warp invoking differential precession.

Similar features are seen also in NGC5128, the host galaxy of the powerful radio source Cen A. A dust lane (Dufour *et al.*, 1979) and a warped gas disk (e.g. Wild *et al.*, 1997; Sparke, 1996), along with the presence of (stronger than in NGC3718) radio emission originating from the nucleus are among the common properties between the two galaxies that often lead to characterizing NGC3718 as the “northern Cen A”.

NGC3718 is also a part of the NUClei of GALaxies (NUGA) survey, which is dedicated to studying several nearby low-luminosity active galactic nuclei (LLAGN) (García-Burillo *et al.*, 2003). Its spectroscopic features led Ho *et al.* (1997b) to classify NGC3718 as a LINER L1.9 galaxy. The detection of weak broad $H\alpha$ emission ($FWHM_{H\alpha, Broad} \approx 2350 \text{ km s}^{-1}$) from the nucleus and of strong $[OI]\lambda\lambda 6300\text{\AA}$ ($FWHM_{[OI]} \approx 570 \text{ km s}^{-1}$) were considered indicative of a hidden AGN (Filippenko and Sargent, 1985). Further indications for an active nucleus came from 18 cm Merlin radio data analyzed by Krips *et al.* (2007), which revealed a candidate jet structure stretching ~ 0.5 arcsec north-west (NW) from the nucleus, while NGC3718’s bolometric luminosity (i.e. $\sim 10^{41} - 10^{42} \text{ ergs s}^{-1}$ – estimated from its X-ray emission) implies accretion below the Eddington limit.

Chitre and Jog (2002) consider NGC3718 (object ARP214) to be an advanced merger remnant, while Jog and Chitre (2002) discuss its mixed photometric and kinematic characteristics. Photometrically, NGC3718 shows characteristics of a spiral galaxy– i.e. it has an exponential surface brightness profile–, kinematically, however, it is similar to an elliptical galaxy– i.e. it is mostly supported by pressure from random motions of stars–, as the $V_C\sigma^{-1} \sim 0.5 - 1$ in the inner few kpc suggest. Bournaud *et al.* (2005) studied galaxy mergers with different mass ratios using N-body simulations and they found that objects with mixed photometric and kinematic characteristics can result from mergers with intermediate mass ratios (i.e. $> (3 - 4.5) : 1$, see section 1.2.2).

Chapter 2 is organized as follows. In Section 2.2 I describe the data and data reduction; in section 2.3 I describe the alignment and pre-processing of the three NIR bands; in section 2.4 I present the NIR maps, the NIR light decomposition, and the 6 cm e-Merlin radio map; in section 2.5 I discuss the scaling relations, the potential classification, and the observed characteristics of NGC3718; in section 2.6 I present additional evidence regarding the possibility that an SMBH recoil is present– or not– in NGC3718; and in section 2.7 I attempt to put all the pieces together to derive a physically consistent global picture.

Throughout this chapter the following are adopted. In all images north is up and east is left. The adopted cosmology includes $\Omega_M = 0.27$, $\Omega_\Lambda = 0.73$, and $H_0 = 67.8 \text{ km s}^{-1}$, and a redshift $z = 0.003927$, corrected to the reference frame of the 3K CMB¹⁷. The suggested distance modulus for NGC3718 is $\mu = 31.2$, reflecting a distance $D = 17.4 \text{ Mpc}$, which leads

¹⁷http://ned.ipac.caltech.edu/cgi-bin/objsearch?search_type=obj_id&objid=26880&objname=1&img_stamp=YES&hconst=67.8&omegam=0.27&omegav=0.73&corr_z=1

to a scale of $84 \text{ pc arcsec}^{-1}$. Finally, for all the conversions from light to mass, I use the mass-to-light ratio from [Bell *et al.* \(2003\)](#). The general form of the ML^{-1} ratio is

$$\log\left(\frac{M_*/M_\odot}{L/L_{\odot,\lambda}}\right) = a_\lambda + b_\lambda(B - V), \quad (2.1)$$

with a_λ and b_λ being $a_J = -0.261, a_H = -0.209, a_K = -0.206, b_J = 0.433, b_H = 0.210$, and $b_K = 0.135$ in the NIR. For NGC3718 this reflects a K_S -band $ML^{-1} \sim 0.78$, using $M_V^{NGC3718} = -20.73$ mag and $M_B^{NGC3718} = -20.01$ mag, magnitudes corrected for extinction and K-corrections retrieved from the NASA/IPAC Extragalactic Database (NED) (footnote 17).

2.2 Observations and data used in chapter 2

2.2.1 Subaru data of NGC3718

The available data set for the analysis of NGC3718 consists of NIR– J (5), H (11), and K_S (12) bands (number of images)– AO assisted data taken with the HiCIAO ([Suzuki *et al.*, 2010](#)) instrument in Direct Imaging Mode (DIM), on the 17th of May 2012, aboard the Subaru telescope at Mauna Kea, Hawaii. The detector used is a Hawaii-IIRG Mercury Cadmium Telluride (HgCdTe) with 2048×2048 pixels², providing a field of view (FoV) of 20×20 arcsec², which results in a pixel scale of $0.010 \text{ arcsec pixel}^{-1}$. The exposure time for the individual frames in all bands is $t_{exp}^{JKS} = 60$ sec, with the total observing time being $\sim 1 \text{ h } 40 \text{ m}$. The total variation in airmass during the observations is ~ 0.082 . The AO system used is the AO188 ([Hayano *et al.*, 2010](#)). The system is installed at the IR Nasmyth platform of the Subaru telescope and it is equipped with a 188-element wavefront curvature sensor with photon counting avalanche photodiode (APD) modules and a 188-element bimorph mirror. For this data set the AO system operates in self-reference mode on the core of NGC3718. The resulting angular resolution of the NIR images is ~ 170 mas.

A reduction pipeline was developed specifically for this data set in order to correct for the 32-strip artifact noise introduced by the 32 readout channels of the detector, since no reduction package was available for HiCIAO. Besides this extra step, all the, initially dithered, raw images were corrected for bad pixels, flat-fielded (dome-flat), aligned (using isophote fitting), and, finally, median stacked (see appendix A). The final images allowed then for the generation of sky frames for all the NIR bands from the data themselves, by clipping each image near its modal background value and adding a high-frequency layer on top¹⁸ (see figure 2.2). The data with the sky subtracted are shown in figure 2.3.

¹⁸This process could be also described as a background subtraction, in the NIR, however, most of the background contamination refers to the sky component. Each sky frame was obtained by keeping values lower than the mode of the corresponding image, which should be a good approximation of the sky contamination. Subsequently, a layer obtained by high pass filtering each image was added on the corresponding sky frame, in order to include the pixel-to-pixel variations as well.

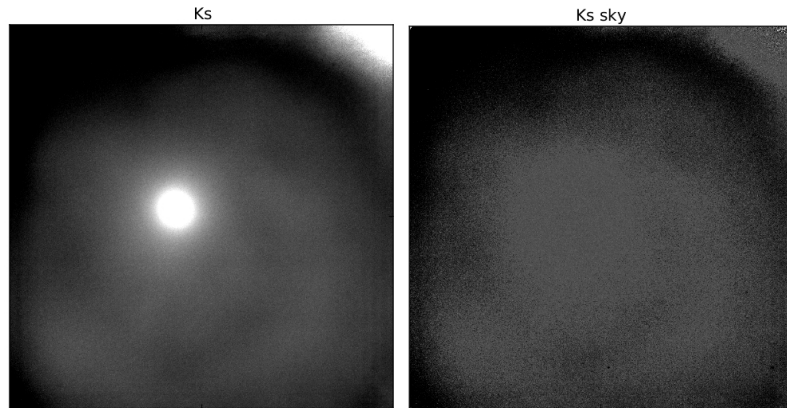


Figure 2.2: $20 \times 20 \text{ arcsec}^2$ reduced K_S band image with the sky component (left) and the sky frame that was generated from the K_S band image (right). Similar sky frames were generated and subtracted from the J and H band images.

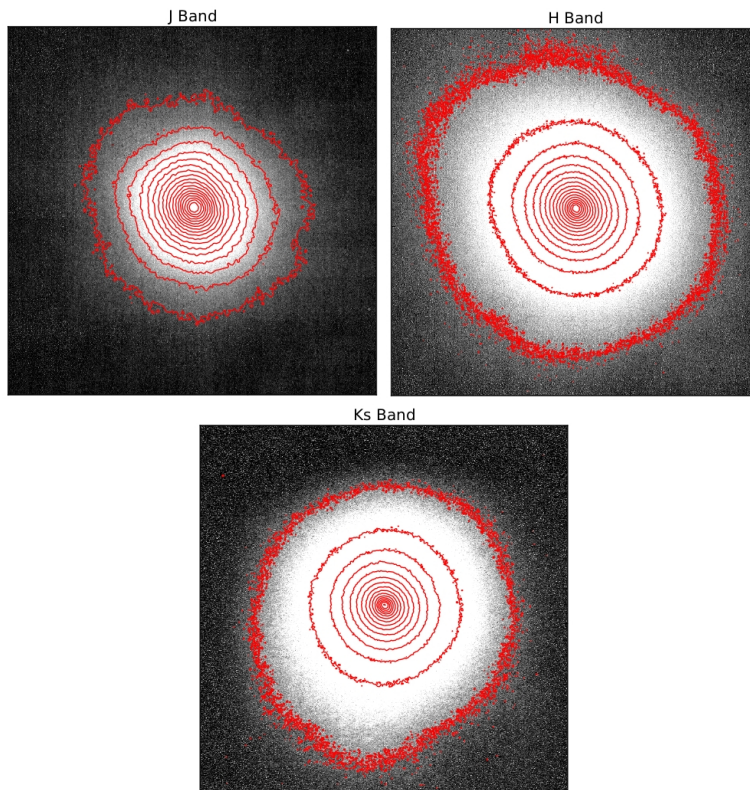


Figure 2.3: Sky subtracted J (top left), H (top right), and K_S (bottom middle) band images.

2.2.2 e-Merlin data of NGC3718

The e-Merlin synthesis telescope (Garrington *et al.*, 2004) is a radio interferometer consisting of seven radio antennas—baselines of up to 217 km—, which are connected to the Jodrell Bank Observatory (Manchester, UK) by a new optical fiber network. An inhomogeneous array, e-Merlin is comprised of the 25 m antennas, Mark II, Knockin, Defford, Pickmere, and Darnhall, the 32 m dish at Cambridge, and the 76 m Lovell telescope.

The data presented in this chapter were obtained during the commissioning phase of e-Merlin using only the five 25 m dishes, resulting in a primary beam of 10 arcmin. The maximum and minimum baselines available were 133.7 km— between Pickmere and Defford— and 11.2 km— between Pickmere and Mark II—, respectively. The complete array will have a bandwidth of 2 GHz, which will provide more than ten times the continuum sensitivity of the original Merlin. For the observations of NGC3718, the e-Merlin array operated at 5 GHz for 10 hrs on the 3rd of August 2011, with four 128 MHz sub-bands of 512 spectral channels each, yielding a total bandwidth of 512 MHz. The observations did not include the longest baselines (i.e. to Cambridge), resulting in a final angular resolution of ~ 100 mas.

The reduction and analysis of the data was performed using the National Radio Astronomy Observatory's AIPS. Initially, the data were edited using SPFLG and IBLED, then averaged to sixty-four channels per intermediate frequency (IF) channel and, subsequently, concatenated using DBCON before further editing. Delay and rate corrections for the calibrator sources were derived using FRING, while the time-dependent phase, amplitude and phase solutions using CALIB. Flux calibration was performed by using short observations of 3C286 at the beginning and end of each observing run, and the flux density scale was calculated with SETJY (Perley and Butler, 2013). To account for the resolution of the e-Merlin shortest spacing (see the Merlin User Guide), the flux density for each IF was reduced by 4%, while band-pass and phase calibrations were performed using bright point sources. Absolute calibration is expected to have an accuracy of $\sim 10\%$ for the commissioning data.

The minimum quoted positional uncertainties are of the order of ~ 1 mas. These are associated with phase transfer errors from the phase reference to the target source for a typical 3 degrees separation. This, however, assumes six stations— including Cambridge— and online L-Band link corrections. For this observing run, the phase reference source used is J1146+5356 with the observations being referenced to the coordinates given in the Very Long Baseline Array (VLBA) calibrator list, namely, $\alpha_{2000} = 11 : 46 : 44.204328$ and $\delta_{2000} = +53 : 56 : 43.08356$. These coordinates indicate a separation of ~ 2.28 degrees between J1146+5356 and NGC3718. Accounting also for the lower resolution of these data— due to the absence of the longest baseline— and allowing for known—yet small— phase corrections for the L-Band link transmission delays around this observational epoch, the phase transfer errors are expected to be ~ 4 mas. The quoted positional uncertainties of

J1146+5356 in the VLBA Calibrator list are 0.35 mas in right ascension (RA) and 1.17 mas in declination (Dec). The formal measurement uncertainty from the peak of the e-Merlin map is $100/2Q$ mas, with a restoring beam of ~ 100 mas and a peak signal-to-noise ratio (SNR) in the image of Q , which in this case is better than ~ 60 . Therefore, the total positional uncertainties are estimated to be ~ 4.1 mas.

2.3 Data processing

2.3.1 Locating the center of the stellar bulge

The first step in the analysis of the NGC3718 NIR data is to align the J , H , and K_S images. Due to the absence of secondary sources in the FoV, I choose an alignment method based on fitting ellipses on the isophote contours of NGC3718. For this, the Image Reduction and Analysis Facility's (IRAF)¹⁹ ellipse task was used, which fits ellipses on the iso-intensity contours of the light distribution of a galaxy. In figure 2.4, I plot the X_{center} and Y_{center} coordinates, as indicated by each fitted ellipse versus its semi-major axis (SMA).

With the exception of the J band X_{center} coordinate and the K_S band Y_{center} coordinate, the rest of the curves are close to what would be normally expected²⁰. The behavior of the J band is, likely, the result of its lower flux (i.e. F_J) compared to the fluxes of the H and K_S bands ($F_{K_S} \sim 3F_J$ and $F_H \sim 2.5F_J$, respectively). This is primarily because NGC3718's stellar population is mostly comprised of old K/M type stars²¹ and, partly, also due to the lower total integration time of the J band ($t_J = 300$ sec, $t_H = 660$ sec, and $t_{K_S} = 720$ sec). In turn, the lower flux leads to noisier isophote contours and, therefore, to higher uncertainties. The dust lane of NGC3718 is not expected to affect the central NIR light distribution to a large extent because it lies relatively far from the projection of the center (see section 2.4 and appendix B). Moreover, both in terms of structural size and illumination, the dominant component seen in the NIR images should be the stellar bulge of the galaxy, which appears to be largely relaxed, as the absence of large-scale contour deformations and the nearly round contour shape²² indicate.

Given the above, it is safe to consider that the average of the most prominent stable values of each (X_{center}, Y_{center}) coordinate pair should be a good first order approximation of the actual photo-center (i.e. the center of the stellar bulge) of NGC3718 in the three NIR bands. The uncertainties of the $(\bar{X}_{center}, \bar{Y}_{center})$ pairs are the quadratic addition

¹⁹IRAF is distributed by the National Optical Astronomy Observatories, which are operated by the Association of Universities for Research in Astronomy, Inc., under cooperative agreement with the National Science Foundation.

²⁰The fitted ellipses of a symmetric light distribution would point towards a common center and, as a result, the plots of figure 2.4 would closely resemble horizontal lines.

²¹The $V - K \sim 3$ color (NED) of NGC3718 suggests a dominant population of stars with $T_{eff} \sim 4000$ K (Ridgeway *et al.*, 1980).

²²The NIR ellipticities in the radial interval between $\sim 0.5 - 1.5$ arcsec range between $\sim 0.09 - 0.12$ in J band, $\sim 0.07 - 0.09$ in H band, and $\sim 0.03 - 0.07$ in K_S band.

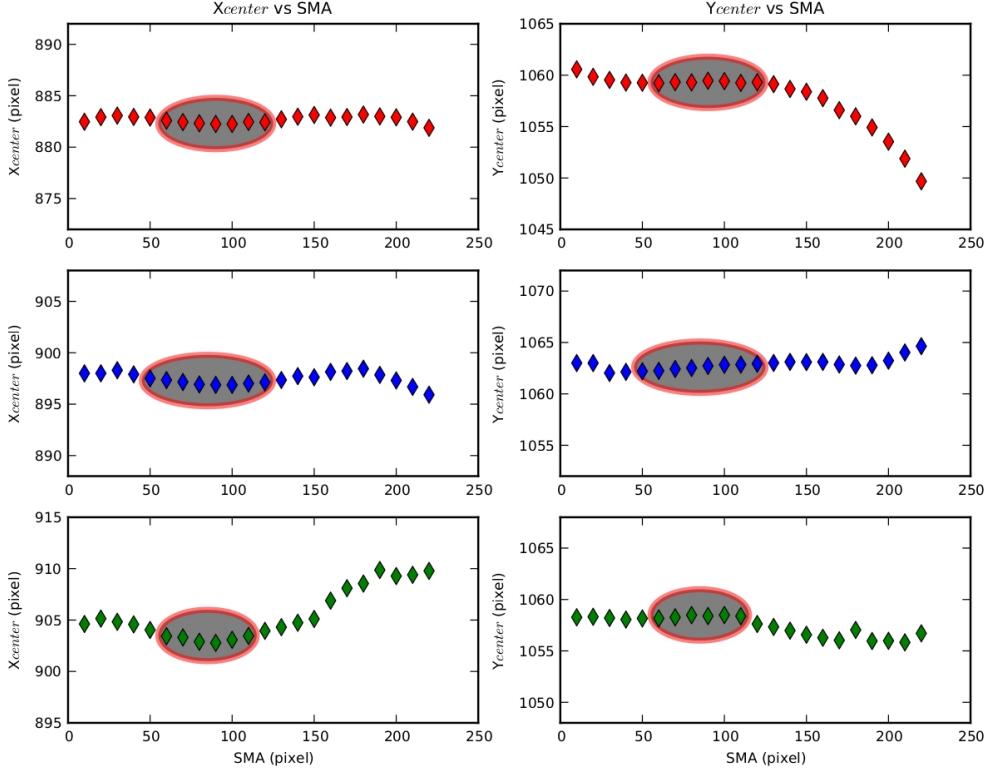


Figure 2.4: X (left column) and Y (right column) central coordinates indicated by the fitted ellipses versus their SMAs for the K_S (red/top row), H (blue/middle row), and J (green/bottom row) bands. The shaded elliptical regions indicate the most prominent stable values used for the derivation of the first order approximation photo-centers of NGC3718.

Table 2.1: First order approximation photo-centers.

Filter	\bar{X}_{center} (Pixel)	\bar{Y}_{center} (Pixel)	$\bar{dX}_{center}^{total}$ (mas)	$\bar{dY}_{center}^{total}$ (mas)
J	903.16	1058.36	3.4	2.2
H	897.10	1062.59	2.5	3.0
K_S	882.39	1059.33	1.5	1.3

Note. First order approximation of the \bar{X}_{center} and \bar{Y}_{center} of NGC3718 in each band in pixels, along with their corresponding uncertainties in mas, as suggested by the ellipse fitting process. 1 pixel equals 10 mas.

products of the standard deviation of the most prominent stable values with the average fitting uncertainties (\bar{dX}_{center} , \bar{dY}_{center}) as indicated by the ellipse task. The first order approximation photo-centers and their corresponding uncertainties are shown in table 2.1.

2.3.2 Pivot and subtract operation

Having a first order approximation of the center of the stellar bulge of NGC3718, it is interesting to further investigate the cause of the observed deviation in the Y_{center} coordinate of the K_S band. A clean bulge component should have a symmetrical bell-shaped light distribution (i.e. a Sérsic profile), as expected from all spherical/elliptical shapes that are projected on a 2-D surface. This should result in co-centered isophotes and, subsequently, in co-centered fitted ellipses.

So the following scheme is considered: A perfectly symmetrical spherical 3-D structure should look the same under any rotation around the perpendicular to the X-Y plane axis. Similarly, a symmetrical elliptical 3-D structure should look the same under $n \times \pi$ rotation, with n being an integer. So if one was to rotate such a structure around its center and subtract its 2-D projection from the 2-D projection of the unrotated structure itself, the result should be 0. Expanding this scheme for an isolated, undistorted, and perfectly symmetrical bulge, if one rotates and subtracts its 2-D projection from itself, one should receive only random noise without any obvious residual signal. More specifically, in the case of NGC3718 the projection of its bulge is slightly elliptical, so the above scheme is valid only under $n \times \pi$ (with $n = 1, 2, 3, \dots, n$) rotation around the first order approximation photo-centers that I derived earlier.

The process of pivot (π rotation) and subtract reveals strong residuals in the K_S and H bands (see figure 2.5), while in the J band the residuals are generally noisier.

2.3.3 Evaluating the centering process

Despite the fact that the implied uncertainties are of the order of a few mas (see table 2.1), the accuracy of the initial center estimations is further tested by repeating the pivot and subtract process, this time with the pivot points shifted by $(X_{center}^{init} \pm 1, Y_{center}^{init} \pm 1)$ and $(X_{center}^{init} \pm 0.5, Y_{center}^{init} \pm 0.5)$ in all bands. This way, a mesh of sixteen alternative neighboring pivot points, forming a rectangular (2×2 pixels²) grid around the initial center estimations, are tested. If the mean residual flux of a candidate $(X_{center}^i, Y_{center}^i)$ within the central 300×300 pixels² is smaller than the mean residual flux of the $(X_{center}^{init}, Y_{center}^{init})$ within the same region, then the candidate $(X_{center}^i, Y_{center}^i)$ is adopted as a better center estimation and the pivot and subtract process is iterated until the minimum mean central residual flux is reached.

This evaluation process reveals that the initial center estimations are surprisingly accurate— within ± 0.5 pixels (± 5 mas) per coordinate—, since the initial pivot points produced the minimum mean residuals in the central 300×300 pixels². The tested ± 0.5 pixels accuracy is slightly larger than the statistical uncertainties of the initial statistical analysis (see table 2.1), it is adopted, however, as a more conservative uncertainty estimation. Examples of the residuals from the alternative pivot points for the H band are shown in

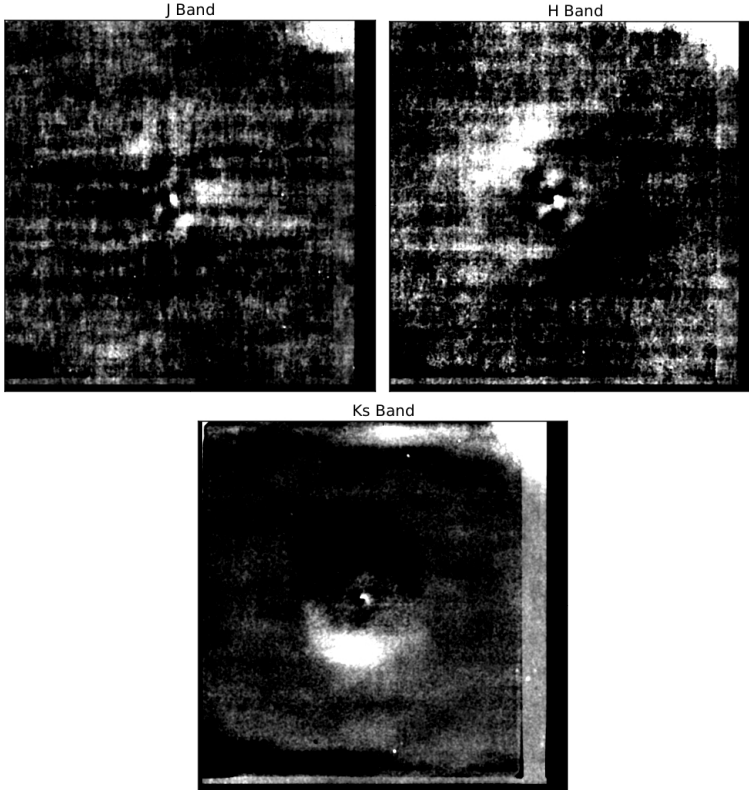


Figure 2.5: Residual images– from the pivot and subtract operation– for the J(top left), H(top right), and K_S (bottom middle) bands. All images are smoothed with a 10-pixel Gaussian kernel. The mean peak residual fluxes as percentages of NGC3718’s mean peak fluxes are $\sim 4.5\%$, $\sim 3.0\%$, and $\sim 3.4\%$ for the J, H, and K_S bands, respectively.

figure 2.6. The alternative pivot points produce, generally, much less well defined residuals especially in the central region, where the bright features clearly indicate that incorrect pivot points have been used. Large-scale asymmetries, however, like the extended light excess NE from the center (see figure 2.6) could still be traced and removed irrespective of the chosen pivot points.

The residual images (see figure 2.5) are then subtracted from the initial images (see figure 2.3) in order to correct the NIR light distribution for any asymmetries. The resulting NIR light distribution in all bands (see figure 2.7) is clearly more symmetrical and, generally, better defined.

It should be noted at this point that the residual images represent asymmetries between anti-diametrical parts of the NIR light distribution. If inclination and/or tilt are present, then, while moving away from the center, the line-of-sight light path, and, there-

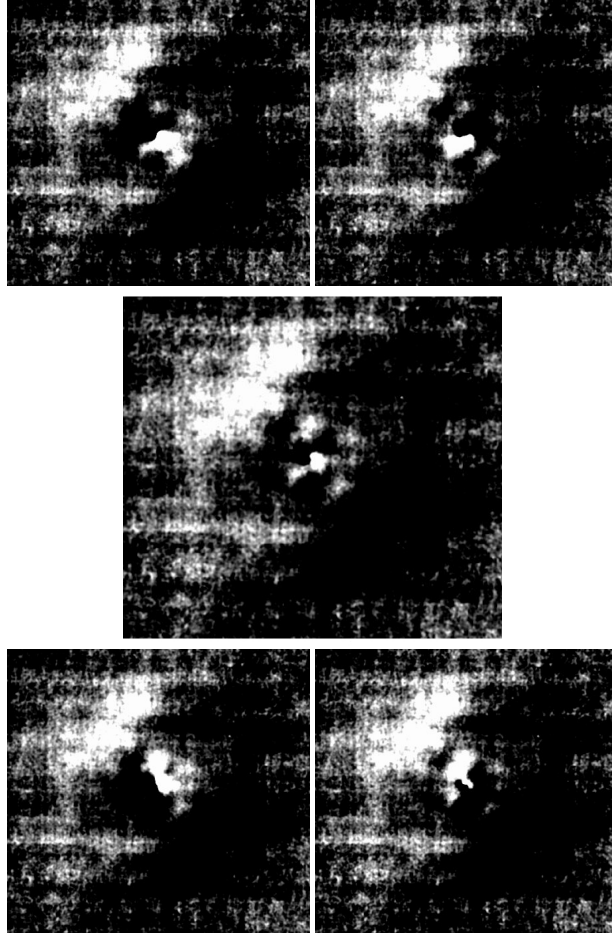


Figure 2.6: Examples of smoothed residual H band images after rotation around pivot points shifted by $(X_{center}^{init} - 0.5, Y_{center}^{init} + 0.5)$ (upper left), $(X_{center}^{init} + 0.5, Y_{center}^{init} + 0.5)$ (upper right), $(X_{center}^{init}, Y_{center}^{init})$ (center), $(X_{center}^{init} - 0.5, Y_{center}^{init} - 0.5)$ (lower left), and $(X_{center}^{init} + 0.5, Y_{center}^{init} - 0.5)$ (lower right).

fore, the brightness difference between anti-diametrical parts of the galaxy will become increasingly larger. This means that it is not safe to treat the large-scale asymmetries as light over-densities with a physical meaning. On the other hand, as one moves towards the center, these effects will become increasingly smaller and, subsequently, the small-scale asymmetries should mainly represent true light- and mass- over-densities²³. This, in turn, suggests that the symmetrical light images and the residual maps can be safely

²³While approaching the center, the brightness difference between anti-diametrical parts of the NIR light distribution will become increasingly smaller. Given that the photo-centers are accurate, these residuals should represent actual light density variations.

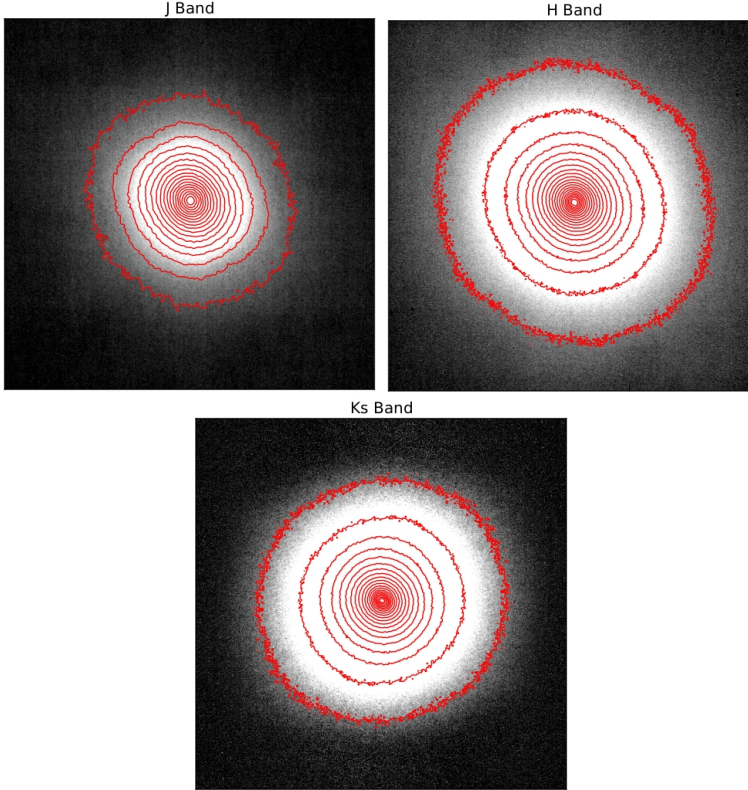


Figure 2.7: Symmetrical light images—after the removal of the residuals—for the *J* (top left), *H* (top right), and K_S (bottom middle) bands.

used for scientific measurements, as long as their use is restricted to small scales²⁴.

2.3.4 Matching the angular resolution and calibrating the flux

All the NIR images of figure 2.3 are aligned with respect to the *J* band, using the center estimations derived and tested in the previous paragraphs. The angular resolution of the data is also matched by convolving the images taken in better seeing conditions (namely, *H* and K_S bands) to the image taken with the worst one (i.e. *J* band). The seeing conditions are validated for each band by measuring the FWHMs of appropriate PSF-reference stars in the data set. The final Gaussian kernels used for convolution equal the quadratic difference of the better from the worse seeings, in the following way:

$$\delta_{FWHM}(H) = \sqrt{[FWHM(J)]^2 - FWHM(H)^2} \approx 9.8 \quad (2.2)$$

²⁴However, following Ockham's razor, throughout this chapter I avoid their use as much as possible in favor of credibility.

$$\delta_{FWHM}(K_S) = \sqrt{[FWHM(J)]^2 - FWHM(K_S)^2} \approx 10.3 . \quad (2.3)$$

Finally, I use standard stars for each NIR band in the data set in order to derive appropriate zero points (ZP), with which I perform the calibration of NGC3718's flux according to

$$m_{Sub.}^i = Z.P.^i_{Sub.} - 2.5 \log\left(\frac{\text{Counts}_{Sub.}^i}{\text{Exp.Time}_{Sub.}^i}\right) , \quad (2.4)$$

where m is the apparent magnitude and the index i indicates the $J/H/K_S$ bands, respectively.

2.3.5 Astrometric uncertainties

In order to astrometrically calibrate the Subaru data, I align the Subaru J band image with a re-sampled and re-scaled copy of the SDSS z band image²⁵. The SDSS z band is chosen mainly because the SDSS is currently the most accurate—in astrometric terms—survey available (Pier *et al.*, 2003), but also because its central wavelength (0.9134 μm) is the closest to the Subaru J band (1.220 μm), which should ensure the best possible astrometric calibration, since the photo-centers of the old stellar populations of NGC3718's bulge are expected to coincide in neighboring NIR bands (see appendix C and footnote 21). The intrinsic SDSS astrometric uncertainties are calculated according to the instructions given in the SDSS online documentation, while the total astrometric uncertainty budget of the Subaru data is shown in table 2.2.

2.4 The NIR color maps

Having the NIR images of 2.3 aligned and, astrometrically and flux, calibrated, the $J - H$ and $H - K_S$ NIR color maps are produced. The NIR color maps can be a very important tool because they provide crucial information about the distribution of the colors of a galaxy, e.g. whether the incoming light originates from an “ordinary” stellar population or it also has contribution(s) from a black-body and/or a power law component and whether reddening affects the colors (Glass and Moorwood, 1985) or not. The colors of ordinary galaxies were estimated by Glass (1984) to be $J - H = 0.78$ and $H - K = 0.22$. Light in the J band comes mainly from stars, while in the K_S band light can be produced from both hot dust and stars. In this context, a black-body of temperature below the sublimation temperature

²⁵More specifically, a $51 \times 51 \text{ pixels}^2$ (FoV $20 \times 20 \text{ arcsec}^2$) section of the SDSS z band image centered on NGC3718's nucleus is magnified by ~ 40 times, i.e. the scale ratio of the SDSS and Subaru data, namely, ~ 0.4 and $\sim 0.01 \text{ arcsec pixel}^{-1}$, respectively. The new— $2040 \times 2040 \text{ pixels}^2$ —SDSS z band replica image is, subsequently, aligned with the—also trimmed to $2040 \times 2040 \text{ pixels}^2$ —Subaru J (and, therefore, with the H and K_S) band(s), following the method of section 2.3.1.

Table 2.2: Astrometric uncertainties and coordinates.

uncertainties:	SDSS (mas)	z - J (mas)	Cent./Shift (mas)	e-Merlin (mas)	Total (mas)
<i>J</i> band					
$\delta(RA)$	42.5	10.8	5.0	4.1	44.3
$\delta(Dec)$	41	11.0	5.0	4.1	42.9
<i>H</i> band					
$\delta(RA)$	42.5	10.8	7.1	4.1	44.6
$\delta(Dec)$	41	11.0	7.1	4.1	43.2
K_S band					
$\delta(RA)$	42.5	10.8	7.1	4.1	44.6
$\delta(Dec)$	41	11.0	7.1	4.1	43.2
RA (Bulge)			Dec (Bulge)		
11:32:34.8515 \pm 0.0051			+53:04:04.475 \pm 0.044		
RA (Red blob)			Dec (Red blob)		
11:32:34.8550 \pm 0.0051			+53:04:04.512 \pm 0.044		
RA (Radio)			Dec (Radio)		
11:32:34.8497 \pm 0.0005*			+53:04:04.527 \pm 0.004		

Note. Upper table: The total astrometric uncertainties involved for the three NIR bands. Columns: 1) The total intrinsic SDSS z band astrometric uncertainties, 2) SDSS z / Subaru J bands alignment uncertainties, 3) centering and/or shifting uncertainties, i.e. during the centering of the J , H , and K_S images and the J/H and J/K_S alignments, 4) the intrinsic e-Merlin radio map astrometric uncertainties, 5) total uncertainty in each NIR band, i.e. quadratic addition of all the above. Lower table: From top to bottom, the position of the peak flux of the a) stellar bulge of NGC3718, b) offset red blob, and c) offset e-Merlin 6 cm radio emission.

*This position for the peak of NGC3718's radio emission was calculated using the coordinates of J1146+5356 quoted in section 2.2.2. Assuming the calibrator coordinates used in earlier e-Merlin observations, then the RA and Dec of NGC3718's peak radio flux become $\alpha_{2000} = 11 : 32 : 34.8534 \pm 0.0005$ and $\delta_{2000} = +53 : 04 : 04.523 \pm 0.004$, which are in very good agreement with the position published by [Krips et al. \(2007\)](#).

of dust, namely ~ 1500 K, will radiate at $\lambda \gtrsim 1.9 \mu\text{m}$, affecting mostly the K_S band, but potentially also the H band ($\lambda_{\text{central}} = 1.63 \mu\text{m}$) to some extent. This indicates that the $J-H$ map is a better probe of extinction phenomena because the, already sublimated, dust is acting mostly as a scattering source, while the $H-K_S$ map is a better probe of hot dust emission. The NIR color maps are shown in figure 2.8.

Both NIR color maps of figure 2.8 are reasonably symmetric. An approximately elliptical region of NIR excess can be seen around the nucleus in the $J-H$ map, extending from south-east (SE) to NW. This could be the result of the presence of dust around the nucleus, which causes some amount of local extinction. Similarly, the $H-K_S$ map also shows an elliptical NIR excess region around the center and along the same orientation, its color (i.e. $H-K_S \sim 0.5$), however, indicates that there is contribution to the emission by

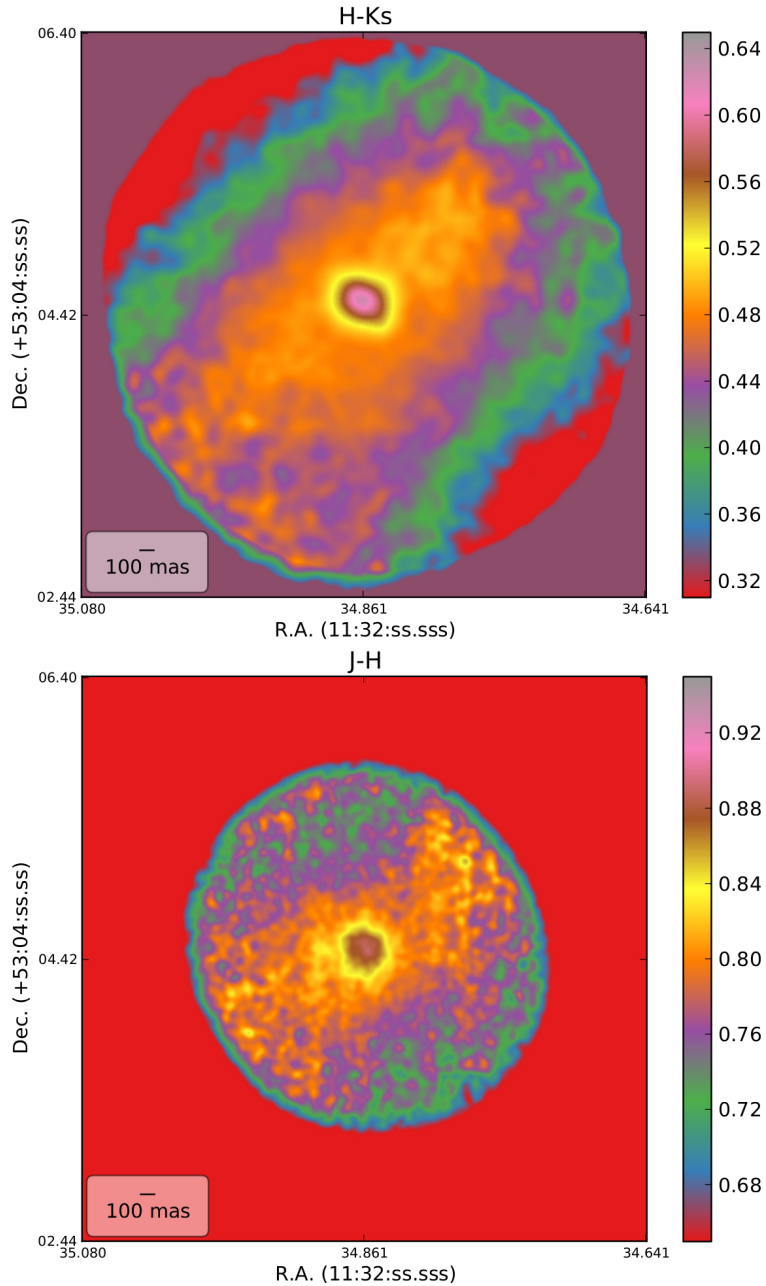


Figure 2.8: The $H - K_S$ (top) and $J - H$ (bottom) NIR color maps .

the presence of hot dust. Most importantly though, the absence of a large-scale constant color gradient from both NIR maps indicates that the extension of the dust lane– located

towards the south-west (SW) of the stellar bulge (see appendix B)– does not affect our view towards the center of the stellar bulge.

The symmetry of the NIR color maps is clearly evident in the radial plots of figure 2.9. Measuring the NIR color maps along four different directions (see caption of figure 2.9) confirms that there is no sign of a large-scale constant color gradient. Such a gradient would appear in the form of an asymmetry of these curves with respect to the center and would imply that an amount of non-uniformly distributed foreground dust is present²⁶. The only form of asymmetry visible in these plots is between the blue and red profiles outside the central ~ 0.5 arcsec. This is, likely, due to the perpendicularity of the different measurement directions, which map the center of the bulge along the major and minor axes of the NIR elliptical excess, however, both components are symmetrical with respect to the center.

The most interesting feature of the NIR color maps, however, is that the peak of the red blob emission in the $H - K_S$ map is offset by ~ 50 mas from the center of the underlying stellar bulge. In order for this to be more easily visible, I use the images of figure 2.7 to produce the “symmetrical” $H - K_S$ map. The peak contours of the symmetrical map– representing the center of the stellar bulge– are then over-plotted alongside the peak contours of the $H - K_S$ map of figure 2.8, as shown in figure 2.10. Moreover, the same (i.e. in terms of length and orientation) offset is also extracted by applying a high pass filter on the K_S image of figure 2.3, which strongly implies that this is not the result of the geometric transformations during the alignment of the NIR images. The central positions of the stellar bulge and of the offset red blob– expressed in RA and Dec– are shown in table 2.2.

2.4.1 Decomposing the NIR light

In order to decompose the light of NGC3718, the model of mixtures of ordinary galaxy colors with black-bodies at various temperatures from [Glass and Moorwood \(1985\)](#) (see caption of figure 2.11) is used. I azimuthally average measurements of the innermost ~ 0.5 arcsec of the nucleus of NGC3718, using five equally spaced radius bins with a ~ 50 mas step. This reveals (see zoomed-in section of figure 2.11) a gradual drop in the light mixture from a 50% stellar - 50% dust at $T_{100} \sim 1000$ K in the innermost ~ 100 mas, to a 60% stellar - 40% dust at $T_{200} \sim 800$ K in the innermost ~ 200 mas, to a 65% stellar - 35% dust at $T_{300-500} \sim 700 - 500$ K in the innermost $\sim 300 - 500$ mas, indicating the presence of significant contribution from hot dust in the central region of NGC3718. This, in turn, suggests an environment ideal for SMBH accretion.

²⁶A non-uniform (e.g. progressively thinner) northwards extension of the dust lane, would reflect the presence of progressively excessive amounts of dust towards the S/SW compared to the N/NE of the stellar bulge. In turn, this would lead to excessive reddening, which would create an asymmetry in the plots of figure 2.9, as follows: progressively more dust \rightarrow progressively higher reddening \rightarrow progressively lower J (H) flux \rightarrow progressively higher $J - H$ ($H - K_S$) values towards the S/SW. However, a uniform “film” of foreground dust causing even reddening across the bulge could be present, but this should not– qualitatively at least– affect the result’s interpretation.

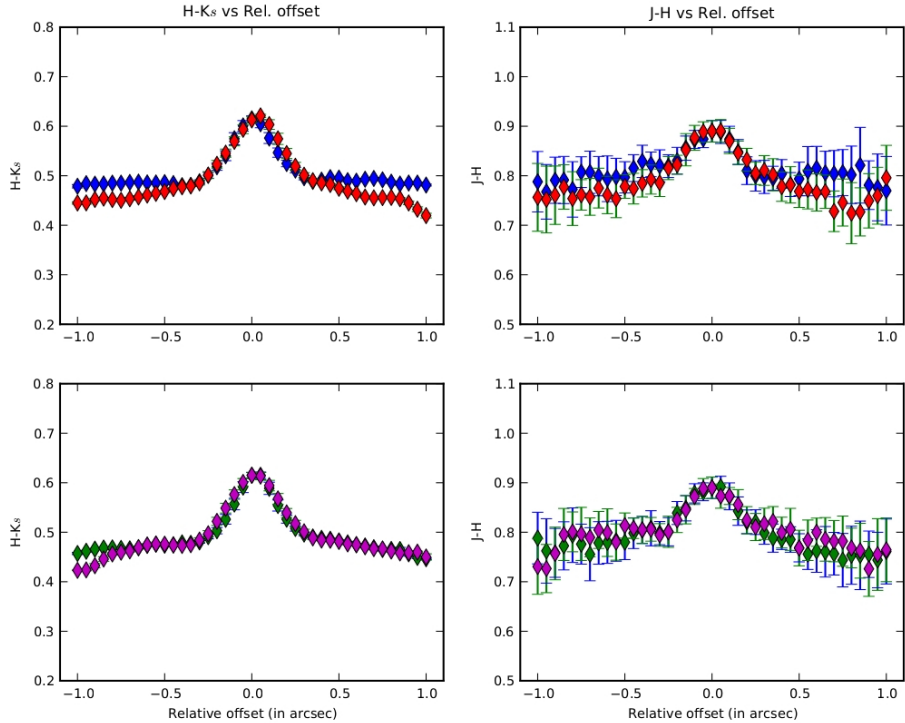


Figure 2.9: Radial profiles of the $H - K_S$ (two left hand panel plots) and $J - H$ (two right hand panel plots) color maps. Measurements are performed along two perpendicular sets of directions measured counterclockwise from the north, namely, $120^\circ/210^\circ$ (blue and red points, respectively - upper row) and $170^\circ/260^\circ$ (green and magenta points, respectively - lower row). Negative \rightarrow positive relative offset represents a $S(E,W) \rightarrow N(W,E)$ direction.

2.4.2 The e-Merlin radio map

In figure 2.12, I present the 6 cm radio e-Merlin map, which provides high angular resolution (~ 100 mas) and a pointing accuracy of ~ 4.1 mas (see section 2.2.2). The outer contours are set to $\sim 4\sigma$ sigma above the background ($\sim 2-3\%$ of the peak flux) and, therefore, the flux density enclosed within these contours is considered to be true signal detection from the extended radio structures of NGC3718, at least in the position angle defined by the red dashed line in figure 2.12.

Over-plotting the radio map on the $H - K_S$ NIR map reveals yet another very interesting result. As shown in figure 2.13, the position of the peak of the radio emission appears to be closer to the position of the offset red blob (i.e. within the astrometric uncertainties) than it is to the center of the stellar bulge. This is an additional indication that the SMBH is not located at the center of the bulge, but it is offset by ~ 50 mas, which, translated to physical distance, reflects a projected separation of ~ 4.25 pc at the distance of NGC3718 (i.e. \sim

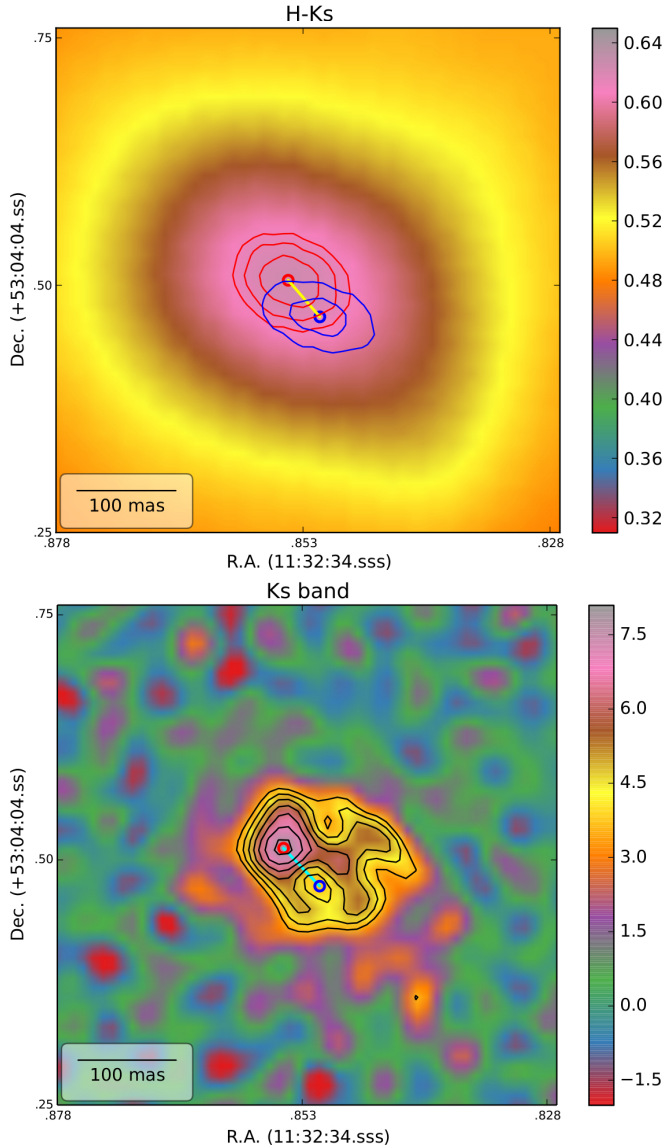


Figure 2.10: Top: Closeup of the $H - K_S$ map. The contours of the red blob (in red) are offset from the peak contours of the symmetrical $H - K_S$ map (in blue). Bottom: Closeup of the high pass filtered K_S band image. The peak flux of the image is offset from the K_S band photo-center. In both images, the red circle marks the peak of the offset red blob, while the blue circle marks the center of the underlying stellar bulge. Finally, the radii of the blue and red circles represent their positional uncertainties, namely, ~ 7 mas, while the yellow(top)/cyan(bottom) line represents the displacement of the offset, namely, ~ 50 mas.

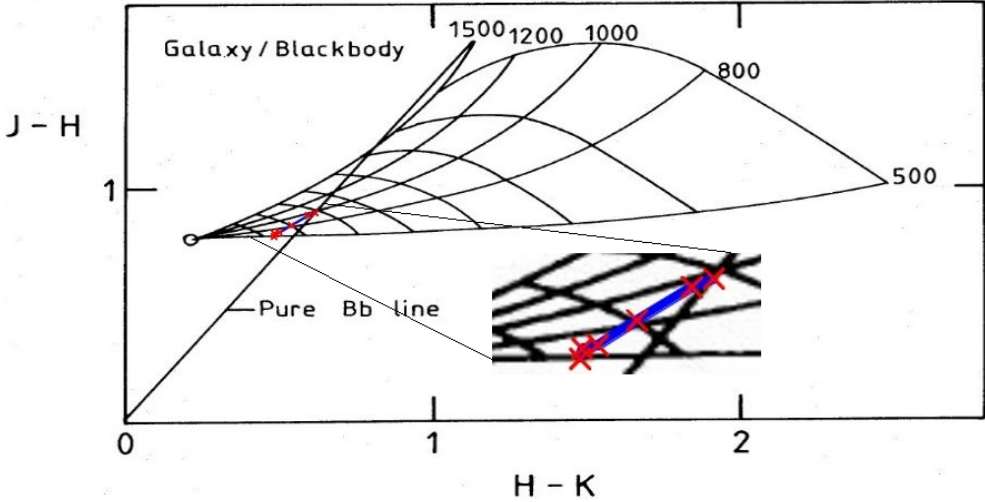


Figure 2.11: The model of mixtures from *Glass and Moorwood (1985)*. Moving away from the open black circle at $J - H = 0.78$ and $H - K = 0.22$ (i.e. ordinary galaxy colors) and along the horizontal lines in the grid of mixtures, indicates an increase (by 10% per vertical line) in the percentage of contribution from hot dust emission, while moving along the vertical lines of the model reflects an increase in the temperature of this dust component in the range $T \sim 500 - 1500$ K.

17.4 Mpc). Moreover, the presence of radio emission is not a surprise, since NGC3718 has been previously identified as an LLAGN. The closer proximity of the radio emission to the offset red blob could, therefore, imply that the SMBH accretes matter normally, but it does so being displaced from the center of the bulge. It has to be reminded, however, that the radio emission offset is of the order— though slightly larger— of the coordinate uncertainties quoted in table 2.2, which suggests that a coincidence of the radio emission with the offset red blob could realistically be true. The position of the peak radio emission— expressed in RA and Dec— is shown in table 2.2.

Nonetheless, the current theory predicts the existence of spatial offsets (potentially coincident with offset AGNs, e.g. in the case of SMBH recoils (e.g. *Sijacki et al., 2011; Komossa, 2012*). In short, when a merger of two galaxies takes place, the SMBHs that reside in their centers will form a binary (*Begelman et al., 1980*), which will eventually coalesce due to emission of gravitational waves from the two members (e.g. *Bekenstein, 1973*), while the newly formed SMBH will recoil because the gravitational wave emission will, likely, be anisotropic (see section 1.2.2). Discussion on this subject, however, is resumed later on, as more evidence are necessary in order to favor such a scenario for NGC3718.

The ~ 0.5 arcsec NW candidate jet component identified by *Krips et al. (2007)* in their Merlin 18 cm map, is also present in the 6 cm e-Merlin map (see figure 2.12). Additionally,

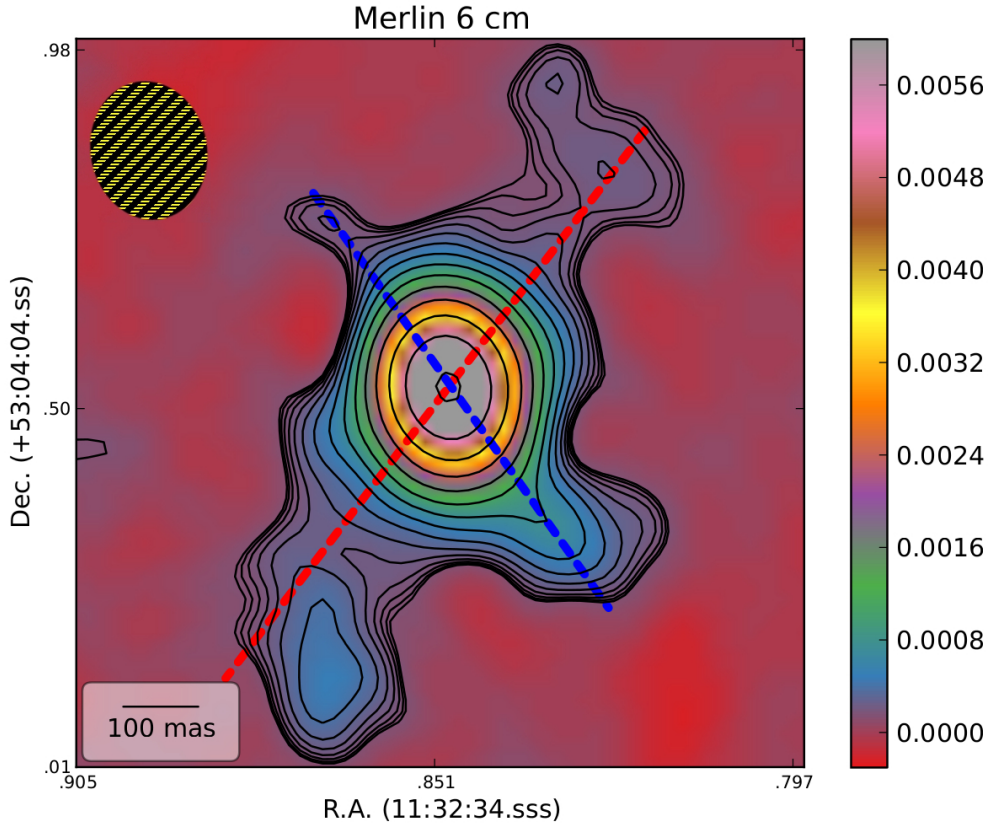


Figure 2.12: The *e*-Merlin 6 cm radio map. The third innermost contour represents the $\sim 40 - 50\%$ of the peak flux, while the outer contours ($\sim 4\sigma$ above the local background) represent $\sim 2 - 3\%$ of the peak flux. The size of the beam is shown in the upper left corner, while the red and blue dashed lines indicate the position angles of the SE-NW and the NE-SW small-scale candidate bipolar extended structures, respectively.

the latter shows a second, anti-diametrically placed ~ 0.5 arcsec extension towards the SE. This could be a counterpart of the NW jet component, since both extensions have the same length and lie along the same orientation. Finally, a brighter but less extended structure towards the SW²⁷, as well as, a fainter tail-like structure towards the NE, both with a length of ~ 0.3 arcsec and along the same orientation, could (potentially) indicate the presence of a small-scale X-shaped radio structure. These are thought to be associated either with the jet emitting members of a close SMBH binary (Lal and Rao, 2007), or with “spin-flip” processes in SMBH recoils (e.g. Merritt and Ekers, 2002; Liu *et al.*, 2012).

²⁷In the position angle defined by the blue dashed line, which could be the westward candidate jet component identified by Krips *et al.* (2007) in their EVN 6 cm map. The same structure aligns also with the arcmin scale-jet-like extension in the VLA observations of Condon (1987).

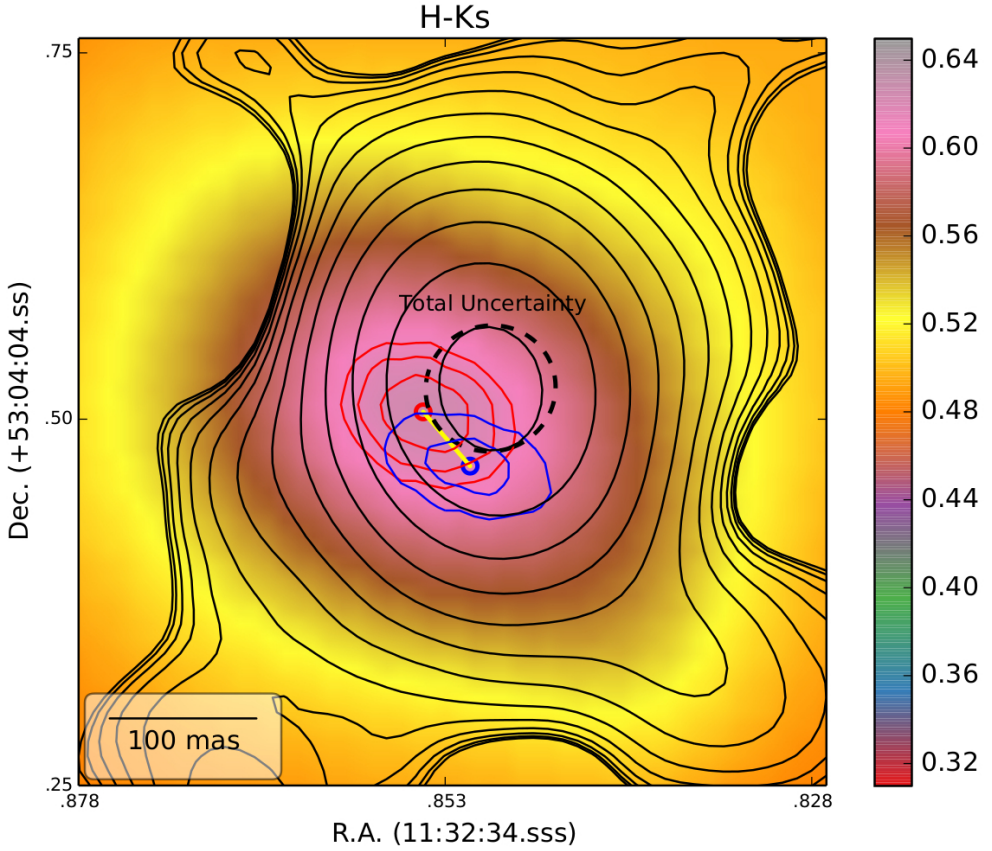


Figure 2.13: The 6 cm e-Merlin radio contours over-plotted on a copy of the upper image of figure 2.10. The radii of the blue and red circles represent the uncertainties of each position, namely, ~ 7 mas, while the black dashed ellipse represents the total coordinates uncertainty shown in table 2.2. (Note: This is the position of the radio emission quoted in table 2.2. The same image with the position quoted in *Krips et al. (2007)* is shown in appendix D, figure D.1).

Finally, the measured 6 cm e-Merlin peak and integrated fluxes of NGC3718 are 8.85 ± 0.07 mJy and 9.97 ± 0.08 mJy, respectively. Both of these, therefore, show an average increase of $\sim 65\%$ ²⁸ with respect to the 6 cm Merlin fluxes published by *Krips et al. (2007)*, namely, 5.3 ± 0.1 mJy and 6.1 ± 0.3 mJy, respectively. This could be an indication that NGC3718 is a variable radio source, which is consistent with SMBH accretion.

²⁸I.e. $\sim 67\%$ for the peak flux and $\sim 63\%$ for the integrated flux.

2.5 Scaling relations and classification of NGC3718

2.5.1 To bulge or not to bulge?

Perhaps the most important relations between the properties of a host galaxy and its SMBH are the $M_{\text{BH}} - \sigma$ and $M_{\text{BH}} - L$, widely known as the scaling relations. These relate the stellar velocity dispersion and the luminosity of the stellar bulge of a galaxy, respectively, with the mass of its central SMBH, implying a certain degree of co-evolution.

It is possible to make an estimation of the absolute magnitude $M_{K_S, \text{bulge}}$ of NGC3718 from the Subaru K_S band directly. Given, however, that no decomposition into different components (i.e. disk, bulge etc.) is performed, the contaminated bulge magnitude derived M_{BH} should be viewed as an upper limit. The bulge magnitude is estimated using aperture photometry on the K_S band images (see figures 2.3 and 2.7) of NGC3718, with apertures of three different sizes (i.e. 3, 4, and 5σ above the background), resulting in an average aperture of $r_{\text{aper.}} \sim 3 \text{ arcsec}^{29}$. The flux of those measurements is then averaged and a (rather large) uncertainty of 0.2 mag^{30} is assigned. The K_S band absolute magnitude of NGC3718 is

$$M_{K_S, \text{bulge}} = -21.1 \pm 0.2 \text{ mag} .$$

For an estimation of the velocity dispersion, however, spectroscopic information of NGC3718 is necessary. The Palomar AGN spectroscopic survey (Ho *et al.*, 1997a) extracted several useful parameters for a number of objects, including the $FWHM[NII] = 371 \text{ km s}^{-1}$ line of NGC3718. Assuming a Gaussian profile for the spectral lines, an estimation for the velocity dispersion is $\sigma \approx 157 \text{ km s}^{-1}$, using $FWHM = 2\sqrt{2\ln(2)}\sigma \approx 2.355\sigma$. The $[NII]\lambda\lambda 6583\text{\AA}$ line, however, is considered to be a better tracer for the motion of the ionized gas. A number of authors (e.g. Pignatelli *et al.* (2001), Caldwell *et al.* (1986)) suggest that the gas may rotate at different speeds than the stars. Ho (2009) combined gas and stellar velocity dispersions and they found that, generally, σ_{gas} and σ_{\star} correlate well. Ho *et al.* (2009) measured the stellar velocity dispersion of NGC3718 to be $\sigma = 158.1 \pm 9.6 \text{ km s}^{-1}$, using the $Ca + Fe$ absorption feature at 6495\AA , a value that is adopted for all relevant calculations in this chapter. These measurements suggest a $\sigma_{\text{gas}}\sigma_{\star}^{-1} \sim 1$ for NGC3718. The authors argue that “as the gas derives principally from mass loss from bulge stars, its kinematics should generally track the kinematics of the stars. But because the gas is collisional and experiences hydrodynamical drag against the surrounding hot medium, we expect it to be kinematically slightly colder than the stars. In the absence of additional energy input from other sources, we anticipate $\sigma_{\text{gas}}\sigma_{\star}^{-1} \lesssim 1$, as observed. As additional energy is injected into the system, for example from activation of the central black hole, the gas gains energy, to the point that σ_{gas} approaches or even overtakes σ_{\star} ”. This picture is supported

²⁹The average flux difference of the images of figure 2.3 and those of figure 2.7 is $\sim 0.1 \text{ mag}$, which is considered to be negligible.

³⁰To account for systematic uncertainties in the calibration process, for statistical deviations in the measurements etc.

by the fact that NGC3718 is an LLAGN. This could be seen as an indirect indication that the SMBH of NGC3718 provides enough energy (i.e. through AGN feedback) to heat up the gas and cause the very good agreement between σ_{gas} and σ_* .

Having estimations for both the bulge luminosity and the stellar velocity dispersion, I use the $M_{BH} - M_{K_S, bulge}$ and $M_{BH} - \sigma$ relations from [Kormendy and Ho \(2013\)](#) to calculate the SMBH mass, namely:

$$\log \frac{M_{BH}}{10^9 M_\odot} = -(0.265 \pm 0.050) - (0.488 \pm 0.033)(M_{K_S, bulge} + 24.21) \quad (2.5)$$

$$\log \frac{M_{BH}}{10^9 M_\odot} = -(0.509 \pm 0.049) + (4.384 \pm 0.287) \log \left(\frac{\sigma}{200 \text{ km s}^{-1}} \right) . \quad (2.6)$$

The SMBH mass suggested by equation 2.5 is

$$M_{BH}^{M_{BH}-M_{K_S, bulge}} = 1.65_{-0.82}^{+1.64} \times 10^7 M_\odot ,$$

while the SMBH mass suggested by equation 2.6 is

$$M_{BH}^{M_{BH}-\sigma} = 1.11_{-0.54}^{+1.05} \times 10^8 M_\odot .$$

Although equations 2.5 and 2.6 were derived by [Kormendy and Ho \(2013\)](#) using the same galaxy sample, they suggest SMBH masses that differ by almost an order of magnitude in the case of NGC3718. Adopting the velocity dispersion derived M_{BH} as a more robust estimation and forcing an agreement between equations 2.5 and 2.6, a minimum brightness difference of

$$\delta M_{K_S} \sim 1.7 \text{ mag}$$

is revealed. In other words, NGC3718's bulge should be ~ 4.8 times brighter in order to justify the SMBH mass suggested by the velocity dispersion of its stars.

But what could be the cause of the disagreement between the scaling relations, when NGC3718's values are used? A first approach is that NGC3718 does not have a bulge but a pseudo-bulge³¹, so equations 2.5 and 2.6 do not apply ([Kormendy et al., 2011](#)). The current classification of NGC3718 as an SB(s)a pec implies that it has a bar and barred galaxies preferably have pseudo-bulges ([Kormendy and Kennicutt, 2004](#)).

³¹A pseudo-bulge is a dense central stellar region similar to a classical bulge, but it has properties closer to a disk-like object (i.e. mainly supported by rotation and not by pressure from random stellar motions). They are believed to form through different mechanisms than classical bulges do (i.e. through secular processes and not in galaxy mergers).

In contrast, the gas dynamics of NGC3718 has been studied by several authors (e.g. [Pott et al., 2004](#); [Krips et al., 2005](#); [Sparke et al., 2009](#)), who successfully described it using tilted rings models and concluded that the gas orbits close to the center are nearly edge-on. [Sparke et al. \(2009\)](#) suggest that classifying NGC3718 as a barred galaxy is misleading. They interpret the apparent nuclear bar as the effect of looking through a dusty gas disk/ring (the projection of which is the dust lane) on polar orbit around a nearly face-on stellar disk. Additionally, they do not detect any HI emission on the plane of rotation of the stellar disk, which implies that it is probably free of cold gas, a characteristic usually seen in lenticular galaxies. Furthermore, the spectrum of NGC3718 revealed the presence of broad $H\alpha$ emission ([Ho et al., 1997b](#)). This suggests that we have a relatively direct view towards the nucleus of the host galaxy, which, in turn, has to be closer to face-on. [Sparke et al. \(2009\)](#) classify NGC3718 as a polar ring galaxy, a rare type of objects often hosting lenticular galaxies. The latter—being early-type objects—have many kinematic and other properties in common with elliptical galaxies. The Subaru data also favor this picture, since there are no obvious traces of a nuclear bar. The elliptical region surrounding the nucleus (see $H - K_S$ map, figure 2.8) looks more like a nearly face-on disk rather than a nuclear bar.

Moreover, NGC3718’s bulge does not fulfill, at least, three of the criteria of [Kormendy and Kennicutt \(2004\)](#) to be classified as a pseudo-bulge:

- i Following [Kormendy and Bender \(2013\)](#), the Faber-Jackson relations for core and coreless ellipticals suggest

$$\frac{L_V}{10^{11}L_\odot} = (0.79 \pm 0.11) \left(\frac{\sigma}{250 \text{ km s}^{-1}} \right)^{8.33 \pm 1.24} \rightarrow \sigma \sim 199 \text{ km s}^{-1}. \quad (2.7)$$

$$\frac{L_V}{10^{11}L_\odot} = (0.67 \pm 0.10) \left(\frac{\sigma}{250 \text{ km s}^{-1}} \right)^{3.74 \pm 0.21} \rightarrow \sigma \sim 158 \text{ km s}^{-1} \quad (2.8)$$

The kinematic properties of NGC3718 ([Jog and Chitre, 2002](#)) imply that a random motion supported bulge is present (see section 2.1). The observed velocity dispersion ([Ho et al., 2009](#)) seems to be, generally, in good agreement with both Faber-Jackson relations (given their large scatter), although it matches that of a coreless elliptical (equation 2.8) better. The observed σ , however, is by no means significantly smaller than the σ predicted by the Faber-Jackson relations, a fact that would indicate the presence of a rotationally supported pseudo-bulge. As noted by [Kormendy and Ho \(2013\)](#), “classical bulges are essentially equivalent to coreless ellipticals”, a picture consistent with NGC3718’s classification as a lenticular galaxy.

- ii There are no signs of a nuclear bar.

- iii There is no significant star formation³² (Sparke *et al.*, 2009).

The above indicate that NGC3718 behaves similarly to an elliptical galaxy and, therefore, it is reasonable to assume that the host galaxy - SMBH mass scaling relations should be applicable. So why do they point towards different M_{BH} ?

2.5.2 A light “deficit” or a σ “surplus”?

Since equations 2.5 and 2.6 are derived by Kormendy and Ho (2013) using the same galaxy sample, it is relatively safe to assume that they should, more or less, point towards similar SMBH masses. As noted earlier (see section 2.5.1), σ is considered to be a more accurate measurement than $M_{K_S, bulge}$ because it shows very good consistency when estimated from two different linewidths and the Faber-Jackson relation.

The first choice therefore, is to investigate the robustness of $M_{K_S, bulge}$. A surface brightness profile of NGC3718 is constructed from a joined data set consisting of the Subaru³³ and 2MASS³⁴ K_S band data against the radius, in order to get a better understanding of the light distribution. For this purpose IRAF’s task ellipse is used once again, to obtain an azimuthally averaged surface brightness profile of NGC3718 (see figure 2.14). A number of authors (e.g. Graham *et al.*, 2003; Kormendy *et al.*, 2009) have argued that fitting a Sérsic profile to the outer parts of the surface brightness profile of an early-type galaxy and extrapolating it inwardly can accurately describe its light distribution.

Following the aforementioned scheme, I fit the combined Subaru and 2MASS K_S data set of NGC3718. A combination of a Sérsic component for the bulge (Sérsic index $n = 4.85$) with a dual exponential disk component (scale lengths $R_S^{disk1} \sim 7$ arcsec and $R_S^{disk2} \sim 60$ arcsec, respectively) provides the best description of the data, as presented in figure 2.14. The lower limit of the fitting range (~ 50 arcsec) is chosen based on the uncertainties of the 2MASS data³⁵. With the lower limit fixed, the upper limit is subsequently determined through χ^2 minimization in the radial range between the candidate upper limit and ~ 20 arcsec. This strategy is chosen in order to minimize the fit with respect to the higher SNR data points³⁶. The best fit is obtained for a radial range between $\sim 1.5-50$ arcsec (i.e. ~ 500 data points) with a $\chi^2 \sim 2$. The modeled magnitude of the bulge is $M_{K_S, bulge} \sim -22.85$ mag (i.e. $m_{K_S, bulge} \sim 8.35$ mag). Putting this “recovered” magnitude into equation 2.5 suggests an M_{BH} of

$$M_{BH}^{M_{K_S, bulge}^{Sérsic}} = 1.18_{-0.59}^{+1.17} \times 10^8 M_{\odot} .$$

³²Examination of GALEX near and far UV images reveals that NGC3718’s UV flux is ~ 1 order of magnitude less than the flux of the starburst archetype NGC4449, indicating some amount of star formation, which, however, is not high enough to characterize NGC3718 as a starburst galaxy, supporting the view of Sparke *et al.* (2009).

³³For the innermost ~ 2.5 arcsec.

³⁴From ~ 2.5 to ~ 70 arcsec.

³⁵The flux is $\sim 2\sigma$ above the background at ~ 50 arcsec.

³⁶The flux is $\sim 6\sigma$ above the background at ~ 20 arcsec.

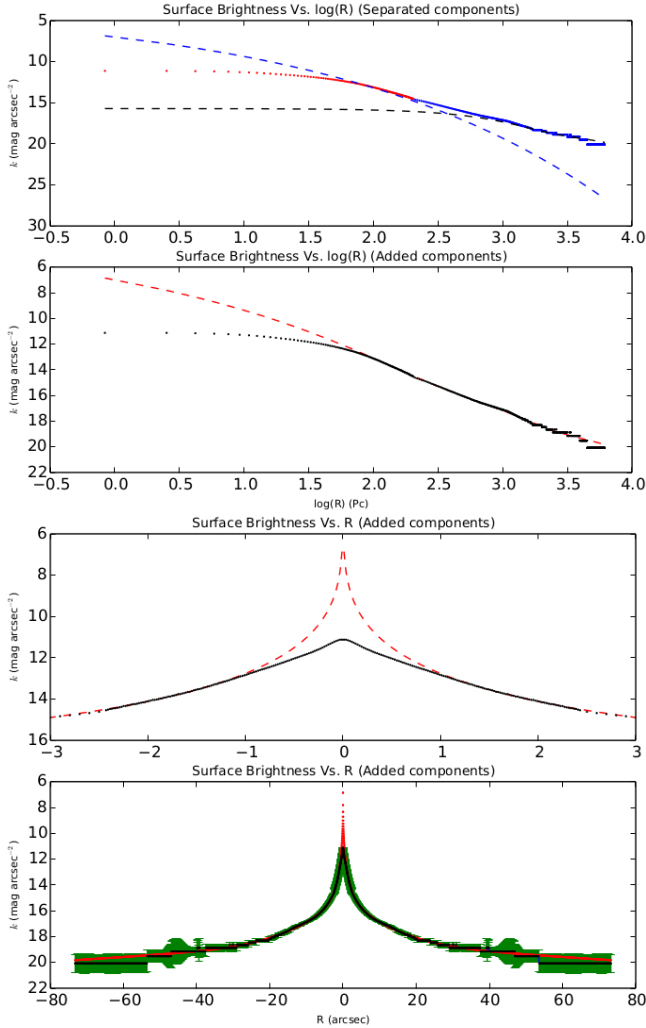


Figure 2.14: First figure: The K_S band surface brightness profile versus the logarithm of the radius ($\log(R)$) in units of pc. The blue dashed line shows the inwardly extrapolated Sérsic profile of the bulge component, while the black dashed line shows the dual exponential disk component. The red and blue points indicate the Subaru K_S and 2MASS K_S data, respectively. Second figure: Same as the first figure, but with the different components added. In this case the black points represent the joined Subaru/2MASS data set, while the red dashed line represents the combined fitted model. Third figure: The K_S band surface brightness profile versus radius (R) in units of arcsec for the innermost ~ 3 arcsec, while the red dashed line (again) indicates the combined fitted model. Fourth figure: Same as the third figure, but showing the complete data range up to ~ 70 arcsec. The green lines show the uncertainties of the data points.

Surprisingly, this result accounts entirely for the disagreement between the $M_{\text{BH}} - L$ and $M_{\text{BH}} - \sigma$ relations (see section 2.5.1).

Dong and De Robertis (2006) arrived at a similar result, using the bulge/disk decomposition algorithm GALFIT on the 2MASS data of NGC3718, in order to decompose the bulge from the disk and obtained magnitudes for both. Their best fit consists of two components, a Sérsic component with index $n = 5.5$ and $M_{K_S, \text{bulge}}^{\text{Dong}} \sim -22.75$ mag ($m_{K_S, \text{bulge}}^{\text{Dong}} \sim 8.45$ mag) for the bulge and a disk component with $R_S^{\text{disk}} \sim 60$ arcsec scale length. Their magnitude estimation is almost identical to the recovered magnitude from the fit presented here. Using this, equation 2.5 gives

$$M_{\text{BH}}^{M_{\text{BH}} - M_{K_S, \text{bulge}}^{\text{Sérsic}}} = 1.05_{-0.53}^{+1.05} \times 10^8 M_{\odot} .$$

Therefore, both fits reveal a very interesting morphological property of NGC3718. Instead of a Sérsic-like profile, a plateau is clearly visible near the center of the surface brightness profile. Although the fit describes the light distribution very well at radii $\geq 1 - 1.5$ arcsec, the model fails near the center where it suggests that a significant amount of light is missing. This can be seen in figure 2.14 as the difference between the observed and the fitted curves. **Kormendy et al. (2009)** suggest that surface brightness profiles with this characteristic is usually seen in core galaxies.

Briefly, an early-type galaxy is classified as a core galaxy when its inner surface brightness profile is shallower with respect to the inward extrapolation of the Sérsic fit of its outer profile, revealing a central light deficit. The opposite defines coreless galaxies. In these, the inward extrapolation of the outer profile's Sérsic fit is shallower with respect to the inner surface brightness profile, revealing a central light excess.

So, as the analysis suggests, the origin of the disagreement between the two scaling relations^{37,38} is, most likely, the observed light deficit. As several authors discuss (e.g. **Kormendy et al., 2009; Kormendy and Ho, 2013; Gualandris and Merritt, 2008**), light deficits³⁹

³⁷**Hopkins et al. (2008)** comments on the danger of performing three component fits. The fit indeed appears to be sensitive to the chosen lower and upper limits and this is the reason for setting statistical constraints based on the robustness of the data sample. The confirmation of the fit of **Dong and De Robertis (2006)** indicates, at least, a good level of consistency. Moreover, the fact that light is missing from NGC3718's central region is also evident in its published—mostly using larger apertures—photometry values on NED, which are closer to the Subaru aperture photometry measurement (see section 2.5.1) than to the recovered magnitudes. A slightly different Sérsic index combined with a small extra light component near the transition from the disk to the bulge (roughly at $\log(R) \sim 2 - 2.5$ pc in figure 2.14) cannot be conclusively ruled out, however, the presence of the disk would make such a component very difficult, if not impossible, to be distinguished in this case. If NGC3718 is an advanced merger remnant, then the limited star formation activity will have created some post merging stars that, in principal, could have formed an extra light component. Nevertheless, this is not expected to significantly alter the big picture, especially regarding the presence of the missing light, which seems largely dominant.

³⁸The sensitivity of the fit on the upper and lower limits is also noted by **Jog and Chitre (2002)** and they do not to perform such a fit. However, the Subaru data resolve the central ~ 2.5 arcsec of NGC3718 much better, providing more data points to work with.

³⁹Usually present in the brighter bulges and elliptical galaxies.

could be indicative of core depletion produced by the combined action of SMBH binaries followed by SMBH recoils (see sections 1.2.2 and 2.7.1). The amount of the light deficit, can be estimated by calculating the difference between the expected and the observed brightness (see figure 2.14, [Graham, 2004](#)). In the case of NGC3718, this is $M_{def}^{NGC3718} \sim 2.2 \times 10^9 M_{\odot}$, or $M_{def} \sim 19 M_{BH}$, and although it lies relatively away from the main distribution (i.e. $M_{def} \sim 5 M_{BH}$) on the $M_{def} - M_{BH}$ plot (i.e. figure 30) of [Kormendy and Ho \(2013\)](#), it is still closer to the main distribution than NGC4382, the only data point of an ongoing merger on this plot (i.e. $M_{def}^{NGC4382} \sim 50 M_{BH}$). Additionally, a core is realistic if the mass deficit is $\leq 1\%$ of the total galaxy mass (e.g. [Hopkins et al., 2008](#)) and for NGC3718 this is $M_{def}^{NGC3718} \sim 0.5\% M_{tot}^{NGC3718}$ (using $M_{tot}^{NGC3718} \sim 400 \times 10^9 M_{\odot}$ from [Schwarz \(1985\)](#)), which is within the realistic limits. These make the relatively large M_{def} of NGC3718 seem, at least, physically plausible.

Finally, the fit appears to be consistent with the results of previous studies. Study of 2MASS and kinematic data of NGC3718 by [Chitre and Jog \(2002\)](#) and [Jog and Chitre \(2002\)](#), revealed elliptical-like kinematics combined with spiral-like photometry. These “transitional” objects are thought to result from intermediate mergers with mass ratios $> (3 - 4.5) : 1$ (see section 1.2.2, [Bournaud et al., 2005](#)) and their remnants have many properties in common with lenticular galaxies. The fact that both the fit presented here and the fit of [Dong and De Robertis \(2006\)](#) recover the random motion supported bulge and the exponential disk in NGC3718’s surface brightness profile reflects that it is, likely, a lenticular galaxy and, consequently, can realistically be considered as a merger remnant.

The overall indications that NGC3718 is a merger remnant and the suggested mass deficit are compatible with the presence of an SMBH recoil. Further discussion on this subject is resumed in section 2.7. For now, the average SMBH mass of equations 2.5 (mine and [Dong and De Robertis \(2006\)](#)) and 2.6 is adopted for the rest of the calculations as a reasonable estimation for the M_{BH} , namely

$$M_{BH}^{NGC3718} = 1.11_{-0.55}^{+1.09} \times 10^8 M_{\odot} .$$

2.5.3 Core or coreless?

As it is evident so far, NGC3718 shares properties with both core and coreless elliptical galaxies. For example, the presence of missing light from the center of the galactic bulge is a characteristic usually found in core galaxies, whereas its central velocity dispersion is closer to that of a coreless galaxy. Therefore, further investigation for other similarities or differences with either of these categories is of special interest. Many authors (e.g. [Thomas et al., 2005](#); [Emsellem et al., 2007](#); [Cappellari et al., 2007](#)) have discussed the classification criteria of the so-called E-E dichotomy⁴⁰ and [Kormendy \(2009\)](#) presented the most updated and complete version.

⁴⁰Elliptical galaxies form two categories, each defined by a number of specific fundamental properties, such as core/coreless, boxy/disk, etc.

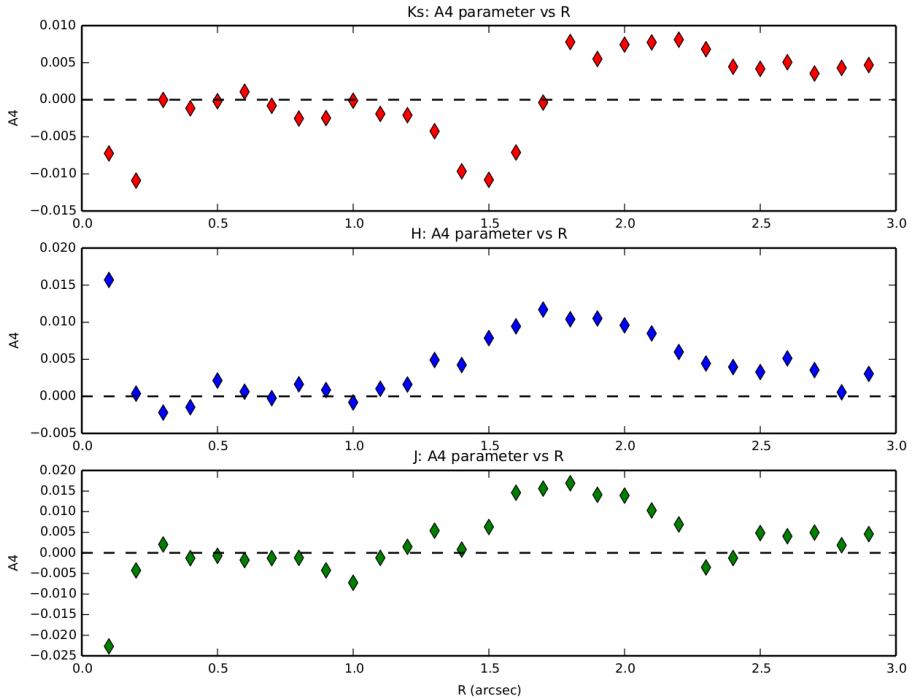


Figure 2.15: The A_4 parameter of NGC3718 plotted as a function of radius R (in units of arcsec), for the K_S (red/top), H (blue/middle), and J (green/bottom) bands. The dashed black line shows the transition from disk to boxy galaxies.

In favor of the classification of NGC3718 as a coreless galaxy is its visual magnitude $M_V^{NGC3718} = -20.73$ mag. This is fainter by nearly an order of magnitude than the border of the E-E dichotomy, namely $M_V \sim -21.5$ mag⁴¹, placing NGC3718 on the bright end of the coreless distribution (see figure 2 of [Kormendy, 2009](#)). Moreover, the presence of non-dominant radio emission (see figure 2.12, section 2.4.2, and [Krips et al. \(2007\)](#)) and NGC3718's stellar kinematic properties ([Jog and Chitre, 2002](#)) are also characteristics that are usually present in coreless galaxies.

On the contrary, the most obvious observational piece of evidence in favor of a classification of NGC3718 as a core galaxy is the—quite dominant—missing light observed in its surface brightness profile. Additionally, the high Sérsic index of $n > 4$ and the presence of X-ray emission (e.g. [Tueller et al., 2010](#)) may strengthen a potential classification of NGC3718 as a core galaxy.

Moreover, an interesting general trend in the shape of the isophotal contours in all

⁴¹The border of the E-E dichotomy was calculated for $H_0 = 72 \text{ km s}^{-1}$. For this H_0 , NGC3718's absolute magnitude becomes $M_V^{NGC3718} = -20.60$ mag.

Table 2.3: E-E dichotomy parameters.

Criteria	core	coreless	Reference
Visual Magnitude		✓	1
Surface Brightness profile	✓		5
Isophote Contours shape	✓	✓	4
Sérsic index	✓		5,6
Radio emission		✓	3,7,8,9
X-ray emission	✓		2,1
Kinematics		✓	10

Note. E-E dichotomy classification parameters for NGC3718.

References. (1) NED; (2) [Tueller et al. \(2010\)](#); (3) Figure 2.12; (4) Figure 2.15; (5) Figure 2.14; (6) [Dong and De Robertis \(2006\)](#); (7) [Pott et al. \(2004\)](#); (8) [Krips et al. \(2005\)](#); (9) [Krips et al. \(2007\)](#); (10) [Jog and Chitre \(2002\)](#);

images of figure 2.3 is observed, as shown in figure 2.15. The A4 parameter⁴² is mostly on the negative side out to a radius of $\sim 1 - 1.5$ arcsec, which is consistent with a boxy (i.e. core) galaxy. On larger radii, however, the A4 parameter rises steadily and remains on the positive side, out to a radius of ~ 3 arcsec, which is consistent with a disk (i.e. coreless) galaxy. This behavior could indicate an inside-out transformation of NGC3718– occurring roughly at the spatial scales of the observed light deficit– from a coreless to a core galaxy. The classification criteria of NGC3718 are summarized in table 2.3.

The picture formed from the above is that NGC3718 is, likely, an intermediate– between core and coreless– galaxy, complicating the interpretation of the results. It serves, however, as additional evidence that NGC3718 is the “smoking gun” of a past/ongoing merger, since the E-E dichotomy refers by definition to early-type galaxies, which are believed to form from the merging of late-type galaxies (see section 1.2.2).

2.6 Observational evidence for an SMBH recoil

The analysis of the observations suggests that NGC3718 is a merger remnant, with a dominant core in the central region of its surface brightness profile, and a spatial offset combined with a, potentially coincident and X-shaped, AGN offset. All of these findings are compatible with SMBH recoils.

For this view to be realistic, a few additional characteristic electromagnetic signatures should also be present in NGC3718 ([Komossa, 2012](#)). Perhaps the most prominent expected signature would be a relative velocity shift between a line’s broad and narrow components (e.g. $H\alpha$). Briefly, when a recoiled SMBH is present in a galaxy, it is likely to have a region larger than the BLR gravitationally bound to it, which, in turn, will result in a

⁴²The A4 Fourier coefficient is a measure of the degree of deviation of an isophote contour from an ellipse. Boxed galaxies have an $A4 < 0$, while disk galaxies have an $A4 > 0$.

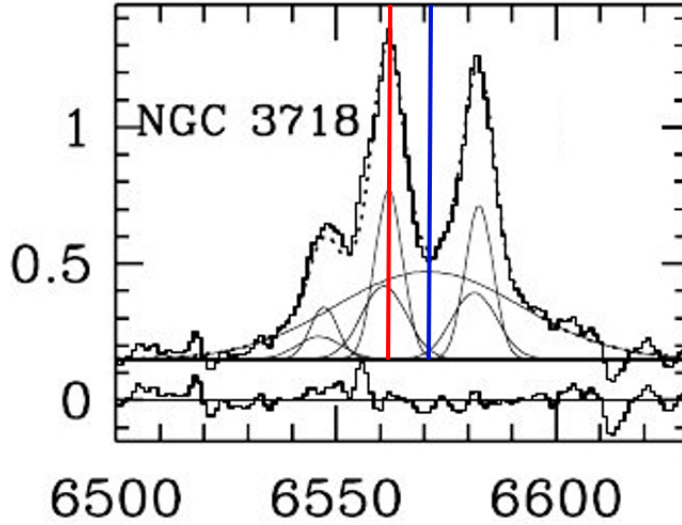


Figure 2.16: Reproduction of figure 10e from *Ho et al. (1997b)*, showing a part of the optical spectrum of NGC3718. The broad (indicated by the blue solid line) and the narrow (indicated by the red solid line) $H\alpha$ emission lines show a clear relative shift, indicating a motion of the BLR with respect to the NLR.

relative motion of the BLR with respect to the— much more extended— narrow line region (NLR). *Ho et al. (1997b)* fitted narrow and broad components to the $H\alpha$ line of the spectrum of NGC3718 and they found that their centroids are shifted relative to each other by 430 km s^{-1} (see figure 2.16). Accounting also for systematic offsets of $\sim 50\text{--}100 \text{ km s}^{-1}$ that are regularly observed between the broad and narrow line components in galaxy spectra (*Peterson, 1997*), a kick velocity of the order of

$$v_{kick} \sim 355 \text{ km s}^{-1} ,$$

is adopted as a realistic value. It has to be noted, however, that this velocity shift is the projected kick velocity, so it can only be considered as a lower limit of the actual kick velocity, a fact that should be accounted for in all subsequent calculations.

Based on the estimations for the v_{kick} and $M_{BH}^{NGC3718}$, I calculate the gravitationally bound— to the recoiled SMBH— radius, following the relation of *Merritt et al. (2006)*; *Komossa (2012)*

$$R_{bound} = \left(\frac{G \times M_{BH}}{v_{kick}^2} \right) \approx 0.4 \times \left(\frac{M_{BH}}{10^8 M_{\odot}} \right) \left(\frac{v_{kick}}{10^3 \text{ km s}^{-1}} \right)^{-2} \text{ pc} . \quad (2.9)$$

This results in an $R_{bound} \sim 3.53 \text{ pc}$ for NGC3718. Since the gravitationally bound radius

has an inversely proportional relation with the v_{kick} and due to the large uncertainties in the $M_{BH}^{NGC3718}$ estimation, this value should be considered as an indicative, but relatively uncertain estimation. With the uncertainties involved in mind, I can roughly estimate the size of the BLR, following the relation from [Zhang *et al.* \(2007\)](#)

$$R_{BLR} = q \times \left(\frac{G \times M_{BH}}{FWHM_{H\alpha, Broad}^2} \right), \quad (2.10)$$

which implies an $R_{BLR} \sim 0.06 - 0.12$ pc ($FWHM_{H\alpha, Broad} \approx 2350$ km s⁻¹ of NGC3718 from [Ho *et al.* \(1997a\)](#)), depending on the adopted value of q (i.e. $q = 0.75 - 1.33$). A last quantity to calculate is the sphere-of-influence of the recoiled SMBH, following the relation

$$R_{infl.} = \left(\frac{G \times M_{BH}}{\sigma^2} \right). \quad (2.11)$$

This is equal to $R_{infl.} \sim 19.1$ pc for the adopted values (i.e. $\sigma = 158.1 \pm 9.6$ km s⁻¹ from [Ho *et al.* \(2009\)](#)) and is ~ 5 times smaller than the core radius (i.e. ~ 100 pc).

The above estimations are very useful tools for a better understanding of the nuclear dynamics of NGC3718, since the suggested R_{BLR} and R_{bound} strongly imply that a BLR of this order of size would, likely, be entirely gravitationally bound to a recoiled SMBH with the observed characteristics.

For the final calculation, I use the symmetrical images of figure 2.7 in order to estimate quantities below the resolution limit. Considering this and that these images have not been thoroughly tested for their scientific validity (see section 2.3.3), this calculation is useful only as an order of magnitude estimation.

With these limitations in mind, a hyper compact stellar system (HCSS), with a luminosity of the order of the total luminosity of a globular cluster, is expected to be present within an R_{bound} around a recoiled SMBH ([Komossa, 2012](#)). This can be estimated by taking the difference– within an R_{bound} from the position of the offset red blob– of the K_S band fluxes of the images of figures 2.7 and 2.3. The main difference of these images is the presence of the offset red blob. The remaining emission should be a good first-order approximation of the contamination from the foreground and background– with respect to the nucleus– sources. The measured luminosity difference is

$$L_{HCSS} \sim 3.5 \times 10^4 L_{\odot},$$

and when this is converted to mass (see section 2.1), it yields

$$M_{HCSS} \sim 2.7 \times 10^4 M_{\odot},$$

both of which are within the luminosity and mass ranges of globular clusters.

The above measurements, therefore, further strengthen the possibility that NGC3718 is indeed the host of an SMBH recoil, since they appear to be compatible with key predictions of the current theory around SMBH recoils (e.g. Komossa, 2012; Sijacki *et al.*, 2011).

2.7 Discussion of chapter 2

Summarizing the results, observations of the central region of NGC3718 reveal the presence of a NIR spatial offset, potentially coincident with an (candidate) X-shaped offset AGN, as well as, a core in its surface brightness profile, while its— previously published— optical spectrum suggests the presence of a relative shift between its broad and narrow $H\alpha$ lines. These observational signatures support that there is an SMBH recoil present in the nucleus of NGC3718. Moreover, the fact that it has spiral-like photometry combined with elliptical-like kinematics and that some of its key properties belong to both core and coreless galaxies are indications that NGC3718 is, likely, a merger remnant. This fulfills the most important requirement for the very existence of an SMBH recoil, since the merging of galaxies is the only realistic theoretical mechanism that can lead to the formation of SMBH binaries and, subsequently, of SMBH recoils. Some of its properties, however, could also be thought to apparently contradict each other, giving rise to a very important question: Is there a complete framework that can incorporate all the observational characteristics of NGC3718 into one physically consistent scheme?

2.7.1 Galaxy evolution and the formation of cores

Attempting to answer this question requires a brief review of what is known so far about the two main subclasses of early-type galaxies. In the previous decades, it has become widely accepted that, in the framework of the Λ CDM cosmological model (e.g. White and Rees, 1978, see section 1.2.1), structures in the Cosmos grow hierarchically. Within this general picture, elliptical galaxies and classical bulges are thought to form in galaxy mergers, which results in the common properties seen in these objects. Additionally, a trend of increasing dissipation with decreasing mass is observed in elliptical galaxies (Kormendy, 2009). This reflects that later type, fainter ellipticals, being the “first stage” products of mergers between gas-rich spiral galaxies, have more gas available to dissipate through wet merging (Hopkins *et al.*, 2009a), while earlier type, giant ellipticals, being merger products of gas-poor fainter ellipticals, are formed in dry mergers (Hopkins *et al.*, 2009b, see section 1.2.2).

An immediate effect of wet mergers is that pre-existing stars in the progenitor (disk) galaxies violently relax at larger radii of the newly formed galaxy (giving rise to its Sérsic law profile), while the new stars form mainly in the intense central starburst as a result of gas dissipation. The violence of a major merger exerts tidal forces on the cold gas, which channel it towards the central region, triggering the feeding and feedback of the SMBH and

the intense nuclear starburst (Hopkins *et al.*, 2008). The AGN in this case operates in the so-called quasar mode. SMBH accretion will continue until $\sim 0.5\text{--}1\%$ of the energy output of the AGN is coupled to the infalling gas and blow it away, stopping the black hole growth and begin quenching the nuclear star formation (e.g. Ostriker and Ciotti, 2005). SMBH recoils will, likely, still occur, since mergers are a prerequisite of early-type galaxies formation, the presence of sufficient amounts of nuclear gas, however, will help the SMBH recoil damp its motion more quickly and return to the center (e.g. Blecha *et al.*, 2011; Sijacki *et al.*, 2011). This will stop the core depletion and will allow the intense central starburst to replace the missing light with newly formed stars (Kormendy and Ho, 2013), consuming the larger fraction of the available gas in the process (Hopkins *et al.*, 2008). The latter forms the extra light observed in these objects, which can be recognized as a break towards a steeper central surface brightness profile in comparison with the inward extrapolation of the outer Sérsic fit of the light profile (e.g. Hopkins *et al.*, 2009a,b; Kormendy and Ho, 2013).

On the other hand, dry mergers are the products of the subsequent merging of fainter, gas-poor, extra light ellipticals and as such, they lack the intense central starburst. The old violently relaxed stellar populations of the progenitor galaxies will violently relax at larger radii of the newly formed giant elliptical galaxy, while the extra light components will be preserved in the form of a higher stellar density in the central region (Hopkins *et al.*, 2009b). Tidal forces will channel the (little) remaining gas towards the central region, but the newly formed galaxy is massive enough to retain sufficient amounts of hot (X-ray emitting) gas, which will heat up any cold gas reaching the nucleus and, thus, prevent nuclear star formation (Nipoti and Binney, 2007). The AGN in this case operates in maintenance mode. This helps the gas to remain hot, further quenching the nuclear star formation and, eventually, keeping the merger dry (Kormendy and Ho, 2013). In such a gas-free environment, SMBH recoils can “stay on duty” for longer, acting mainly on the spatial scales of the preserved extra light fossil in the newly formed elliptical, excavating the core and creating what appears as missing light, or in other words, a break towards a shallower– compared to the inward extrapolation of its outer Sérsic fit– inner surface brightness profile.

2.7.2 Polar ring galaxies formation

Moreover, as it is extensively discussed in section 2.5.1, the observations support a polar ring galaxy classification for NGC3718, as suggested by Sparke *et al.* (2009). So, how are polar ring galaxies formed?

Two candidate formation mechanisms have been proposed (see figure 2.17). The first is the merging scenario (Bekki, 1997, 1998), which suggests a formation through a head-on collision between two orthogonally arranged galaxies, namely, the “intruder” and the “victim” (left panel of their figure 1). After the completion of the merger, the intruder will become the host galaxy (often a lenticular galaxy), while the victim will become the polar ring. The second scenario, supported by a number of different authors (e.g. Reshetnikov and Sotnikova, 1997), is the accretion scenario. This mechanism involves tidal gravita-

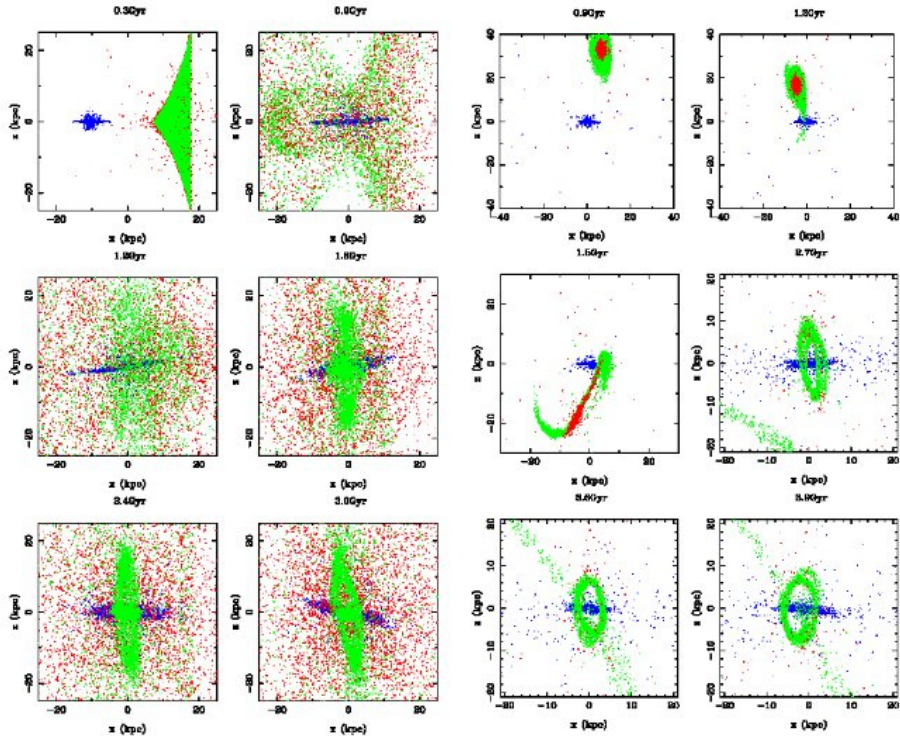


Figure 2.17: Six snapshots of the different evolutionary stages of the two polar ring galaxy formation scenarios adopted from [Bournaud and Combes \(2003\)](#). The merging scenario is shown in the six left hand panels, while the accretion scenario is shown in the six right hand panels.

tional interactions due to close encounters, explaining the formation of a polar ring galaxy through the accretion of gas on polar or nearly polar orbit from a “donor” galaxy to a host galaxy. Subsequent merging of the two progenitor galaxies is not required for the formation of a polar ring, but it is not physically prohibited.

Both formation mechanisms were simulated by [Bournaud and Combes \(2003\)](#), using the same numerical model. They found that both mechanisms can successfully reproduce a number of properties observed in polar ring galaxies, such as a) stable and nearly polar ring structures (at least up to 8 – 10 Gyr of evolution), b) early-type hosts, and c) warps/spiral-arm like features when polar ring galaxies are viewed from specific angles (i.e. edge-on/face-on for the ring/host galaxy). A number of independent studies (e.g. [Pott et al., 2004](#); [Krips et al., 2005](#); [Sparke et al., 2009](#)) suggest that these properties are present in NGC3718.

The two proposed scenarios, however, produce galaxies that are different in a number

of ways. At first, in the accretion scenario the host galaxy can be gas-rich, whereas in the merging scenario the host galaxy has to be gas-poor (which is the case of NGC3718 according to Sparke *et al.* (2009)). Secondly, in the merging scenario the stars of the victim galaxy form a faint, spherical, diffuse stellar halo, which surrounds both the host galaxy and the polar ring. NGC3718 appears to have such a faint diffuse stellar component, nearly engulfing the host galaxy and the edge-on ring (see figure 2.1). In the accretion scenario a donor galaxy is expected to be found in close proximity– if it has not already been “cannibalized” by the host– instead of a diffuse stellar halo, which in the case of NGC3718 could be the neighboring galaxy NGC3729. Lastly, the (inefficient) inflow of gas towards the center of the host galaxy is more consistent in the merging (i.e. $\sim 10 - 25\%$) than in the accretion scenario. Bournaud and Combes (2003) conclude that the most likely polar ring galaxy formation mechanism is the accretion scenario, at least for the majority of cases, however, they do not rule out the merging scenario based on physical, but rather on statistical argumentation, noting that it could realistically be invoked for the formation of some polar ring galaxies.

If the subsequent merging of the two galaxies after the accretion of gas into polar orbit is not a common output, then the present analysis favors the merging scenario as the most likely for the formation of NGC3718. The main reason is the plethora of observational evidence presented throughout this chapter for the presence of an SMBH recoil, whose existence requires a recent merger. Additionally, the low star formation activity noted by Sparke *et al.* (2009), as well as, the detection of gas within the central ~ 700 pc (Krips *et al.*, 2005) further strengthen the merging scenario, since the gas inflow it predicts appears to be confirmed by the observations. Finally, provided that the dust traces the kinematics of the gas (a reasonable assumption since gas and dust appear to be mixed in the polar ring), then the hot dust contribution to the K_S band emission (see section 2.4.1) could be viewed as a secondary tracer for the aforementioned gas inflow.

In principal, the accretion scenario can also account for these phenomena. However, if after the gas accretion the two galaxies merge, then the formation process could be described as a merger with a different orbital configuration. So, when I refer to a “merging event”, I mean either of the above polar ring galaxy formation mechanisms, provided that the merging of the central SMBHs is “guaranteed”, in order to be compatible with the indications for an SMBH recoil.

2.7.3 Building the big picture

However, the inefficient inflow of gas towards the central region predicted by the merging scenario could be the key for a robust physical explanation of the light deficit seen in the surface brightness profile of NGC3718 (see figure 2.14). Therefore, a working scheme could be the following:

Considering NGC3718 as a gas-rich⁴³ merger remnant, it is reasonable to expect signs of an intense central starburst in the form of an extra light component (e.g. [Kormendy and Ho, 2013](#); [Hopkins et al., 2008, 2009a](#)) instead of the observed core. However, the absence of sufficient amounts of nuclear gas leads naturally to the observed low star formation activity. Combining this with the fact that in gas-poor environments the time-scales for which SMBH recoils stay on duty are prolonged ([Sijacki et al., 2011](#)), create a physically consistent framework for the formation of a core. To put it more simply, although the gas exists in the galaxy, it is “locked up” in (the very stable) polar orbit ([Bournaud and Combes, 2003](#); [Bekki, 1997, 1998](#)), which, consequently, limits the available gas that can flow towards the center to trigger the necessary star formation and “fill the gap” created by the prolonged action of the recoiled SMBH.

Moreover, the radial behavior of the A4 parameter (see figure 2.15), which indicates an inside-out transformation of NGC3718 from a disky to a boxy galaxy, fits also within this framework. Boxiness is, generally, found in galaxies that lack the extra light component, either due to the limited amounts of nuclear cold gas and/or quenching of the nuclear star formation caused by AGN feedback ([Kormendy and Ho, 2013](#)). An environment with these characteristics appears to be ideal for an SMBH recoil to excavate a core and, in the case of NGC3718, it seems to be related with the isophotal contours shape, since the transition from boxy to disky contours happens roughly at the spatial scales of the core.

Furthermore, the presence of X-ray emission (see table 2.3) can potentially also be incorporated within this framework. Provided that it is, at least partly, associated with hot gas in the central region and combined with feedback from the AGN, can, in principal, point towards further quenching of the already low star formation activity caused by the limited gas inflow. The agreement between the gas and the stellar velocity dispersions ([Ho et al., 2009](#), $\sigma_{gas}\sigma_{\star}^{-1}$ is ~ 1 , see section 2.5.1), could be an observational indication that some of these processes are at work in the nucleus of NGC3718.

The last property of NGC3718 that needs to be incorporated into the above scheme is its AGN activity level. NGC3718 is a LINER galaxy ([Ho et al., 1997b](#)) and is one of the NUGA LLAGN sources ([García-Burillo et al., 2003](#)). Hosting an LLAGN, however, is compatible with an inefficient inflow of gas towards the nuclear region, since it would affect the accretion rate of the SMBH by reducing the available gas reservoir. The absence of sufficient amounts of nuclear gas is observationally supported by the fact that NGC3718 is a sub-Eddington system ($L_{bol}L_{edd}^{-1} \sim 10^{-4} - 10^{-5}$ [Krips et al. \(2007\)](#)), which indicates that the accretion onto the central engine is far from being efficient.

Any apparent contradictions that may arise, come from the fact that all these processes are not observed in a red and dead giant elliptical for which they were originally

⁴³It contains $M_{HI} \sim 8 \times 10^9 M_{\odot}$ ([Sparke et al., 2009](#)), approximately twice the HI content of the Milky Way, and $\sim 2.4 \times 10^8 M_{\odot}$ of molecular gas ([Krips et al., 2005](#)). These imply that NGC3718 is, on large-scales, a gas-rich galaxy.

proposed, but, circumstantially, due to the limited gas inflow– attributed to the dynamics of this (rare) merger case– in a gas-rich system.

2.7.4 An SMBH recoil?

The last question within the scope of this chapter is perhaps the most important, albeit a very difficult one to answer: Does an actual SMBH recoil exist in NGC3718? An attempt to give a qualitative answer to this question requires to further discuss the compatibility of NGC3718's observables with what is known about SMBH recoils.

The near-the-center position of the offset red blob allows for two different possibilities: It could be either the beginning of an SMBH displacement (i.e. an “early” SMBH recoil), or an ongoing (i.e. a “late”) SMBH recoil “captured” during one of its pericentric passages.

At first, if the age of $\sim 2 - 3$ Gyr of the gas disk of NGC3718 (Spärke *et al.*, 2009) roughly traces the age of the merger, then it would be in very good agreement with the predictions of the simulations of Bournaud and Combes (2003), where both a stable polar ring and a warp are produced from mergers with mass ratios of $\sim (1 - 4) : 1$ within $\sim 2 - 3$ Gyr. Blecha *et al.* (2011) performed simulations of recoils in galaxy mergers and they found that the SMBHs often coalesce at ~ 2 Gyr in relatively gas-poor major mergers (i.e. mass ratios $\sim (1 - 2) : 1$, gas content 10 – 30%). For similar systems and for recoil velocities of $v_{kick} \leq 0.7v_{esc}$, the SMBHs trajectories are confined within ~ 1 kpc with return timescales of the order of $\sim 0.5 - 1$ Gyr. Therefore, time-wise, it appears possible that either a recent, or an ongoing SMBH recoil could exist in NGC3718 and that it could be observed.

Secondly, if the current view around the formation of cores in galaxies is attributed mainly to a combinations of SMBH binaries and, subsequently, recoils (e.g. Kormendy and Ho, 2013), then the relatively large $M_{def} \sim 19 M_{BH}$ (see section 2.5.2) needs to be addressed. An M_{def} of this magnitude could partly reflect accumulated errors from uncertainties e.g. in the fit, in the assumed ML^{-1} relation, and/or in the large intrinsic scatter of the scaling relations. However, it could also imply that cores already present in the progenitor galaxies were inherited by NGC3718. Gualandris and Merritt (2008) studied the mass deficits that SMBH kicks can produce and they found that the combination of an SMBH binary (Merritt, 2006) and a subsequent recoil can remove $\sim 5 M_{BH}$ of stellar mass from the central region per merger. The fact that the light profile shapes are, more or less, preserved in dissipationless mergers (e.g. Hopkins *et al.*, 2009b) is what led several authors to conclude that large mass deficits could indicate different core depletion events after sequential mergers. It seems, therefore, possible that a large M_{def} can potentially co-exist with either a recent, or an ongoing SMBH recoil.

The shape of the radio emission of NGC3718, however, may provide a dividing line between a recent and an ongoing SMBH recoil. If NGC3718 is indeed an X-shaped radio source, then this would reflect that its SMBH has undergone a reorientation of its jet (Liu

et al., 2012) and that NGC3718 hosts a new SMBH recoil. In such a case, an inherited core of the observed size (i.e. ~ 200 pc across) is considered as necessary because a recently recoiled SMBH would not have the time to create it (Merritt, 2006). On the contrary, if the secondary extended radio features are not attributed to a second jet-fossil, then an ongoing SMBH recoil that accretes matter in one of its pericentric passages (Blecha *et al.*, 2011) could produce a – single– bipolar jet structure. In this case, the inheritance of a core of the observed size– or a part of it– is not necessary, although it is not prohibited either. Therefore, in principal, a core with the observed characteristics could have been excavated in “one go”, provided that the aforementioned uncertainties lead to a considerable overestimation of the M_{def} .

To conclude this chapter, I have presented a number of independent evidence, which, along with the findings from the analysis of the Subaru and e-Merlin data, suggest that NGC3718 could be considered as a very good candidate for hosting an SMBH recoil. Therefore, an interesting question arises: Are SMBH recoils a standard process in galaxy evolution? If NGC3718 is a polar ring galaxy and polar ring galaxies account for $\sim 5\%$ of the lenticular and early-type galaxies in the local Universe (Whitmore *et al.*, 1990), then the suggested detection of an SMBH recoil in such a rare object could be a hint for an affirmative answer. However, our limited knowledge around the exact behavior of SMBH recoils and the precise mechanism(s) that form the cores, combined with the limited resolution of the present observations allow only for general qualitative and, consequently, highly speculative interpretations. Certainly though, higher resolution future observations and simulations are necessary for more detailed and quantitative answers to the above questions. In all, NGC3718 turns out to be an object where very interesting phenomena are taking place, with, possibly, many more yet to be revealed.

Cen A: Supergiants in a region of jet-induced star formation?

3.1 Introduction to chapter 3

Located at a distance of ~ 3.8 Mpc (Rejkuba, 2004), NGC5128 is the host galaxy of the famous, powerful radio source Cen A. This peculiar giant elliptical galaxy is, generally, seen as an example of a post-merging system, thought to be the result of a recent merger between a small gas-rich and a massive early-type galaxy (e.g. Malin *et al.*, 1983; Israel, 1998).

The NML of Cen A is located in the NE part of NGC5128. A CO molecular cloud (Charmandaris *et al.*, 2000), an HI cloud (Schiminovich *et al.*, 1994; Oosterloo and Morganti, 2005), filaments of ionized gas, young blue stars arranged in OB associations (e.g. Blanco *et al.*, 1975; Graham and Price, 1981; Graham, 1998; Fassett and Graham, 2000; Mould *et al.*, 2000; Rejkuba *et al.*, 2001), and shells of old stars (Malin *et al.*, 1983) have been previously observed near this region. A number of authors (e.g. Graham, 1998; Fassett and Graham, 2000; Mould *et al.*, 2000; Rejkuba *et al.*, 2001) have argued that the OB associations of this region have resulted from a recent jet-induced star formation, since both the filaments of ionized gas and the gas clouds seem to be associated with the young blue stars that are located near the NE border of the HI cloud and directly into the jet's path (see figure 3.1). All these lie superimposed on a— typical for the halo of NGC5128— background sheet of older stars (Mould *et al.*, 2000; Rejkuba *et al.*, 2001).

These young blue stars are estimated to be $\sim 10 - 15$ Myr old (Mould *et al.*, 2000; Fassett and Graham, 2000; Rejkuba *et al.*, 2001). Within this time-frame, the most massive of these stars will have naturally evolve past the main-sequence. In this context, the NE part

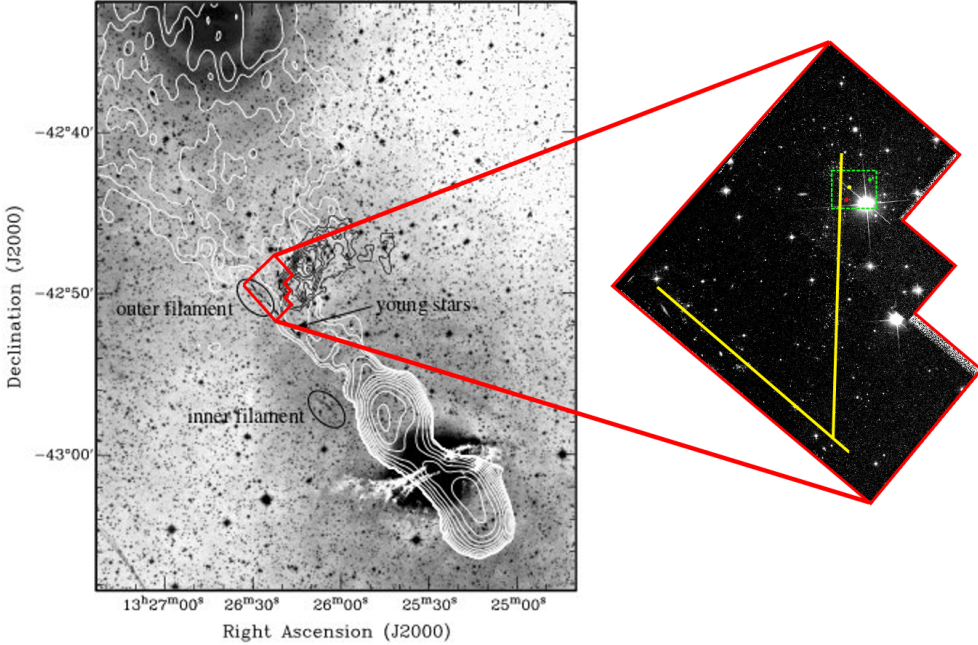


Figure 3.1: *Left: Reproduction of figure 1 from Oosterloo and Morganti (2005). Over-plotted on an optical image of NGC5128 can be seen a) the HI cloud (black contours), b) the centimeter radio jet (white contours), c) and the filaments of ionized gas (black ellipses). The approximate position of the HST field (Mould et al., 2000) is shown by the red outlined region. Right: The green dashed rectangle represents the Subaru field, while the yellow lines on the HST F555W image approximately indicate the positions of the OB associations.*

of Cen A is an ideal target for identifying bright, extra-galactic, NIR-excess sources like supergiants (i.e. YSGs and red (RSGs)) and/or asymptotic giant branch (AGB) stars that should already exist if a recent star formation has taken place. Attempting, therefore, to resolve denser-than-average stellar fields in galaxies outside our Local Group (LG), using the top-of-the-range 8-meter class telescopes assisted by AO systems, could have a great potential in understanding the nature of the stellar populations of numerous, relatively, nearby galaxies.

Chapter 3 is organized as follows. In section 3.2 I describe the data and data reduction; in section 3.3 I describe the process of locating the Subaru FoV on the HST images of this region; in section 3.4 I describe the NIR data processing and I attempt, using statistical and photometric techniques, to constrain the luminosity classes and the spectral types of the three brighter stars on the HST images; and in section 3.5 I discuss the results and the observational potential to resolve dense stellar populations (e.g. OB associations) into individual stars in galaxies beyond our LG with ground-based observations.

3.2 Observations and data used in chapter 3

3.2.1 Subaru data of Cen A

The available data set for the study of the OB associations along the Cen A jet consists of NIR– $J(10)$, $H(10)$, and $K_S(10)$ bands (number of images)– AO assisted data taken with the HiCIAO (Suzuki *et al.*, 2010) instrument in DIM, on the 17th of May 2012, aboard the Subaru telescope at Mauna Kea, Hawaii. The detector used is a Hawaii-IIRG HgCdTe with 2048×2048 pixels², providing an FoV of 20×20 arcsec², which results in a pixel scale of 0.010 arcsec pixel⁻¹. The exposure time for the individual frames in all bands is $t_{exp}^{J,H,K_S} = 60$ sec. The AO system used is the AO188 (Hayano *et al.*, 2010). The system is installed at the IR Nasmyth platform of the Subaru telescope and it is equipped with a 188-element wavefront curvature sensor with photon counting APD modules and a 188 element bimorph mirror. The resulting angular resolution of the data-set is ~ 270 (J), ~ 210 (H), and ~ 170 (K_S) mas for the three NIR bands, respectively. This particular field was chosen out of the entire region occupied by the OB associations because it contains sufficiently bright AO natural guide stars, which are necessary in order to achieve the highest possible angular resolution.

The pipeline constructed for the reduction of the NGC3718 data (see section 2.2.1) was used for the reduction of the Cen A data as well. This includes correction for the 32-strip artifact noise– introduced by the 32 readout channels of the detector–, correction for bad pixels, flat-fielding (dome-flat), sky-subtraction, alignment and median stack for all the, initially dithered, raw images (see appendix A). Finally, any large-scale patterns were removed from the final NIR images by subtracting the weighted average of the mean column and row values. In all images north is up and east is left. In figure 3.2 I present the final, $\sim 20 \times 18$ arcsec² J , H , and K_S images.

3.2.1.1 Subaru photometric calibration

The calibration of the flux of the Subaru images is performed according to section 2.3.4. Standard star observations are used to derive appropriate ZPs for the three NIR bands, which are subsequently used in all apparent magnitude calculations through:

$$m_{Sub.}^i = Z.P.^i_{Sub.} - 2.5 \log\left(\frac{\text{Counts}_{Sub.}^i}{\text{Exp.Time}_{Sub.}^i}\right). \quad (3.1)$$

3.2.2 HST data of Cen A

Archived⁴⁴ HST $F555W$ and $F814W$ imaging data of the same region of Cen A (originally studied by Mould *et al.*, 2000, see figure 3.3) are also used. The $F555W$ and $F814W$

⁴⁴<http://hla.stsci.edu/hlaview.html#>

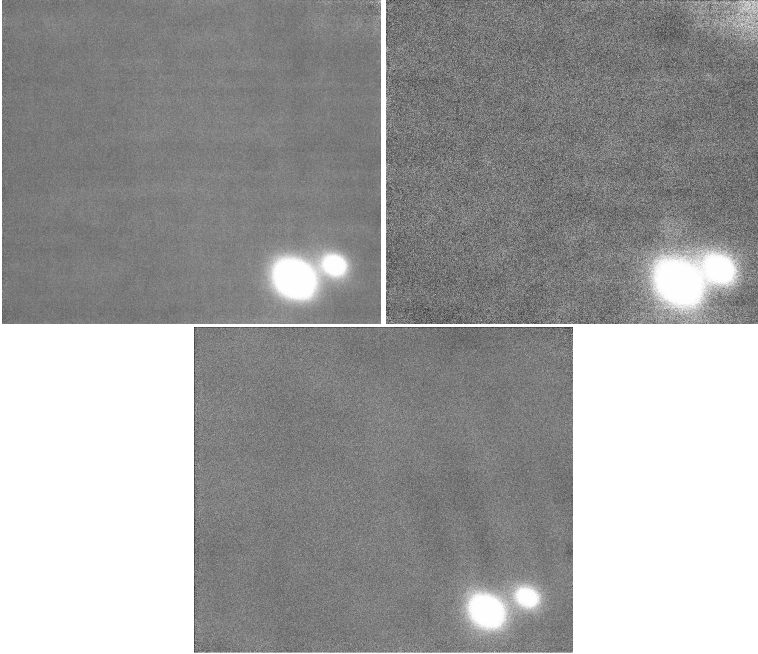


Figure 3.2: The final, $\sim 20 \times 18 \text{ arcsec}^2$ Subaru J (top left), H (top right), and K_S (bottom middle) images.

apparent magnitudes are obtained with aperture photometry, while transformations from the STMAG to the UBVRI photometric system are performed according to the values given in the HST Data Handbook for WFPC2/WFPC2 Photometry Cookbook. Throughout this chapter the average transformations $V - F555W \sim -0.01 \pm 0.06 \text{ mag}$ and $I - F814W \sim -1.30 \pm 0.24 \text{ mag}$ are adopted. The validity of these transformations is tested against the $V - I$ color indices and V band magnitudes of the two brightest stars on the WF2 chip (see table 1 from Mould *et al.*, 2000). The resulting photometry of these sources is within $\sim 5\%$ from the values given by Mould *et al.* (2000), which indicates that the adopted transformations are acceptably accurate.

3.3 Locating the FoV

The central coordinates of the Subaru FoV are $\alpha_{2000} = 13:26:21.127$ and $\delta_{2000} = -42:49:09.02$, located approximately $\sim 15 \text{ kpc}$ from the center of NGC5128 towards the NE. I use the two AO guide stars⁴⁵ and the cardinal points as reference, in order to locate the FoV of the Subaru images on the HST images (see figure 3.3). The position angles (PA) of the two

⁴⁵The term “guide stars” refers always to the foreground AO guide stars in the lower right corner of the HST (see figure 3.3) and/or the Subaru images (see figure 3.2). With the term “unresolved guide star” I also refer to the same sources, in this case, however, the quoted information (e.g. proper motion, magnitude etc.) is obtained from lower resolution images in which these stars are unresolved (e.g. 2MASS, UCAC4 etc.).

guide stars are $\sim 19.3 \pm 1.0$ and $\sim 19.0 \pm 0.1$ degrees, while their projected separations are $\sim 2.19 \pm 0.14$ and $\sim 2.25 \pm 0.01$ arcsec on the HST and the Subaru images⁴⁶, respectively. These indicate that this “binary” guide star can be either a long-period physical, or an apparent projected rather than a close physical binary. The insignificant change in their PA and projected separation between the epochs of the Subaru and the HST data (i.e. ~ 15 years) could be either due to the combination of the different– but negligible– proper motions of the two projected members, or due to the “capture” of a close physical binary in an orbital configuration similar to that on the HST images. In a, time-wise, random observation though, the former appears more likely to be the case.

Additionally, the total proper motion of the unresolved guide star (G.S.) quoted in the UCAC4 catalog (Zacharias *et al.*, 2013), namely, $\sim 24.2 \pm 14.3$ mas and $\sim -34.5 \pm 12.0$ mas in RA and Dec, respectively, is negligible. In principal, this can account for the small observed change in PA and projected separation (i.e. ~ 0.3 degrees and ~ 60 mas, respectively), which is in any case within the uncertainties. Most importantly, however, the negligible proper motion of the G.S. is a good indication that the HST field stars⁴⁷ are expected roughly at the same, with respect to the two guide stars, positions on the Subaru NIR images as well.

3.3.1 Testing the Subaru photometric calibration

Since the Subaru AO guide stars are not saturated on the NIR images, aperture photometry is possible. This yields $m_{G.S.1}^{K_S} = 11.39 \pm 0.10$ mag, $m_{G.S.1}^H = 11.53 \pm 0.10$ mag, and $m_{G.S.1}^J = 11.70 \pm 0.10$ mag for the SE guide star (G.S.1) and $m_{G.S.2}^{K_S} = 13.01 \pm 0.10$ mag, $m_{G.S.2}^H = 13.25 \pm 0.10$ mag, and $m_{G.S.2}^J = 13.83 \pm 0.10$ mag for the NW guide star (G.S.2).

In order to test the accuracy of the photometric calibration against literature photometry, I calculate the Subaru NIR magnitudes of the “G.S.” by adding the fluxes of G.S.1 and G.S.2. These are $m_{SUB. G.S.}^{K_S} = 11.17 \pm 0.14$ mag, $m_{SUB. G.S.}^H = 11.33 \pm 0.14$ mag, and $m_{SUB. G.S.}^J = 11.56 \pm 0.14$ mag, in excellent agreement with the magnitudes of the G.S. from the 2MASS survey, namely, $m_{2MASS G.S.}^{K_S} = 11.15 \pm 0.02$ mag, $m_{2MASS G.S.}^H = 11.30 \pm 0.04$ mag, and $m_{2MASS G.S.}^J = 11.51 \pm 0.03$ mag. This indicates that the Subaru flux calibration is very accurate, which allows the use of the two AO guide stars as calibration reference sources for the rest of the calculations in this chapter.

⁴⁶The centers of both guide stars on the Subaru images and of the fainter NW guide star on the HST images are estimated by fitting Gaussian functions on their profiles. For the brighter (and saturated, SE) guide star on the HST images, however, I use the central pixel of the saturated area of the PSF, both in RA and Dec, as an acceptable– though significantly more uncertain– center estimation.

⁴⁷With the term “field stars” I always refer to the faint background stars on the HST images (see figure 3.1 and 3.3). These are thought to belong to the OB associations along the Cen A jet.

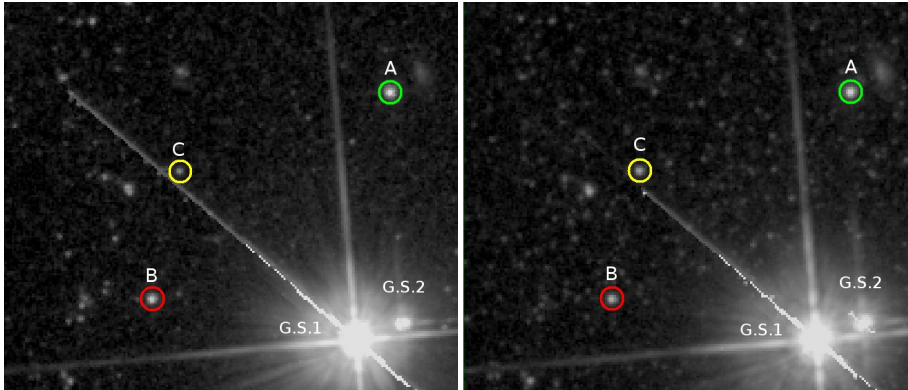


Figure 3.3: HST F555W (left) and F814W (right) images. This HST FoV is equivalent to the FoV of the Subaru J, H, and K_S band images ($\sim 20 \times 18 \text{ arcsec}^2$). The three colored circles indicate the positions of the brighter stars on the HST F814W field. The A HST star (green circle) is the brightest, the B HST star (red circle) is the second brightest, and the C HST star (yellow circle) is the third brightest.

3.4 Data processing

Initially, there isn't any visible point source-like signal on the Subaru images (see figure 3.2) that can be correlated with any of the field stars on the HST images (see figure 3.3). In order, therefore, to highlight any signal that could be “hidden” into the noise, I apply a low-pass filter⁴⁸ with a 10 pixel Gaussian kernel on all NIR images. From the low-pass filtered images, a JHK_S composite image— using equal weight for each NIR band— is subsequently constructed, in order to increase the SNR further by $\sim \sqrt{3}$ (see figure 3.4).

This process reveals strong signal at the brightest HST field star's expected position (A HST star – see figure 3.3) on all the low-pass filtered NIR images of figure 3.4. This signal has a $> 3\sigma$ above the background peak flux, while this is the only position where such a strong signal is consistently observed on all NIR bands (see figure 3.5). Considering also that the field stars are expected approximately at the same positions on the HST and the Subaru images, raises a very interesting question: Does the $> 3\sigma$ signal originate from the NIR counterparts of the A HST star and, if so, is it possible to further constrain its nature? Attempting to give an answer to this question requires both a statistical and a photometric approach.

3.4.1 Statistical analysis of the NIR $> 3\sigma$ signal

Statistically approaching this problem means that the above question should be expressed in a more mathematically appropriate way: What is the probability of a $> 3\sigma$ signal obser-

⁴⁸Low-pass filtering, or smoothing, an image will attenuate the highest frequencies of the noise, resulting in a higher SNR.

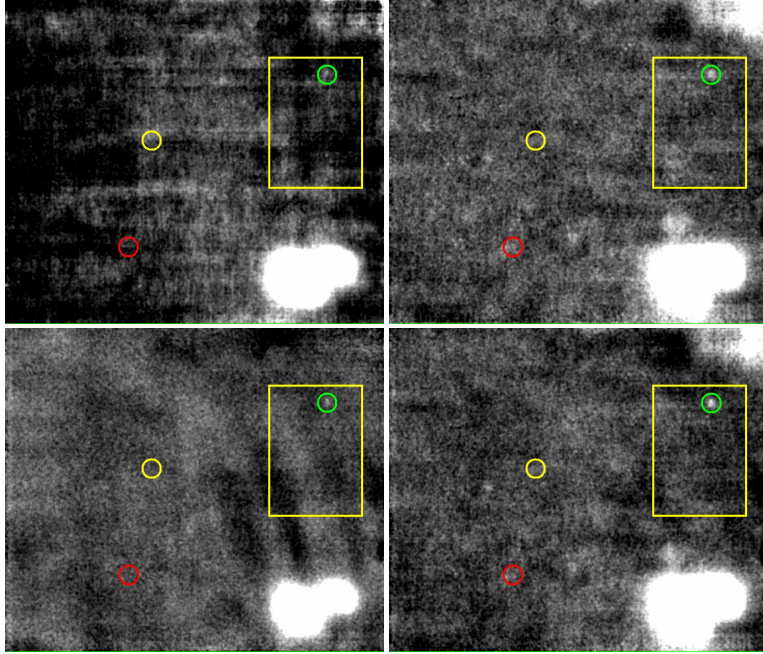


Figure 3.4: Low-pass filtered with a 10 pixel Gaussian kernel Subaru J (top left), H (top right), K_S (bottom left), and the JHK $_S$ composite (bottom right) images. The expected positions of the three brighter stars on the HST F814W field are marked by the three colored circles. The statistics region is outlined by the $\sim 5 \times 7$ arcsec 2 yellow box.

vation, at a given position, in three independent experiments, if this signal originates from stochastic fluctuations of the background noise alone?

In general, the background noise⁴⁹ of an astronomical image is distributed according to the Poisson distribution, which should gradually approach the Gaussian distribution as the statistical sample becomes larger. Given a Gaussian distribution, the probability of randomly observing (i.e. drawing) a flux value F_i which satisfies the condition

$$F_{bg}^- - 3\sigma \geq F_i \text{ and } F_i \geq F_{bg}^- + 3\sigma ,$$

where F_{bg}^- is the mean flux of the background noise (i.e. the underlying distribution), from a single observation (i.e. a single experiment) is $\leq 0.27\%$.

The statistical analysis is performed in a sub-region of $\sim 5 \times 7$ arcsec 2 (see figures 3.4 and 3.5), with the position of the A HST star included. Given the large statistical sample (i.e. $N \sim 3.5 \times 10^3$ pixels), the background noise is expected to be distributed approximately

⁴⁹Often called “white noise” or “shot noise”.

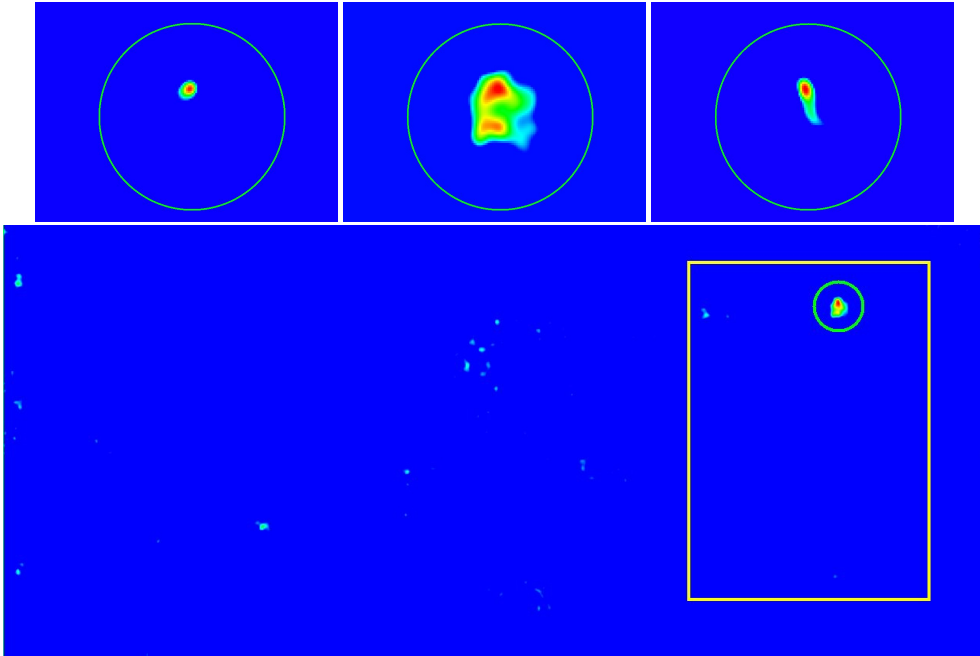


Figure 3.5: Top: The $> 3\sigma$ signal at the (zoomed-in) expected position of the A HST star on the three Subaru NIR bands, namely, J (left), H (middle), and K_S (right). Bottom: A $\sim 20 \times 9$ arcsec² region of the JHK_S composite image, in which the statistics region is outlined by the $\sim 5 \times 7$ arcsec² yellow box. All images are clipped at 3σ above the background (blue background).

normally, which appears to be the case, since the median and the mean converge within the chosen sampling area. In turn, this implies a) that the distribution is not heavy tailed, but most importantly, b) that this statistical sample provides a good representation of the global statistics, at least, in terms of statistical power.

The probability, therefore, of a $\geq 3\sigma$ above the background observation, when a pixel inside the chosen sampling area is randomly selected from a single observation is $\leq 0.135\%$ or $P(A) \leq 0.00135$ ⁵⁰. Taking also into account that the $> 3\sigma$ signal at the A HST star's position is the only signal that is consistently present on all NIR bands (i.e. three independent experiments), the probability that it originates from random background noise fluctuations alone should be $[P(A)]^3 \leq 2.5 \times 10^{-9}$ or $\leq 2.5 \times 10^{-7}\%$. Considering this as being negligible, the origin of the NIR $> 3\sigma$ signal of figure 3.5 should, realistically, be assigned to the presence of a point source, which systematically produces flux values above the $+3\sigma$ limit within the green circle in repeated observations.

⁵⁰The probability of observing values outside the $F_{pg}^{\pm} \pm 3\sigma$ limits is $P(A) \leq 0.0027$. Consequently, half of this should represent the probability of observing values that exceed only the $+3\sigma$ limit. A $P(A) \leq 0.00135$ is, therefore, adopted as a logical occurrence probability of a random $\geq 3\sigma$ observation in a single experiment.

However, are the NIR photometric properties of these $> 3\sigma$ detections consistent with the photometric properties of the A HST star?

3.4.2 Photometric calibration of the NIR $> 3\sigma$ detections

The V and I magnitudes of the A HST star are measured with aperture photometry on the HST $F555W$ and $F814W$ images (see section 3.2.2), namely, $m_{HST,A}^V = 20.23 \pm 0.12$ and $m_{HST,A}^I = 19.39 \pm 0.26$ mag, respectively.

Conversely, using aperture photometry for measuring the magnitudes of the NIR $> 3\sigma$ detections is not possible in this case, since their stellar profiles are not fully recovered. Alternatively, their J , H , and K_S magnitudes can be estimated by taking the ratio of the added NIR peak fluxes of the two guide stars (i.e. G.S.1 and G.S.2) to the peak fluxes of the NIR $> 3\sigma$ detections⁵¹, using

$$m_{>3\sigma}^{J,H,K_S} = m_{G.S.}^{J,H,K_S} + 2.5 \times \log X \quad (3.2)$$

$$\text{with, } X = \left(\frac{F_{G.S.1}^{J,H,K_S} + F_{G.S.2}^{J,H,K_S}}{F_{>3\sigma}^{J,H,K_S}} \right),$$

where, $m_{G.S.}^{J,H,K_S}$ represents the Subaru G.S. magnitudes derived in section 3.3.1, $F_{G.S.1}^{J,H,K_S}$ and $F_{G.S.2}^{J,H,K_S}$ represent the NIR peak fluxes of G.S.1 and G.S.2, respectively, and $F_{>3\sigma}^{J,H,K_S}$ represents the NIR peak fluxes of the $> 3\sigma$ detections.

The resulting J , H , and K_S magnitudes of the $> 3\sigma$ detections are $m_{>3\sigma}^{K_S} = 18.15 \pm 0.37$ mag, $m_{>3\sigma}^H = 18.51 \pm 0.36$, and $m_{>3\sigma}^J = 18.96 \pm 0.36$, respectively, while their uncertainties are calculated as follows:

$$\delta m_{>3\sigma}^{J,H,K_S} = \left((\delta m_{G.S.}^{J,H,K_S})^2 + 0.43^2 \times 2.5^2 \times \left(\frac{\delta X}{X} \right)^2 \right)^{1/2} \quad (3.3)$$

$$\text{with, } \left(\frac{\delta X}{X} \right)^2 = \frac{(\delta F_{G.S.1}^{J,H,K_S})^2 + (\delta F_{G.S.2}^{J,H,K_S})^2}{(F_{G.S.1}^{J,H,K_S} + F_{G.S.2}^{J,H,K_S})^2} + \left(\frac{\delta F_{>3\sigma}^{J,H,K_S}}{F_{>3\sigma}^{J,H,K_S}} \right)^2$$

$$\text{and } (\delta m_{G.S.}^{J,H,K_S})^2 = (\delta m_{G.S.1}^{J,H,K_S})^2 + (\delta m_{G.S.2}^{J,H,K_S})^2,$$

where a 10% uncertainty for the measurements of $F_{G.S.1}^{J,H,K_S} / F_{G.S.2}^{J,H,K_S}$ and a 30% uncertainty for the measurements of the $F_{>3\sigma}^{J,H,K_S}$ is assumed.

⁵¹Different point sources simultaneously observed with the same telescope will be convolved with the same PSF, provided that their projected separations are smaller than ~ 30 arcsec (i.e. the isoplanatic angle). As a consequence, the ratio of their fluxes at any given point across their PSFs, as well as, the ratio of their total fluxes will be approximately equal, making any of these measurements representative of their actual magnitude difference.

Having the visual and NIR magnitude estimations of the $\text{NIR} > 3\sigma$ detections/A HST star, I can estimate its $V - I$, visual-NIR⁵², and NIR⁵³ color indices and attempt to put a constraint on its spectral type and luminosity class.

3.4.3 An extra-galactic supergiant or a galactic dwarf?

Two scenarios are possible for the nature of the A HST star. This star can be either an extra-galactic supergiant, member of the jet-induced stellar populations of Cen A, or a main-sequence dwarf in our Milky Way galaxy. The V and I magnitudes of the A HST star imply a $V - I = 0.84 \pm 0.28$ color index, which, based on the (intrinsic) colors of supergiants and main-sequence stars from [Ducati et al. \(2001\)](#) (see table 3.1), is consistent with either an $F8$ to $G3$ supergiant, or an $F5$ to $K1$ main-sequence dwarf.

Since the $V - I$ color index is measured directly with aperture photometry on the HST images, in which the A HST star has a proper Gaussian PSF—and, therefore, its photometry has a smaller uncertainty—, it serves as the primary criterion in assigning a spectral type to the A HST star. The visual-NIR color indices are then used as a secondary criterion, in order to check for inconsistencies on if and how they overlap with the $V - I$. For completeness, I also examine the overlap of the NIR with the $V - I$ and Visual-NIR color indices for each luminosity class. The results are shown in table 3.1.

On the one hand, the spectral type ranges (STR) suggested by the $V - I$ and visual-NIR color indices of the A HST star are rather limited and they show acceptable agreement for both luminosity classes, but in the case of supergiants the overlap of the color indices is nearly perfect. In contrast, the NIR color indices suggest significantly larger STRs for both luminosity classes, so they cannot be individually used in a physically meaningful way, despite the fact that they overlap with both the $V - I$ and visual-NIR color indices.

It should be noted at this point that I do not correct for reddening because its exact value along the lines-of-sight towards the OB associations of Cen A cannot be precisely known. However, according to the IRSA dust extinction online tool⁵⁴ the reddening on large-scales (i.e. several arcmin) towards NGC5128 should not be significant. Applying the quoted extinction values on the color indices of the A HST star would reduce them by ~ 0.12 mag ($V - I$), $\sim 0.20 - 0.24$ mag (visual-NIR), and $\sim 0.02 - 0.04$ mag (NIR). As a result, these corrections would cause a shift of the spectral type classifications towards ~ 1 type earlier in table 3.1, which can not, qualitatively at least, affect the interpretation of the results.

Is there a way, however, to further distinguish between the supergiant and the dwarf scenarios?

⁵²I.e. $V - J$, $V - H$, and $V - K_S$.

⁵³I.e. $J - H$, $H - K_S$, and $J - K_S$.

⁵⁴<http://irsa.ipac.caltech.edu/applications/DUST/>

Table 3.1: NIR and Visual-NIR colors.

Colors	$V-I$	$V-J$	$V-H$	$V-K_S$	$J-H^a$	$H-K_S^a$	$J-K_S^a$
A HST Star	0.84	1.27	1.72	2.08	0.45	0.36	0.81
Uncertainties	(± 0.28)	(± 0.38)	(± 0.38)	(± 0.39)	(± 0.51)	(± 0.52)	(± 0.52)
Spectral Type	Intrinsic colors of Supergiants (Ducati et al., 2001)						
A5	0.180	0.200	0.290	0.350	0.090	0.060	0.150
F0	0.310	0.360	0.510	0.600	0.150	0.090	0.240
F2	0.370	0.440	0.620	0.730	0.180	0.110	0.290
F5	0.470	0.570	0.790	0.910	0.220	0.120	0.340
F8	0.700	0.870	1.170	1.340	0.300	0.170	0.470
G0	0.900	1.140	1.520	1.710	0.380	0.190	0.570
G2	1.060	1.350	1.800	1.990	0.450	0.190	0.640
G3	1.120	1.430	1.900	2.090	0.470	0.190	0.660
G3.5	1.160	1.470	1.950	2.150	0.480	0.200	0.680
G4	1.190	1.520	2.010	2.200	0.490	0.190	0.680
G5	1.260	1.610	2.130	2.320	0.520	0.190	0.710
G8	1.430	1.830	2.410	2.590	0.580	0.180	0.760
K0	1.590	2.010	2.640	2.800	0.630	0.160	0.790
K1	1.680	2.110	2.760	2.910	0.650	0.150	0.800
K2	1.760	2.200	2.870	3.010	0.670	0.140	0.810
K3	1.960	2.410	3.140	3.250	0.730	0.110	0.840
K3.5	2.040	2.500	3.250	3.340	0.750	0.090	0.840
K4	2.130	2.590	3.370	3.440	0.780	0.070	0.850
K5	2.270	2.740	3.550	3.590	0.810	0.040	0.850
Spectral Type	Intrinsic colors of Main-sequence Stars (Ducati et al., 2001)						
A9	0.310	0.310	0.490	0.440	0.180	-0.050	0.130
F0	0.360	0.370	0.570	0.520	0.200	-0.050	0.150
F1	0.400	0.430	0.640	0.580	0.210	-0.060	0.150
F2	0.450	0.480	0.710	0.660	0.230	-0.050	0.180
F5	0.570	0.670	0.930	0.890	0.260	-0.040	0.220
F8	0.640	0.790	1.060	1.030	0.270	-0.030	0.240
G0	0.700	0.870	1.150	1.140	0.280	-0.010	0.270
G2	0.750	0.970	1.250	1.260	0.280	0.010	0.290
G3	0.760	0.980	1.270	1.280	0.290	0.010	0.300
G5	0.780	1.020	1.310	1.320	0.290	0.010	0.300
G8	0.850	1.140	1.440	1.470	0.300	0.030	0.330
K0	0.970	1.340	1.670	1.740	0.330	0.070	0.400
K1	1.050	1.460	1.800	1.890	0.340	0.090	0.430
K2	1.140	1.600	1.940	2.060	0.340	0.120	0.460
K3	1.250	1.730	2.090	2.230	0.360	0.140	0.500
K4	1.340	1.840	2.220	2.380	0.380	0.160	0.540
K5	1.540	2.040	2.460	2.660	0.420	0.200	0.620
K7	1.860	2.300	2.780	3.010	0.480	0.230	0.710
M0	2.150	2.490	3.040	3.290	0.550	0.250	0.800
M1	2.360	2.610	3.220	3.470	0.610	0.250	0.860
M2	2.620	2.740	3.420	3.670	0.680	0.250	0.930
M3	2.840	2.840	3.580	3.830	0.740	0.250	0.990
M4	3.070	2.930	3.740	3.980	0.810	0.240	1.050

Note. Upper table: The Visual-NIR and NIR colors of the Subaru NIR detections/A HST star and their corresponding uncertainties. Middle/Lower tables: The intrinsic colors of supergiants and dwarfs from [Ducati et al. \(2001\)](#). The $V-I$ (in red), the Visual-NIR (in red) and the NIR (in blue) color index ranges of the Subaru NIR detections/A HST star can be seen in the middle and lower tables. These reflect an STR for each luminosity class.

^a The $J-H$, $H-K_S$, and $J-K_S$ indices for the middle and lower tables are calculated from the $-(V-J) + (V-H)$, $-(V-H) + (V-K_S)$, and $-(V-J) + (V-K_S)$, respectively.

3.4.3.1 Supergiant

In the scenario in which the A HST star is an extra-galactic supergiant, the remaining analysis is relatively straightforward. Assuming a distance modulus of $\mu = 27.92 \pm 0.19$ mag for NGC5128 (Rejkuba, 2004), the combination of its absolute magnitude $M_{HST,A}^V = -7.69 \pm 0.22$ mag and its $V - I$ color range place the A HST star in the YSG⁵⁵ (e.g. a G1) part of the Hertzsprung-Russell (HR) diagram. However, the presence of supergiants in this region of Cen A should not be a surprise. Earlier VLT (Rejkuba *et al.*, 2001) and HST (Mould *et al.*, 2000) observations confirmed that young blue stars concentrated in OB associations exist in the region, believed to have formed in a recent ($\sim 10 - 15$ Myr ago) jet-induced star formation. In this context, supergiants are expected to be found in the vicinity, as young blue stars that left the main-sequence in the time elapsed. In order to estimate the age of the A HST star, I use isochrones for non-rotating stars with sub-solar (i.e. $Z = 0.6Z_{\odot}$, Rejkuba *et al.*, 2001) and solar (i.e. $Z = Z_{\odot}$, Salomé *et al.*, 2016) metallicities from Bertelli *et al.* (2009) and for non-rotating and rotating stars with solar metallicity from Ekström *et al.* (2012). One of these isochrones is shown as an example in the color-magnitude diagram (CMD) of figure 3.6. Based on these isochrones, the age⁵⁶ of the A HST star is estimated to be $\sim 10_{-3}^{+4}$ Myr, which is in excellent agreement with the age of the jet-induced star formation reported in previous studies.

3.4.3.2 Dwarf

In the scenario in which the A HST star is a foreground main-sequence dwarf, however, its distance has to be constrained in order to get a glimpse on its location within our Galaxy.

Based on its $V - I$ range (see lower table 3.1), its spectral type should be between $F5$ and $K1$. Assuming an intermediate spectral type (IST) to this range (e.g. $G3$), the A HST star should have an absolute magnitude of $M_{G3\ dwarf}^V \sim 5.10_{-1.40}^{+1.10}$ mag. Knowing both its apparent and absolute magnitudes, I can then estimate its distance modulus $\mu \sim 15.13_{-1.10}^{+1.40}$ mag and its luminosity distance $D_L^{G3\ dwarf} \sim 10.62_{-4.22}^{+9.61}$ kpc. Considering also its galactic latitude of $\sim 19.6^{\circ}$, the A HST star should be located at a vertical-to-the-galactic-plane distance of $D_{\perp}^{G3\ dwarf} \sim 3.56_{-1.41}^{+3.23}$ kpc. In turn, this suggests that if this is indeed a galactic source, then it should be part of the stellar halo of the Milky Way (e.g. Voigt, 1988; Norris, 1997).

Assuming a density profile for the galactic stellar halo from Deason *et al.* (2011) and integrating over a solid angle defined by the dimensions of the Subaru field along the line-of-sight towards NGC5128, the fraction of galactic halo stellar mass probed by the Subaru FoV can theoretically be estimated. This results in a total stellar mass of $M_{FoV}^{Total} \sim$

⁵⁵A YSG is a short-lived (i.e. $\sim 10^3$ yr) transitional evolutionary phase of a massive star with initial mass of $\sim 9 - 40 M_{\odot}$.

⁵⁶This is the median age of all the isochrones within the photometric uncertainties from all the models used.

Table 3.2: Parameters for the B and C HST stars.

Extra-galactic Supergiant								
HST Star	$V - I$	STR	IST ^a	m_V	M_V	Exp. m_{K_S}	Exp. m_H	Exp. m_J
units	mag	-	-	mag	mag	mag	mag	mag
uncert.	± 0.28	-	-	± 0.12	± 0.22	-	-	-
B	0.68	F5 – G0	F8	21.24	-6.68	$19.90^{+0.43}_{-0.37}$	$20.07^{+0.38}_{-0.35}$	$20.37^{+0.30}_{-0.27}$
C	1.97	K2 – K4	K3/3.5	23.20	-4.72	$19.91^{+0.28}_{-0.15}$	$20.01^{+0.32}_{-0.18}$	$20.75^{+0.25}_{-0.14}$
Galactic Dwarf								
HST Star	$V - I$	STR	IST ^a	m_V	μ	Lum. Dist.	Vert. Dist.	
units	mag	-	-	mag	mag	kpc	kpc	
uncert.	± 0.28	-	-	± 0.12	-	-	-	-
B	0.68	F1 – G8	G0	21.24	$16.54^{+1.50}_{-0.90}$	$20.32^{+20.23}_{-6.89}$	$6.82^{+6.78}_{-2.31}$	
C	1.97	K7 – M0	K7/M0	23.20	$14.80^{+0.30}_{-0.30}$	$9.12^{+1.35}_{-1.18}$	$3.06^{+0.45}_{-0.40}$	

Note. The first five columns are common in the two tables. These indicate 1) the HST star identification (the letters of figure 3.3), 2) the $V - I$ color index, 3) the STR corresponding to the $V - I$ color index on table 3.1, 4) the IST, and 5) the apparent V band magnitude. Upper table: For the extra-galactic supergiant scenario, column 6) indicates the absolute V band magnitude for the assumed distance modulus ($\mu = 27.92 \pm 0.19$ mag) for NGC5128, and columns 7), 8), and 9) indicate the expected K_S , H , and J band apparent magnitudes, respectively, for the chosen IST, derived by its $V - K_S$, $V - H$, and $V - J$ color indices on table 3.1. Lower table: For the galactic dwarf scenario, column 6) indicates the estimated distance modulus for the chosen IST, column 7) indicates the estimated luminosity distance, and column 8) indicates the estimated vertical-to-the-galactic-plane (luminosity) distance, using the galactic latitude of $\sim 19.6^\circ$.

^a The IST is chosen to be either the middle spectral type of the STR, or, in the case of an even STR, the average of the middle spectral types. If the STR has only two spectral types, then their average is chosen as the IST. The uncertainties in the columns 7), 8), and 9) of the upper table and 6), 7), and 8) of the lower table cover the entire corresponding STRs.

$0.39^{+0.39}_{-0.23} M_\odot^{57}$, which, provided it is in the form of one halo star, could potentially represent a K0 to M8 main-sequence dwarf. However, the expected mass range of the A HST star (i.e. $\sim 0.7 - 1.3 M_\odot^{58}$) does not significantly overlap with this mass range. Talking also into account a) that the peak of the initial mass function (IMF) is $\sim 0.18 - 0.25 M_\odot$, b) that the IMF traces the present day mass function (PDMF) relatively well for low-mass stars (e.g. [Bochanski et al., 2010](#)), and c) that the overlap of the color indices is more consistent in the case of supergiants, the galactic dwarf scenario for the A HST star can be considered as significantly less likely, although it cannot be excluded.

3.4.4 What about the B and C HST stars?

So far, the analysis suggests that the Subaru $> 3\sigma$ detections are, most likely, the NIR counterparts of the A HST star, which appears to be an extra-galactic YSG located within the OB associations along the path of the Cen A jet. However, the B and C HST stars (see figure 3.3) are not detected in the NIR.

⁵⁷This mass range reflects the different mass-to-light ratios (i.e. $\sim 1 - 5$) assumed for the stellar halo of the Milky Way by [Deason et al. \(2011\)](#).

⁵⁸As implied by its STR i.e. F5 to K1.

Similarly to section 3.4.3, I attempt to put a constraint on the spectral types of these stars for both luminosity classes through their $V - I$ color indices and estimate the corresponding quantities for the two scenarios, namely, the extra-galactic supergiant and the galactic main-sequence dwarf. The results are shown in table 3.2.

If these stars are extra-galactic supergiants, then their absolute visual magnitudes— as suggested by their HST V band photometry (see upper table 3.2) and the distance modulus of NGC5128— place them in the supergiant part of the HR diagram. Combining their visual magnitudes with their $V - I$ color ranges, it follows that the B HST star is a YSG (i.e. an $F8$) and the C HST star is an RSG (i.e. a $K3/3.5$). Similarly to section 3.4.3.1, various isochrones are used to estimate their ages, resulting in $\sim 16_{-3}^{+6}$ Myr and $\sim 25_{-9}^{+15}$ Myr, respectively. This suggests that the B and C HST stars are— on average— older than the A HST star, which could be a hint that there is an underlying age-spread in the evolved stellar populations of the region of ~ 15 Myr, although within the quoted uncertainties such an age-spread could also be minimal. Generally, however, both of these age estimations are in very good agreement with the age of the jet-induced star formation.

If these are foreground main-sequence dwarfs, then their vertical-to-the-galactic-plane distances would position them inside the stellar halo of our Galaxy (see lower table 3.2). Similarly to section 3.4.3.2, the ranges of their spectral types suggest that the expected masses of the B and C HST stars would be $\sim 0.8 - 1.5M_{\odot}$ and $\sim 0.4 - 0.5M_{\odot}$, respectively. Evidently, the total stellar mass of the galactic halo expected within the Subaru FoV overlaps with the mass of the C HST star but not with the mass of the B HST star. The galactic dwarf scenario can, therefore, be plausible only for the C HST star, leaving only the A and B HST stars as potential supergiants in Cen A. This, however, would only be valid under the assumption that all the galactic halo stellar mass probed by the Subaru FoV is “expressed” as one halo star. Under a more conservative assumption in which the probed galactic halo stellar mass is expressed as the sum of a few lower mass stars near the peak of the IMF (i.e. $\sim M5 - M8$ stars), it is reasonable to treat the C HST star also as an extra-galactic supergiant rather than as a galactic main-sequence dwarf.

3.5 Discussion of chapter 3

In this chapter, I have presented an extensive study of high angular resolution Subaru $J/H/K_S$ and archived HST $F555W/F814W$ data of a region along the path of the jet of Cen A, in which a recent jet-induced star formation is thought to have taken place.

Initially, I locate the Subaru FoV on the much larger HST FoV (see figure 3.1), using the AO guide stars and the cardinal points as reference. The quoted proper motions (see section 3.3) of the two guide stars are negligible, which strongly indicates that the HST field stars should be located roughly at the same, with respect to the AO guide stars, positions also on the Subaru NIR images.

However, on the reduced J , H , and K_S band images (see figure 3.2) there is no obvious signal that can be considered as a stellar detection. I use a low-pass filter with a 10 pixel Gaussian kernel on the NIR images (see figure 3.4) in order to highlight hidden structures within the noise. This process reveals strong- $> 3\sigma$ above the background- signal (see figure 3.5) at the A HST star's expected position.

An extensive statistical analysis (see section 3.4.1) shows that a purely random origin of this strong NIR signal is highly unlikely and, therefore, that it should originate from the presence of an underlying source, which systematically produces higher than expected flux at the position of the A HST star. In turn, this strongly implies that the $> 3\sigma$ detections are, most likely, the NIR counterparts of the A HST star.

In order to constrain its the nature, I photometrically examine two different possibilities. The A HST star can be either an extra-galactic supergiant, or a foreground main-sequence dwarf (see section 3.4.3). Thorough examination of both of these possibilities (see sections 3.4.3.1, 3.4.3.2) favors the extra-galactic YSG scenario, mainly on the basis of its absolute magnitude, its significantly better color index overlap, and its age estimation, which appears to be in excellent agreement with the age of the jet-induced star formation. Using similar argumentation, but based only on their HST photometry, I promote the extra-galactic supergiant scenario also for the B (YSG) and C (RSG) HST stars, although the latter could- under certain assumptions- be a galactic main-sequence dwarf as well (see section 3.4.4, table 3.2).

Supergiants, however, should be naturally expected in this part of Cen A. Previous studies (e.g. Blanco *et al.*, 1975; Graham and Price, 1981; Graham, 1998; Fassett and Graham, 2000; Mould *et al.*, 2000; Rejkuba *et al.*, 2001) have found young blue stars in the region and proposed a jet-HI cloud interaction that triggered star formation $\sim 10 - 15$ Myr ago as the favored explanation for their formation. In this framework, finding YSGs and RSGs in this region should not be a surprise, since, within this time-frame, the most massive of these young blue stars will have evolve past the main-sequence, entering the supergiant phase. If these young stars are indeed jet-induced, then accurately mapping the distribution of the supergiants of the region could reveal the recent interaction history between the jet and the gas clouds, potentially providing important information about the underlying physics of positive AGN feedback.

Finally, finding candidate YSGs can also be very important for the further development of the stellar evolutionary models, since the evolution of massive stars after the main-sequence phase is still largely unknown (e.g. Langer, 2012). YSGs lie in the instability strip (i.e. $T_{eff} \sim 5000 - 6000$ K) at the brighter part of the HR diagram, also known as the HR gap (e.g. Castro *et al.*, 2014). Stars in the HR gap can be evolving either from the main-sequence to the giant/supergiant phase, or from the RSG phase to hotter temperatures (e.g. Gordon *et al.*, 2016). Both transitions are thought to happen in short time-scales after the end of the main-sequence phase, which could provide an explanation for the small number

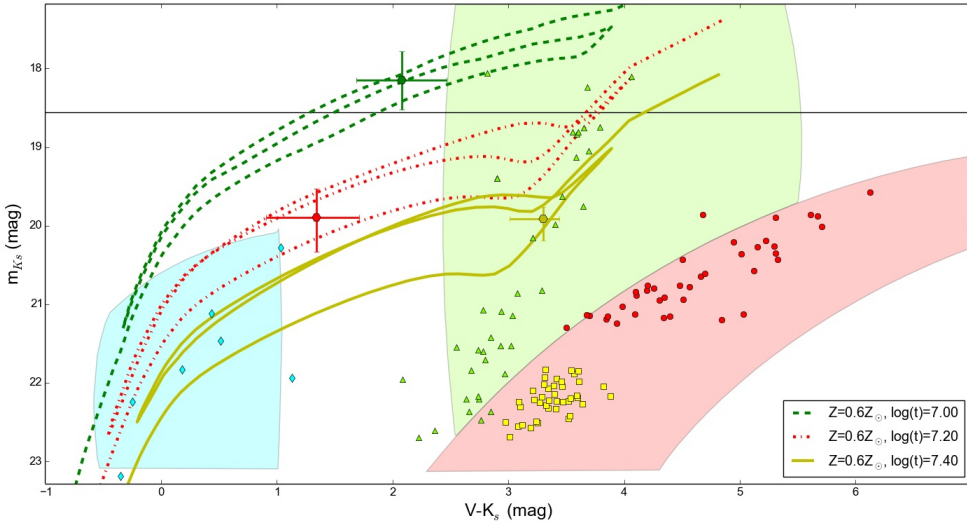


Figure 3.6: The Visual-NIR CMD of figure 3 from [Gullieuszik et al. \(2008\)](#). The BSGs (in diamond symbols), RSGs (in triangles), RGB (in squares), and AGB (in filled circles) stars of UKS 2323-326 are shown. The three (red, green, and blue) shaded areas show the equivalent stellar sequences (see figure 12 of [Rejkuba et al. \(2001\)](#)) of NGC5128. The three colored (green, red, and yellow) points and their error bars show the positions of the A, B, and C HST stars, respectively, and their corresponding photometric uncertainties on the CMD. The green (dashed), the red (dashed-dotted), and the yellow (solid) lines show example isochrones ([Bertelli et al., 2009](#)) for the median ages of the three HST stars. Finally, the black solid line shows the Subaru K_S band limiting magnitude.

of stars detected so far in the HR gap (e.g. [Langer, 2012](#)). Therefore, all new YSGs found in this part of the HR diagram are of great interest because they can provide additional (empirical) constraints to the stellar evolutionary theory.

3.5.1 Resolving extra-galactic stars beyond our LG

The present attempt to resolve individual stars in objects outside our LG, using 8-meter class telescopes observations, is not the first. A number of authors (e.g. [Bresolin et al., 2001, 2002](#); [Castro et al., 2008](#); [Ohyama and Hota, 2013](#)) have conducted spectroscopic studies of isolated blue (i.e. OB) stars in relatively nearby galaxies, while [Rejkuba et al. \(2001\)](#) performed a photometric study of the stellar halo of NGC5128 (part of which is the region discussed in this chapter) using FORS1 and ISAAC VLT observations. Non of these studies, however, make use of AO assisted observations.

The only other AO assisted photometric study of extra-galactic stellar populations was conducted by [Gullieuszik et al. \(2008\)](#), using data taken with the MAD instrument on the VLT. They managed to resolve blue supergiants (BSGs), RSGs, AGB, and red giant branch

(RGB) stars with $m_{K_S} \leq 22$ mag, at the center of the irregular dwarf galaxy UKS 2323-326. This is the most relevant study to the one presented here, since both studies use ground-based, AO assisted observations to resolve extra-galactic dense stellar populations.

Figure 3.6 shows a comparison between the stellar populations of UKS 2323-326 and NGC5128. In this plot, I reproduce the CMD of figure 3 from [Gullieuszik et al. \(2008\)](#) with the (roughly outlined) BSG, RSG, and AGB/RGB stellar sequences⁵⁹ of NGC5128 and the A, B, and C HST stars over-plotted. For this, the stars of UKS 2323-326 are projected to NGC5128's distance, by adding their distance moduli difference (i.e. $\delta\mu \sim 1.18 \pm 0.24$ ⁶⁰) to the apparent magnitudes of the stars of UKS 2323-326. Finally, the black solid line indicates the limiting magnitude of the Subaru K_S band.

Although the stellar populations of the two galaxies appear to overlap well, the stars of NGC5128 cover a significantly wider area on the CMD, extending towards redder $V - K_S$ values than those of UKS 2323-326, which leads to an offset of their center lines. This effect could be due to the wider range of metallicities of NGC5128's stars ([Rejkuba et al., 2001](#)), which is consistent with the general trend that dwarf galaxies have lower metallicities than giant galaxies ([Mateo, 1998](#)). Furthermore, this offset seems to be dominant mainly in the red populations. This is evident by the better overlap—compared to that between the RSGs and RGB/AGB stars—of the BSGs of the two galaxies, suggesting that this offset is, likely, not a systematic error. This serves, therefore, as an extra indication that the A HST star's position in the YSG part of the CMD is determined relatively accurately. Other factors could also contribute to this offset, e.g. uncertainties in the distance moduli of the two galaxies and/or differences in the reddening of the two fields, although these are not expected to radically change the global picture.

From an observational point of view, however, the present study was clearly more difficult. On one side, UKS 2323-326 is by a factor of $\sim 1.5 - 2$ closer than NGC5128, while on the other, [Gullieuszik et al. \(2008\)](#) worked with data that were $\sim 3 - 4$ deeper⁶¹ than the Subaru data used in this chapter. This is immediately evident on the CMD of figure 3.6. The position of the black solid line shows that the current Subaru observations allow for the detection of only a small number of stars located at the brightest tip of the YSG/RSG branch of NGC5128 in the much larger field of [Rejkuba et al. \(2001\)](#). Detecting one of these stars is a direct consequence of observing a field within a region where star formation has recently taken place, which increases the probability of observing bright supergiants.

Despite the low photometric depth of the current Subaru observations, the potential of the AO capabilities is clearly demonstrated, since the achieved NIR angular resolution

⁵⁹The main stellar distribution of figure 12 from [Rejkuba et al. \(2001\)](#) is chosen as the AGB/RGB branch of NGC5128. Distinction between its BSGs and RSGs is performed by applying approximate $V - K_S$ cut-offs (i.e. $V - K_S < 1$ and $2.5 < V - K_S < 5.5$, respectively) from table 3.1.

⁶⁰A distance modulus of $\mu^{UKS2323-326} = 26.74 \pm 0.15$ mag is adopted for UKS 2323-326 ([Gullieuszik et al., 2008](#)).

⁶¹In integration time, which reflects a SNR of ~ 5 times higher than the current Subaru data.

is comparable to the optical angular resolution of the HST. This can be seen in figure 3.2, in which the two AO guide stars are well resolved in the NIR, similarly to the HST images of figure 3.3. This reflects that, provided a better SNR, the OB associations of Cen A should appear on the Subaru NIR images as they appear on the HST *F555W* and *F814W* images.

The present analysis, therefore, supports the conclusions of [Gullieuszik *et al.* \(2008\)](#). It is now possible to resolve extra-galactic dense stellar populations (e.g. OB associations) in galaxies beyond our LG potentially into individual stars, by using deep, AO assisted observations with the current 8-meter class telescopes. Future developments of the AO technology and the new generation of Extremely Large Telescopes (ELT) will enable the successful completion of more challenging tasks, propelling our understanding around the stellar populations of relatively distant galaxies to a new level.

Final Remarks

4.1 General outline

Throughout this dissertation, I tried to outline the impact that processes related to the central SMBHs can have on their host galaxies in post-merger systems through different forms of mechanical interactions either on the immediate surroundings (i.e. ~ 200 pc) of the nuclear region, i.e. via the presence of an SMBH recoil like in the case of NGC3718, or on larger distances from the center (i.e. ~ 15 kpc), i.e. via the detection of supergiants in a region long suspected to have undergone a recent jet-induced star formation like in the case of NGC5128. Since these mechanisms appear to be participating (at least) in the (partial co-)evolution of their host galaxies on different scales, they could be included under the general category of feedback⁶². Moreover, both of these forms of feedback have been theoretically predicted, however, candidate objects have been identified either based on considerably fewer evidence (e.g. an SMBH recoil – NGC3718 is perhaps the best candidate so far, at least, in terms of the co-existence of several independent evidence), or very rarely (e.g. jet-induced star formation – Cen A is the closest paradigm of this phenomenon), but not yet conclusively.

More specifically, most SMBH recoil candidates have been identified using one of the main recoil tracers, namely, either relative shifts between their broad and narrow

⁶²Strictly speaking, feedback in galaxies is usually considered to be one of the following: Feedback related to stellar winds, feedback from supernova explosions, and feedback from an AGN. An SMBH recoil could be considered as a form of mechanical feedback in the sense that a merger “feeds” the remnant with a second SMBH and the subsequent coalescence and recoil are able to “feed (mechanical) energy back” to the remnant by changing the central stellar density via the depletion of the core.

lines, or spatial offsets, but very rarely using both. On the one hand, objects like SDSSJ092712.65+294344.0 (Komossa *et al.*, 2008), E1821+643 (Robinson *et al.*, 2010), and SDSSJ105041.35+345631.3 (Shields *et al.*, 2009) are good SMBH recoil candidates selected by relative broad/narrow line shifts, but they are generally more distant ($z \geq 0.3$) and they exhibit features like double BLRs or double NLRs that allow space for alternative interpretations, e.g. double-peaked emitters. On the other hand, nearby ($z \leq 0.045$) objects like CXOJ122518.6+144545 (Jonker *et al.*, 2010), ESO 1327-2041 (Keeney *et al.*, 2011), and M87 (Batcheldor *et al.*, 2010) show only spatial offsets and, therefore, they cannot be conclusive cases of SMBH recoils, since acceleration by jets and accretion of cores of satellite galaxies could also be possible explanations.

The most promising candidate SMBH recoil host so far was CID-42 because it shows both kinematic and spatial signatures (Civano *et al.*, 2010, 2012). It has a double optical nucleus, two (or possibly three) NLR components, X-ray emission only from the one core (i.e. the SE), a relative shift between its broad and narrow lines ($\sim 1300 \text{ Km s}^{-1}$), and a spatial offset ($\sim 2 \text{ kpc}$). In the recoil scenario, the non-X-ray emitting core (i.e. the NW) could be the center of the galaxy, while the X-ray emitting core could be its recoiled SMBH, but a case of a dual AGN cannot be ruled out, provided that the non-X-ray emitting core is an obscured AGN. Its distance ($z \sim 0.36$), however, is a limiting factor for the fine-detail observations of its central region that are necessary to make a clear SMBH recoil case. This is not a problem in the case of NGC3718, since its proximity allows for a detailed view of its central region. The co-existence of the relative shift ($\sim 355 \text{ Km s}^{-1}$) between its broad and narrow $H\alpha$ lines, the (candidate X-shaped) radio and NIR emission (potentially coincident) offsets, the depleted core, and the various indications of a recent merger are enough and mostly independent evidence to “award the best candidacy” for hosting an actual SMBH recoil to NGC3718. When all these elements are put together they create a picture compatible with an SMBH recoil, leaving it, likely, as the only possible explanation.

The picture around candidate hosts for jet-induced star formation is rather similar. Apart from the NGC5128/Cen A (e.g. Graham, 1998; Fassett and Graham, 2000; Mould *et al.*, 2000; Rejkuba *et al.*, 2001), there are only three other cases of candidate objects to host jet-induced star forming regions, namely, 3C 285 (van Breugel and Dey, 1993), Minkowski’s Object (near the Fanaroff-Riley type I (FR-I) radio source NGC541) (van Breugel *et al.*, 1985), and the high-redshift ($z \sim 3.8$) radio source 4C 41.17 (Bicknell *et al.*, 2000; De Breuck *et al.*, 2005; Papadopoulos *et al.*, 2005). These objects, however, are considerably more distant ($D \geq 75 \text{ Mpc}$) and, therefore, detailed studies of their jet-induced stellar populations at an individual level are not possible with present-day instrumentation. On the contrary, the proximity of Cen A ($D \sim 3.8 \text{ Mpc}$) is what allowed the identification of young blue stars (previous studies) and supergiants (this work). More detailed studies of the distribution of the supergiants of the region could clarify the connections between the propagation of the shocks at the tips of jets through the ISM/intergalactic medium (IGM) and the turbulence they can cause in the gas clouds to trigger the birth of

new stars, ultimately improving our understanding of the phenomenon of positive AGN feedback.

Finally, the great potential of the current NIR, ground-based, AO assisted observations is underlined throughout this work. The analysis of NGC3718 is indicative of the observational detail that can be achieved with a spatial resolution of ~ 15 parsec⁶³ when observing the central region of a nearby galaxy, while the analysis of NGC5128 clearly shows that it is possible to resolve relatively dense stellar associations into individual stars in galaxies beyond our LG. The unprecedentedly high resolution of the present-day 8–10-meter class telescopes and the upcoming optical/NIR instruments on the next generation ELTs is expected to significantly boost our knowledge around the fine structures in several different parts of nearby galaxies, which will help us to further constrain and fine-tune the theoretical models.

I hope that I have added a small piece to the puzzle of our knowledge around how our Universe creates and evolves its building blocks that we call “Galaxies”, which are the islands where the magnificent miracle of Life can occur. As a closure to this work, I would like to briefly summarize the most important points of the two case studies I performed during my PhD:

4.2 Summary of chapter 2

In chapter 2, I presented an extensive study of NGC3718 using NIR Subaru imaging, a 6 cm e-Merlin radio map, previously published results, and predictions from theoretical models, which revealed the following:

- i The NIR color maps do not show signs of a large-scale constant color gradient, which indicates that our view towards the nucleus of NGC3718 has to be largely unaffected by (at least, non-uniform) extinction.
- ii An offset red blob is clearly seen on the NIR color maps, lying at a projected distance of ~ 4.25 pc from the center of the underlying stellar bulge. Additionally, the peak of the e-Merlin 6 cm radio emission also appears to originate from an offset position, which is closer to the offset NIR red blob than to the center of the stellar bulge.
- iii The NIR light decomposition of the innermost ~ 0.5 arcsec reveals a contribution (up to $\sim 50\%$) from hot (up to ~ 1000 K) dust to the incoming light, indicating the presence of gas in that region.
- iv An extended elongated structure ~ 1 arcsec across is seen on the e-Merlin 6 cm radio map, probably indicating a small-scale bipolar jet. Additionally, a second and

⁶³This is the equivalent to ~ 170 mas angular resolution at a distance of NGC3718, namely, $D \sim 17.4$ Mpc.

smaller one (i.e. ~ 0.6 arcsec across) lies almost perpendicular to the first, potentially suggestive of an X-shaped radio source. These extended structures, however, may also contain contribution from supernova remnant related emission.

- v A clear disagreement between the $M_{\text{BH}} - L$ and $M_{\text{BH}} - \sigma$ scaling relations when the values of NGC3718 are used, along with the shape of its surface brightness profile, reveal an amount of light deficit in the form of a depleted core ~ 200 pc across. This translated to mass reflects an $M_{\text{def}} \sim 19M_{\text{BH}}$.
- vi NGC3718 has mixed characteristics in two ways. At first, it has spiral-like photometry (i.e. an exponential disk component) but elliptical-like kinematics (seen as a bulge component with Sérsic index $n > 4$). Moreover, NGC3718 shares characteristics with both fainter, more rotationally supported, disk, coreless ellipticals, and giant, less rotationally supported, boxy, core ellipticals. These strongly imply that NGC3718 is likely the result of a merger.
- vii Finally, NGC3718 is likely the host of an SMBH recoil. Evidence for this include the offset NIR red blob with the, potentially coincident and X-shaped, offset radio emission, the presence of a depleted core in its surface brightness profile, and the relative shift between its broad and narrow $H\alpha$ lines.

4.3 Summary of chapter 3

In chapter 3, I have performed Subaru NIR and archived HST imaging data analysis of a region along the path of the jet of Cen A, in which a recent jet-induced star formation is thought to have taken place. The key results of the analysis are:

- i The total proper motions of the two guide stars between the epochs of the Subaru and the HST data is negligible. This indicates that the HST field stars should lie roughly at the same, with respect to the guide stars, positions also on the Subaru NIR images.
- ii Strong- $> 3\sigma$ above the background- signal is found at the expected position of the brightest HST star on all low-pass filtered NIR images. The probability that such a signal is the result of random background fluctuations alone, in three independent measurements and at the same position is negligible (i.e. $\leq 2.5 \times 10^{-7}\%$). This suggests that the strong NIR signal, most likely, originates from the NIR counterparts of the brightest HST star.
- iii The nearly perfect overlap between the color indices (i.e. $V - I$, visual-NIR, and NIR) of the brightest HST star and its absolute magnitude suggest that this is, likely, an extra-galactic YSG. Furthermore, its age estimation (i.e. 10_{-3}^{+4} Myr) is in excellent agreement with the age of the jet-induced star formation (i.e. $\sim 10 - 15$ Myr), which is believed to have created the young blue stars that are present in this part

of NGC5128. Starting from this point, the presence of supergiants in the region is naturally expected.

- iv Based only on their HST photometry, the second (YSG) and third (RSG) brighter HST stars are, probably, also supergiants located in NGC5128, since their ages estimations (i.e. $\sim 16_{-3}^{+6}$ Myr and $\sim 25_{-9}^{+15}$ Myr, respectively) are also in very good agreement with the age of the jet-induced star formation. However, under certain assumptions, the third brighter HST star can also be a foreground galactic dwarf.

Appendix A – On the Subaru data reduction

In appendix A, I discuss the reduction process of the Subaru data set. Generally, data reduction is necessary in order to remove systematic noise and known artifacts that accumulate on the science images during data acquisition. The most important of these are:

- i **Dark Current:** It is generated by thermal electrons that build up in the pixels and depends on the detector's temperature and the exposure time. The dark current is significantly reduced by keeping the detector at a low operating temperature (i.e. $\sim 60 - 70$ K).
- ii **Readout Noise:** It is due to accumulated noise from the electronics comprising the detector i.e. the chip, the preamplifier, the Analog-to-Digital Converter etc. during the detector's operation.
- iii **Hot/Dead Pixels:** A small number of damaged pixels (i.e. $\sim 1\%$, collectively called bad pixels) on the detector array recording either no/peculiar values (i.e. dead pixels), or abnormally high values (i.e. hot pixels).

The Hawaii-IIRG 2048×2048 pixels² detector has 32 readout channels (i.e. a channel per 64 pixel interval) that introduce the 32-strip noise pattern seen in figure A.1. In order to correct for this artifact, there are 8 columns of "reference pixels" (i.e. 4 at the beginning and 4 at the end of the array), which are identical to the main pixels of the detector, but not light-sensitive. Their job is to record the combined dark current and readout noise that build up during an exposure.

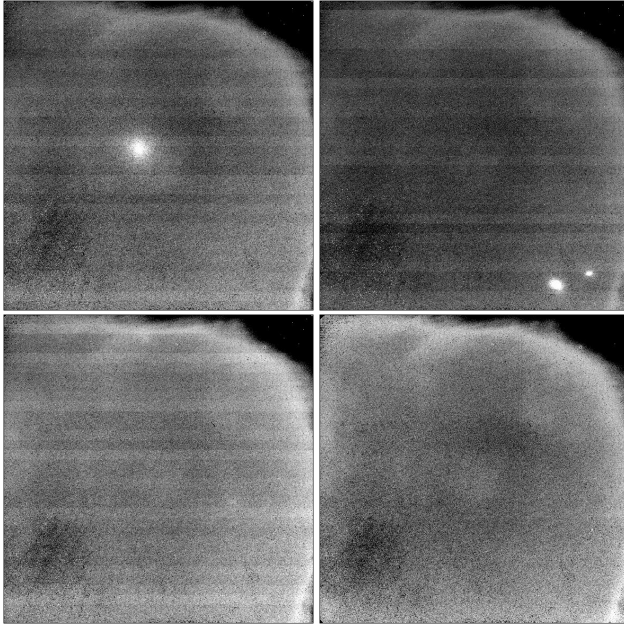


Figure A.1: Examples of raw images of NGC3718 (top left), Cen A (top right), sky (Cen A data set – bottom left), and flat-field (bottom right) from the HiCIAO instrument, in which the 32-strip noise pattern and the bad pixels are clearly visible.

Using the information on the reference pixels of each raw image, I generate a 32-strip noise pattern, which is subsequently subtracted from the corresponding raw image. The de-stripped sky and flat-field images are then median stacked and used to generate bad pixel masks (BPM) (see figure A.2), in order to correct all the data for bad pixels.

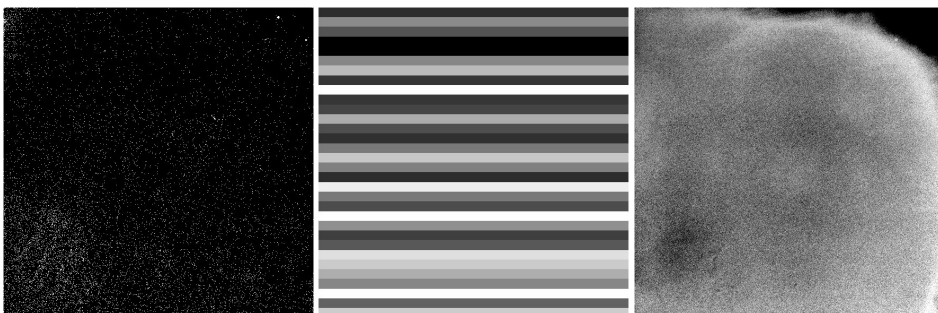


Figure A.2: Examples of a BPM (left) and a 32-strip noise pattern (middle) used to correct all the raw images and an example of a corrected sky image (Cen A data set – right).

Having all the data corrected for systematic noise and known artifacts, I proceed to the final stage of the reduction, namely, correcting the science images for the sky contribution and flat-field effects, in order to produce the final individual images.

The sky in the NIR has emission contributions from hydroxyl, water, and oxygen molecules in the atmosphere, as well as, from zodiacal light, scattered moonlight, and thermal emission from the atmosphere. To correct for the sky emission, the median stacked sky image (taken in an empty patch of the sky close to the science target) is subtracted from each individual science image⁶⁴.

The final reduction step is the flat-fielding. Each pixel of the detector has a slightly different response to incident light (i.e. within $\sim 1 - 2\%$). This is quantified using an image of a uniformly illuminated surface, or in other words, a flat-field image. Any differences in the recorded pixel values, therefore, should directly reflect differences in their response to the same amount of incident light. Dividing the science images with a normalized flat-field will correct for this systematic.

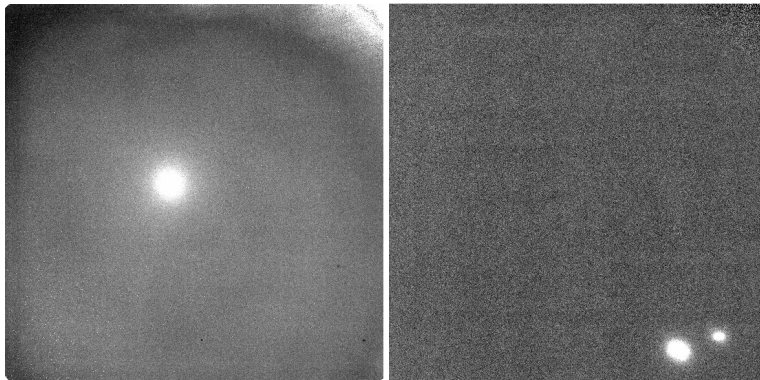


Figure A.3: An example of the final image of NGC3718 (without the sky subtracted – left) and of Cen A (right).

The entire NIR reduction process can be briefly summarized as follows:

$$I_{sci.}^{final} = \left(\frac{I_{sci.}^i - S_{med.}}{(F_{norm, med.})} \right), \quad (\text{A.1})$$

⁶⁴Normally, the reduction process would be identical for both the NGC3718 and the Cen A data sets. However, due to the absence of sky images from the NGC3718 data set, sky subtraction was performed after flat-fielding and median stack, as described in section 2.2.1.

where $I_{sci.}^{final}$ is the final individual science image, $I_{sci.}^i$ is the de-stripped and bad pixel corrected individual science image, and $S_{med.}$ and $F_{norm, med.}$ are the median stacked sky and the normalized median stacked flat-field images, respectively. The final individual science images (see figure A.3) are then undithered and median stacked, to produce the final images of figures 2.3 and 3.2.

B

Appendix B – On the influence of the dust lane

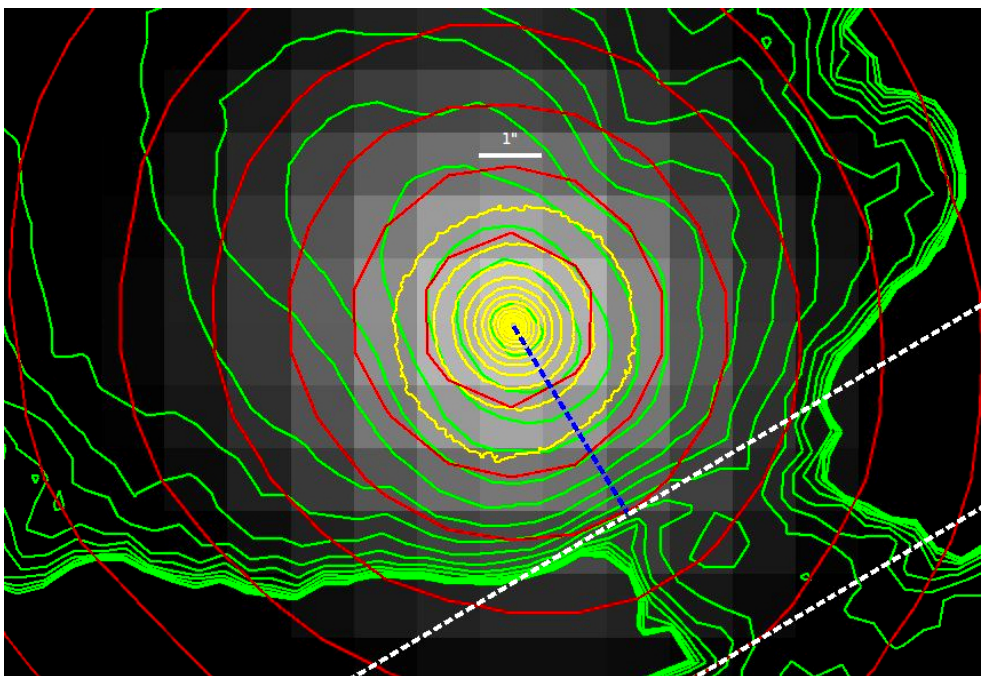


Figure B.1: The 2MASS K_S band image of NGC3718. Over-plotted are the 1) SDSS r band ($\sim 0.6 \mu\text{m}$) contours in green, 2) 2MASS K_S band contours in red, 3) Subaru K_S band contours in yellow, and 4) distance (blue dashed line, length ~ 3.5 arcsec) of the optical/NIR peak flux positions to the beginning of the dust lane (white dashed box).

In appendix B, I present additional evidence to those discussed in section 2.4, concerning the influence of the dust lane on our line-of-sight towards the nucleus of NGC3718.

In order to demonstrate this more clearly, I present the 2MASS K_S band image of NGC3718 in figure B.1. What can be immediately noticed is that the 2MASS K_S band contours (shown in red) appear to be almost completely unaffected by the dust lane. More specifically, their shape is significantly rounder and better defined than the contours of the SDSS r band (shown in green), which show severe deformation due to the presence of foreground dust in the region. Moreover, the Subaru K_S band contours (shown in yellow) appear to be similar to a higher resolution extrapolation of the 2MASS K_S band contours as one would expect, rather than to the heavily distorted contours of the SDSS r band. Additionally, the innermost ~ 4 arcsec of NGC3718 in the Subaru K_S band are ~ 1.5 arcsec away from the position where the deformation of the contours of the SDSS r band becomes catastrophic (i.e. the beginning of the dust lane – outlined by the white dashed box).

Therefore, I consider as safe to treat the nucleus of NGC3718 as being unaffected by the dust lane, when I attempt an interpretation of the NIR color maps.

Appendix C – On the alignment of the z - J bands

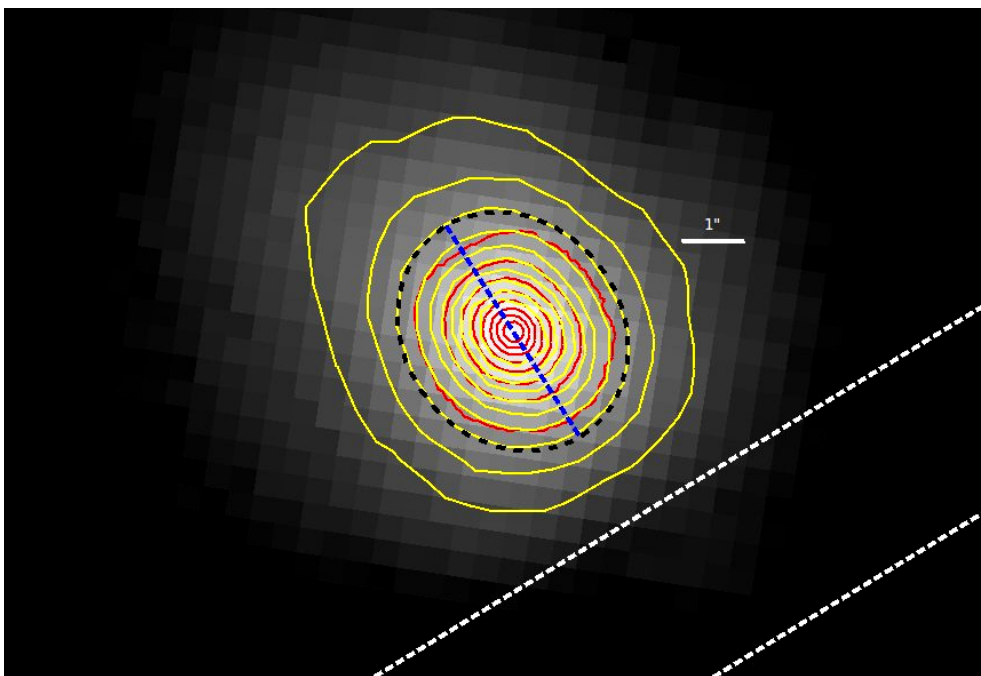


Figure C.1: The SDSS z band image of NGC3718. Over-plotted are the 1) SDSS z band contours in yellow and 2) Subaru J band contours in red. The black dashed ellipse and the blue dashed line mark the central ~ 4 arcsec of NGC3718, indicating the symmetry of the SDSS z band contours in this region.

In appendix C, I discuss the validity of the astrometric calibration (see section 2.3.5) applied on the Subaru images.

For a better illustration of this process, I present the SDSS z band image of NGC3718 in figure C.1. This image shows a black dashed ellipse with its ~ 4 arcsec major axis (shown by the blue dashed line) indicating the approximate radial distance where the shape of the SDSS z band contours starts to deviate from symmetry with respect to the position of the peak flux. What is immediately evident, is that the contours of the SDSS z band (shown in yellow) are relatively round, well defined, but more importantly symmetric within the region defined by the black ellipse. They also appear to be almost entirely unaffected by the dust lane, especially when compared to the contours of the SDSS r band (shown in green contours in figure B.1), at least within the region of interest and, therefore, they are considered to be suitable for deriving an accurate photo-center estimation for NGC3718 in this band. Additionally, the J band contours appear to be similar to the SDSS z band contours (i.e. similar roundness), since the ellipticities range between $\sim 0.09 - 0.12$ and $\sim 0.13 - 0.15$ for the two bands, respectively, in the radial interval between $\sim 0.5 - 1.5$ arcsec. This indicates that both bands are similarly unaffected by the dust lane.

I consider, therefore, that the symmetry of the contours of the SDSS z band image of NGC3718 in the central ~ 4 arcsec and their similarity with the contours of the Subaru J band, allow for the application of the centering method described in section 2.3.1. The photo-centers derived with this method were used to align the SDSS z with the Subaru J , H , and K_S bands in order to perform their astrometric calibration.

D

Appendix D – On the position of the e-Merlin radio map

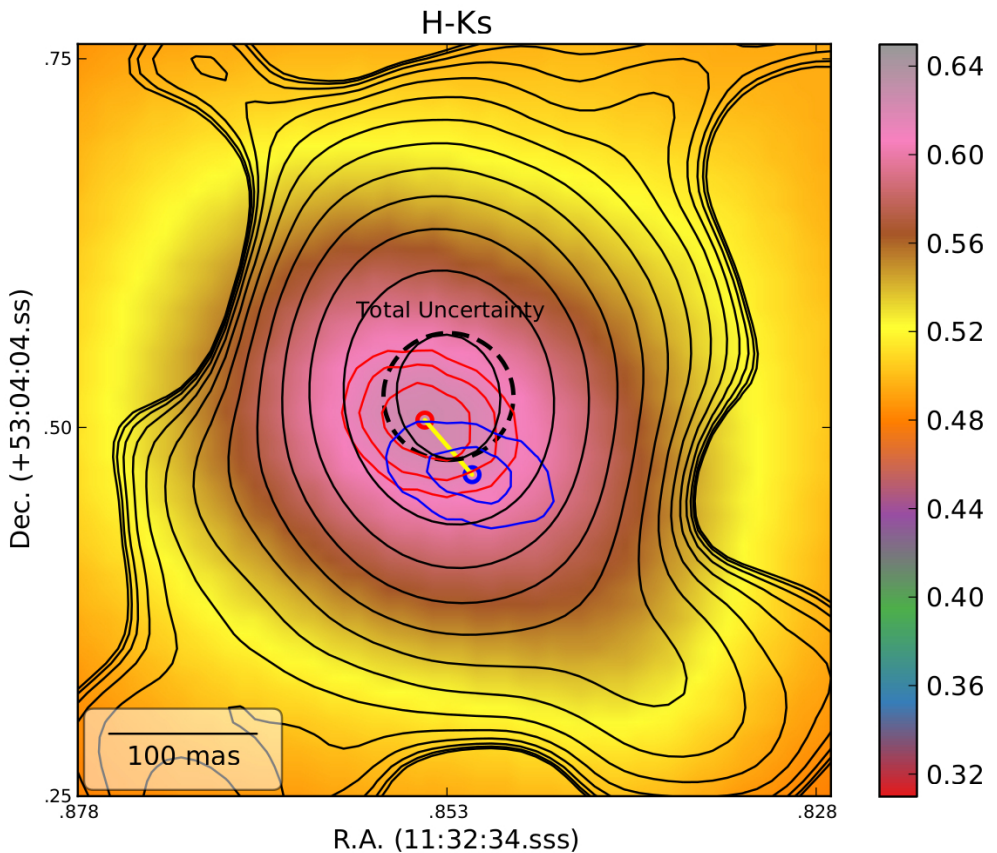


Figure D.1: Identical to figure 2.13, but with the radio map position calculated based on the old/outdated position of the phase reference source. This is equivalent to the peak radio position reported by *Krips et al. (2007)*.

In appendix D, I present a figure identical to figure 2.13, but in this case the 6 cm e-Merlin radio map is over-plotted on the $H - K_S$ map using the central position calculated based on the old/outdated position of the phase reference source in the e-Merlin catalogs. The central position of the radio emission in this figure is the same as the one reported by [Krips *et al.* \(2007\)](#), namely, $\alpha_{2000} = 11:32:34.8534 \pm 0.0005$ and $\delta_{2000} = +53:04:04.523 \pm 0.004$. This figure shows an almost perfect coincidence of the radio emission with the position of the red blob and is presented here for completeness reasons.



Bibliography

- Allen, D. A. (1975). *Infrared: The new astronomy*.
- Barnes, J. E. and Hernquist, L. (1992). Dynamics of interacting galaxies. *ARA&A*, **30**, 705–742.
- Barnes, J. E. and Hernquist, L. (1996). Transformations of Galaxies. II. Gasdynamics in Merging Disk Galaxies. *ApJ*, **471**, 115.
- Batcheldor, D., Robinson, A., Axon, D. J., Perlman, E. S., and Merritt, D. (2010). A Displaced Supermassive Black Hole in M87. *ApJ*, **717**, L6–L10.
- Beckmann, V. and Shrader, C. (2012). The AGN phenomenon: open issues. In *Proceedings of "An INTEGRAL view of the high-energy sky (the first 10 years)" - 9th INTEGRAL Workshop and celebration of the 10th anniversary of the launch (INTEGRAL 2012). 15-19 October 2012. Bibliotheque Nationale de France, Paris, France. Published online at <http://pos.sissa.it/cgi-bin/reader/conf.cgi?confid=176>, id.69, page 69.*
- Begelman, M. C., Blandford, R. D., and Rees, M. J. (1980). Massive black hole binaries in active galactic nuclei. *Nature*, **287**, 307–309.
- Bekenstein, J. D. (1973). Gravitational-Radiation Recoil and Runaway Black Holes. *ApJ*, **183**, 657–664.
- Bekki, K. (1997). Formation of Polar-Ring S0 Galaxies in Dissipative Galaxy Mergers. *ApJ*, **490**, L37–L40.

- Bekki, K. (1998). Formation of a Polar Ring Galaxy in a Galaxy Merger. *ApJ*, **499**, 635–649.
- Bell, E. F., McIntosh, D. H., Katz, N., and Weinberg, M. D. (2003). The Optical and Near-Infrared Properties of Galaxies. I. Luminosity and Stellar Mass Functions. *ApJS*, **149**, 289–312.
- Bertelli, G., Nasi, E., Girardi, L., and Marigo, P. (2009). Scaled solar tracks and isochrones in a large region of the Z-Y plane. II. From 2.5 to 20 M stars. *A&A*, **508**, 355–369.
- Bicknell, G. V., Sutherland, R. S., van Breugel, W. J. M., Dopita, M. A., Dey, A., and Miley, G. K. (2000). Jet-induced Emission-Line Nebulosity and Star Formation in the High-Redshift Radio Galaxy 4C 41.17. *ApJ*, **540**, 678–686.
- Blanco, V. M., Graham, J. A., Lasker, B. M., and Osmer, P. S. (1975). Optical condensations and filaments in the northeast radio lobe of NGC 5128. *ApJ*, **198**, L63.
- Blecha, L., Cox, T. J., Loeb, A., and Hernquist, L. (2011). Recoiling black holes in merging galaxies: relationship to active galactic nucleus lifetimes, starbursts and the $M_{BH}-\sigma_*$ relation. *MNRAS*, **412**, 2154–2182.
- Bochanski, J. J., Hawley, S. L., Covey, K. R., West, A. A., Reid, I. N., Golimowski, D. A., and Ivezić, Ž. (2010). The Luminosity and Mass Functions of Low-mass Stars in the Galactic Disk. II. The Field. *AJ*, **139**, 2679–2699.
- Bournaud, F. and Combes, F. (2003). Formation of polar ring galaxies. *A&A*, **401**, 817–833.
- Bournaud, F., Jog, C. J., and Combes, F. (2005). Galaxy mergers with various mass ratios: Properties of remnants. *A&A*, **437**, 69–85.
- Bournaud, F., Jog, C. J., and Combes, F. (2007). Multiple minor mergers: formation of elliptical galaxies and constraints for the growth of spiral disks. *A&A*, **476**, 1179–1190.
- Boylan-Kolchin, M., Ma, C.-P., and Quataert, E. (2005). Dissipationless mergers of elliptical galaxies and the evolution of the fundamental plane. *MNRAS*, **362**, 184–196.
- Bresolin, F., Kudritzki, R.-P., Mendez, R. H., and Przybilla, N. (2001). Stellar Spectroscopy Far Beyond the Local Group. *ApJ*, **548**, L159–L163.
- Bresolin, F., Gieren, W., Kudritzki, R.-P., Pietrzyński, G., and Przybilla, N. (2002). Spectroscopy of Blue Supergiants in the Spiral Galaxy NGC 300. *ApJ*, **567**, 277–288.
- Bromm, V., Coppi, P. S., and Larson, R. B. (2002). The Formation of the First Stars. I. The Primordial Star-forming Cloud. *ApJ*, **564**, 23–51.
- Caldwell, N., Kirshner, R. P., and Richstone, D. O. (1986). Dynamics of the elliptical galaxy NGC 7097 measured from gas and stars. *ApJ*, **305**, 136–147.
- Caon, N., Capaccioli, M., and D’Onofrio, M. (1993). On the Shape of the Light Profiles of Early-Type Galaxies. *MNRAS*, **265**, 1013.

- Cappellari, M., Emsellem, E., Bacon, R., Bureau, M., Davies, R. L., de Zeeuw, P. T., Falcón-Barroso, J., Krajnović, D., Kuntschner, H., McDermid, R. M., Peletier, R. F., Sarzi, M., van den Bosch, R. C. E., and van de Ven, G. (2007). The SAURON project - X. The orbital anisotropy of elliptical and lenticular galaxies: revisiting the $(V/\sigma, \epsilon)$ diagram with integral-field stellar kinematics. *MNRAS*, **379**, 418–444.
- Castro, N., Herrero, A., Garcia, M., Trundle, C., Bresolin, F., Gieren, W., Pietrzyński, G., Kudritzki, R.-P., and Demarco, R. (2008). The Araucaria Project: VLT-spectroscopy of blue massive stars in NGC 55. *A&A*, **485**, 41–50.
- Castro, N., Fossati, L., Langer, N., Simón-Díaz, S., Schneider, F. R. N., and Izzard, R. G. (2014). The spectroscopic Hertzsprung-Russell diagram of Galactic massive stars. *A&A*, **570**, L13.
- Charmandaris, V., Combes, F., and van der Hulst, J. M. (2000). First detection of molecular gas in the shells of Cen A. *A&A*, **356**, L1–L4.
- Chitre, A. and Jog, C. J. (2002). Luminosity profiles of advanced mergers of galaxies using 2MASS data. *A&A*, **388**, 407–424.
- Civano, F., Elvis, M., Lanzuisi, G., Jahnke, K., Zamorani, G., Blecha, L., Bongiorno, A., Brusa, M., Comastri, A., Hao, H., Leauthaud, A., Loeb, A., Mainieri, V., Piconcelli, E., Salvato, M., Scoville, N., Trump, J., Vignali, C., Aldcroft, T., Bolzonella, M., Bressert, E., Finoguenov, A., Fruscione, A., Koekemoer, A. M., Cappelluti, N., Fiore, F., Giodini, S., Gilli, R., Impey, C. D., Lilly, S. J., Lusso, E., Puccetti, S., Silverman, J. D., Aussel, H., Capak, P., Frayer, D., Le Floch, E., McCracken, H. J., Sanders, D. B., Schiminovich, D., and Taniguchi, Y. (2010). A Runaway Black Hole in COSMOS: Gravitational Wave or Slingshot Recoil? *ApJ*, **717**, 209–222.
- Civano, F., Elvis, M., Lanzuisi, G., Aldcroft, T., Trichas, M., Bongiorno, A., Brusa, M., Blecha, L., Comastri, A., Loeb, A., Salvato, M., Fruscione, A., Koekemoer, A., Komossa, S., Gilli, R., Mainieri, V., Piconcelli, E., and Vignali, C. (2012). Chandra High-resolution observations of CID-42, a Candidate Recoiling Supermassive Black Hole. *ApJ*, **752**, 49.
- Combes, F., Boisse, P., Mazure, A., Blanchard, A., and Seymour, M. (2002). *Galaxies and cosmology*.
- Condon, J. J. (1987). A 1.49 GHz atlas of spiral galaxies with $B(T) = +12$ or less and $\delta = -45$ deg or greater. *ApJS*, **65**, 485–541.
- De Breuck, C., Downes, D., Neri, R., van Breugel, W., Reuland, M., Omont, A., and Ivison, R. (2005). Detection of two massive CO systems in 4C 41.17 at $z = 3.8$. *A&A*, **430**, L1–L4.
- de Vaucouleurs, G. (1948). Recherches sur les Nebuleuses Extragalactiques. *Annales d'Astrophysique*, **11**, 247.

- de Vaucouleurs, G., de Vaucouleurs, A., Corwin, Jr., H. G., Buta, R. J., Paturel, G., and Fouqué, P. (1991). *Third Reference Catalogue of Bright Galaxies. Volume I: Explanations and references. Volume II: Data for galaxies between 0^h and 12^h. Volume III: Data for galaxies between 12^h and 24^h.*
- Deason, A. J., Belokurov, V., and Evans, N. W. (2011). The Milky Way stellar halo out to 40 kpc: squashed, broken but smooth. *MNRAS*, **416**, 2903–2915.
- Di Matteo, T., Springel, V., and Hernquist, L. (2005). Energy input from quasars regulates the growth and activity of black holes and their host galaxies. *Nature*, **433**, 604–607.
- Dong, X. Y. and De Robertis, M. M. (2006). Low-Luminosity Active Galaxies and Their Central Black Holes. *AJ*, **131**, 1236–1252.
- Ducati, J. R., Bevilacqua, C. M., Rembold, S. B., and Ribeiro, D. (2001). Intrinsic Colors of Stars in the Near-Infrared. *ApJ*, **558**, 309–322.
- Dufour, R. J., Harvel, C. A., Martins, D. M., Schiffer, III, F. H., Talent, D. L., Wells, D. C., van den Bergh, S., and Talbot, Jr., R. J. (1979). Picture processing analysis of the optical structure of NGC 5128 /Centaurus A/. *AJ*, **84**, 284–301.
- Ekström, S., Georgy, C., Eggenberger, P., Meynet, G., Mowlavi, N., Wyttenbach, A., Granada, A., Decressin, T., Hirschi, R., Frischknecht, U., Charbonnel, C., and Maeder, A. (2012). Grids of stellar models with rotation. I. Models from 0.8 to 120 M_{\odot} at solar metallicity ($Z = 0.014$). *A&A*, **537**, A146.
- Emsellem, E., Cappellari, M., Krajnović, D., van de Ven, G., Bacon, R., Bureau, M., Davies, R. L., de Zeeuw, P. T., Falcón-Barroso, J., Kuntschner, H., McDermid, R., Peletier, R. F., and Sarzi, M. (2007). The SAURON project - IX. A kinematic classification for early-type galaxies. *MNRAS*, **379**, 401–417.
- Escala, A., Larson, R. B., Coppi, P. S., and Mardones, D. (2005). The Role of Gas in the Merging of Massive Black Holes in Galactic Nuclei. II. Black Hole Merging in a Nuclear Gas Disk. *ApJ*, **630**, 152–166.
- Faber, S. M., Tremaine, S., Ajhar, E. A., Byun, Y.-I., Dressler, A., Gebhardt, K., Grillmair, C., Kormendy, J., Lauer, T. R., and Richstone, D. (1997). The Centers of Early-Type Galaxies with HST. IV. Central Parameter Relations. *AJ*, **114**, 1771.
- Fassett, C. I. and Graham, J. A. (2000). Age, Evolution, and Dispersion of the Loose Groups of Blue Stars in the Northeast Radio Lobe of Centaurus A. *ApJ*, **538**, 594–607.
- Favata, M., Hughes, S. A., and Holz, D. E. (2004). How Black Holes Get Their Kicks: Gravitational Radiation Recoil Revisited. *ApJ*, **607**, L5–L8.
- Filippenko, A. V. and Sargent, W. L. W. (1985). A search for 'dwarf' Seyfert 1 nuclei. I - The initial data and results. *ApJS*, **57**, 503–522.

- Fitchett, M. J. and Detweiler, S. (1984). Linear momentum and gravitational waves - Circular orbits around a Schwarzschild black hole. *MNRAS*, **211**, 933–942.
- García-Burillo, S., Sempere, M. J., Combes, F., Hunt, L. K., and Neri, R. (2000). Anatomy of the counterrotating molecular disk in the spiral NGC 3593. $^{12}\text{CO}(1-0)$ interferometer observations and numerical simulations. *A&A*, **363**, 869–886.
- García-Burillo, S., Combes, F., Eckart, A., Tacconi, L. J., Hunt, L. K., Leon, S., Baker, A. J., Englmaier, P. P., Boone, F., Schinnerer, E., and Neri, R. (2003). NUGA: The IRAM Survey of AGN Spiral Hosts. In S. Collin, F. Combes, and I. Shlosman, editors, *Active Galactic Nuclei: From Central Engine to Host Galaxy*, volume 290 of *Astronomical Society of the Pacific Conference Series*, page 423.
- Garrington, S. T., Anderson, B., Baines, C., Battilana, J. A., Bentley, M. N., Brown, D., Burgess, P., Diamond, P. J., Kitching, G. J., McCool, R., Muxlow, T. W., Noble, R. G., Roddis, N., Spencer, R. E., and Thomasson, P. (2004). e-Merlin. In J. M. Oschmann, Jr., editor, *Ground-based Telescopes*, volume 5489 of *Proc. SPIE*, pages 332–343.
- Genzel, R., Eckart, A., Ott, T., and Eisenhauer, F. (1997). On the nature of the dark mass in the centre of the Milky Way. *MNRAS*, **291**, 219–234.
- Genzel, R., Schödel, R., Ott, T., Eckart, A., Alexander, T., Lacombe, F., Rouan, D., and Aschenbach, B. (2003). Near-infrared flares from accreting gas around the supermassive black hole at the Galactic Centre. *Nature*, **425**, 934–937.
- Glass, I. S. (1984). JHK colours of 'ordinary' galaxies. *MNRAS*, **211**, 461–469.
- Glass, I. S. and Moorwood, A. F. M. (1985). JHKL properties of emission-line galaxies. *MNRAS*, **214**, 429–447.
- Gordon, M. S., Humphreys, R. M., and Jones, T. J. (2016). Luminous and Variable Stars in M31 and M33. III. The Yellow and Red Supergiants and Post-red Supergiant Evolution. *ApJ*, **825**, 50.
- Graham, A. W. (2004). Core Depletion from Coalescing Supermassive Black Holes. *ApJ*, **613**, L33–L36.
- Graham, A. W., Erwin, P., Trujillo, I., and Asensio Ramos, A. (2003). A New Empirical Model for the Structural Analysis of Early-Type Galaxies, and A Critical Review of the Nuker Model. *AJ*, **125**, 2951–2963.
- Graham, J. A. (1998). Shocked Gas and Star Formation in the Centaurus A Radio Galaxy. *ApJ*, **502**, 245–252.
- Graham, J. A. and Price, R. M. (1981). The gaseous filaments in the northeast halo region of NGC 5128 /Centaurus A/. *ApJ*, **247**, 813–822.

- Gualandris, A. and Merritt, D. (2008). Ejection of Supermassive Black Holes from Galaxy Cores. *ApJ*, **678**, 780–797.
- Guedes, J., Callegari, S., Madau, P., and Mayer, L. (2011). Forming Realistic Late-type Spirals in a Λ CDM Universe: The Eris Simulation. *ApJ*, **742**, 76.
- Gullieuszik, M., Greggio, L., Held, E. V., Moretti, A., Arcidiacono, C., Bagnara, P., Baruffolo, A., Diolaiti, E., Falomo, R., Farinato, J., Lombini, M., Ragazzoni, R., Brast, R., Donaldson, R., Kolb, J., Marchetti, E., and Tordo, S. (2008). Resolving stellar populations outside the Local Group: MAD observations of UKS 2323-326. *A&A*, **483**, L5–L8.
- Hayano, Y., Takami, H., Oya, S., Hattori, M., Saito, Y., Watanabe, M., Guyon, O., Minowa, Y., Egner, S. E., Ito, M., Garrel, V., Colley, S., Golota, T., and Iye, M. (2010). Commissioning status of Subaru laser guide star adaptive optics system. In *Society of Photo-Optical Instrumentation Engineers (SPIE) Conference Series*, volume 7736 of *Society of Photo-Optical Instrumentation Engineers (SPIE) Conference Series*.
- Ho, L. C. (2009). Origin and Dynamical Support of Ionized Gas in Galaxy Bulges. *ApJ*, **699**, 638–648.
- Ho, L. C., Filippenko, A. V., and Sargent, W. L. W. (1997a). A Search for “Dwarf” Seyfert Nuclei. III. Spectroscopic Parameters and Properties of the Host Galaxies. *ApJS*, **112**, 315.
- Ho, L. C., Filippenko, A. V., Sargent, W. L. W., and Peng, C. Y. (1997b). A Search for “Dwarf” Seyfert Nuclei. IV. Nuclei with Broad $H\alpha$ Emission. *ApJS*, **112**, 391–414.
- Ho, L. C., Greene, J. E., Filippenko, A. V., and Sargent, W. L. W. (2009). A Search for “Dwarf” Seyfert Nuclei. VII. A Catalog of Central Stellar Velocity Dispersions of Nearby Galaxies. *ApJS*, **183**, 1–16.
- Holmberg, E. (1958). A photographic photometry of extragalactic nebulae. *Meddelanden fran Lunds Astronomiska Observatorium Serie II*, **136**, 1.
- Hopkins, P. F., Hernquist, L., Cox, T. J., Dutta, S. N., and Rothberg, B. (2008). Dissipation and Extra Light in Galactic Nuclei. I. Gas-Rich Merger Remnants. *ApJ*, **679**, 156–181.
- Hopkins, P. F., Cox, T. J., Dutta, S. N., Hernquist, L., Kormendy, J., and Lauer, T. R. (2009a). Dissipation and Extra Light in Galactic Nuclei. II. “Cusp” Ellipticals. *ApJS*, **181**, 135–182.
- Hopkins, P. F., Lauer, T. R., Cox, T. J., Hernquist, L., and Kormendy, J. (2009b). Dissipation and Extra Light in Galactic Nuclei. III. “Core” Ellipticals and “Missing” Light. *ApJS*, **181**, 486–532.
- Israel, F. P. (1998). Centaurus A - NGC 5128. *A&A Rev.*, **8**, 237–278.
- James, P., Bate, C., Wells, M., Wright, G., and Doyon, R. (1999). Do galaxy mergers form elliptical galaxies? A comparison of kinematic and photometric properties. *MNRAS*, **309**, 585–592.

- Jog, C. J. and Chitre, A. (2002). Spiral-like light profiles but elliptical-like kinematics in mergers of galaxies. *A&A*, **393**, L89–L93.
- Jonker, P. G., Torres, M. A. P., Fabian, A. C., Heida, M., Miniutti, G., and Pooley, D. (2010). A bright off-nuclear X-ray source: a type IIIn supernova, a bright ULX or a recoiling supermassive black hole in CXOJ122518.6+144545. *MNRAS*, **407**, 645–650.
- Karachentsev, I. D., Nasonova, O. G., and Courtois, H. M. (2013). Anatomy of Ursa Majoris. *MNRAS*, **429**, 2264–2273.
- Keeney, B. A., Stocke, J. T., Danforth, C. W., and Carilli, C. L. (2011). The Quasar/Galaxy Pair PKS 1327-206/ESO 1327-2041: Absorption Associated with a Recent Galaxy Merger. *AJ*, **141**, 66.
- Klypin, A. A., Trujillo-Gomez, S., and Primack, J. (2011). Dark Matter Halos in the Standard Cosmological Model: Results from the Bolshoi Simulation. *ApJ*, **740**, 102.
- Kocevski, D. D., Faber, S. M., Mozena, M., Koekemoer, A. M., Nandra, K., Rangel, C., Laird, E. S., Brusa, M., Wuyts, S., Trump, J. R., Koo, D. C., Somerville, R. S., Bell, E. F., Lotz, J. M., Alexander, D. M., Bournaud, F., Conselice, C. J., Dahlen, T., Dekel, A., Donley, J. L., Dunlop, J. S., Finoguenov, A., Georgakakis, A., Giavalisco, M., Guo, Y., Grogin, N. A., Hathi, N. P., Juneau, S., Kartaltepe, J. S., Lucas, R. A., McGrath, E. J., McIntosh, D. H., Mobasher, B., Robaina, A. R., Rosario, D., Straughn, A. N., van der Wel, A., and Villforth, C. (2012). CANDELS: Constraining the AGN-Merger Connection with Host Morphologies at $z \sim 2$. *ApJ*, **744**, 148.
- Komossa, S. (2012). Recoiling Black Holes: Electromagnetic Signatures, Candidates, and Astrophysical Implications. *Advances in Astronomy*, **2012**.
- Komossa, S., Zhou, H., and Lu, H. (2008). A Recoiling Supermassive Black Hole in the Quasar SDSS J092712.65+294344.0? *ApJ*, **678**, L81–L84.
- Kormendy, J. (1985). Brightness profiles of the cores of bulges and elliptical galaxies. *ApJ*, **292**, L9–L13.
- Kormendy, J. (1999). The Central Structure of Elliptical Galaxies and the Stellar-Dynamical Search for Supermassive Black Holes. In D. R. Merritt, M. Valluri, and J. A. Sellwood, editors, *Galaxy Dynamics - A Rutgers Symposium*, volume 182 of *Astronomical Society of the Pacific Conference Series*, page 124.
- Kormendy, J. (2009). The Elliptical-Spheroidal and Elliptical-Elliptical Galaxy Dichotomies. In S. Jogee, I. Marinova, L. Hao, and G. A. Blanc, editors, *Galaxy Evolution: Emerging Insights and Future Challenges*, volume 419 of *Astronomical Society of the Pacific Conference Series*, page 87.
- Kormendy, J. and Bender, R. (1999). The Double Nucleus and Central Black Hole of M31. *ApJ*, **522**, 772–792.

- Kormendy, J. and Bender, R. (2013). The Ly α σ^8 Correlation for Elliptical Galaxies with Cores: Relation with Black Hole Mass. *ApJ*, **769**, L5.
- Kormendy, J. and Ho, L. C. (2013). Coevolution (Or Not) of Supermassive Black Holes and Host Galaxies. *ARA&A*, **51**, 511–653.
- Kormendy, J. and Kennicutt, Jr., R. C. (2004). Secular Evolution and the Formation of Pseudobulges in Disk Galaxies. *ARA&A*, **42**, 603–683.
- Kormendy, J., Fisher, D. B., Cornell, M. E., and Bender, R. (2009). Structure and Formation of Elliptical and Spheroidal Galaxies. *ApJS*, **182**, 216–309.
- Kormendy, J., Bender, R., and Cornell, M. E. (2011). Supermassive black holes do not correlate with galaxy disks or pseudobulges. *Nature*, **469**, 374–376.
- Krips, M., Eckart, A., Neri, R., Pott, J. U., Leon, S., Combes, F., García-Burillo, S., Hunt, L. K., Baker, A. J., Tacconi, L. J., Englmaier, P., Schinnerer, E., and Boone, F. (2005). Molecular gas in NUClei of GALaxies (NUGA). III. The warped LINER NGC 3718. *A&A*, **442**, 479–493.
- Krips, M., Eckart, A., Krichbaum, T. P., Pott, J.-U., Leon, S., Neri, R., García-Burillo, S., Combes, F., Boone, F., Baker, A. J., Tacconi, L. J., Schinnerer, E., and Hunt, L. K. (2007). NUClei of GALaxies. V. Radio emission in 7 NUGA sources. *A&A*, **464**, 553–563.
- Lal, D. V. and Rao, A. P. (2007). Giant Metrewave Radio Telescope observations of X-shaped radio sources. *MNRAS*, **374**, 1085–1102.
- Langer, N. (2012). Presupernova Evolution of Massive Single and Binary Stars. *ARA&A*, **50**, 107–164.
- Liu, F. K., Wang, D., and Chen, X. (2012). Recoiling Supermassive Black Holes in Spin-flip Radio Galaxies. *ApJ*, **746**, 176.
- Malin, D. F. and Carter, D. (1980). Giant shells around normal elliptical galaxies. *Nature*, **285**, 643–645.
- Malin, D. F., Quinn, P. J., and Graham, J. A. (1983). Shell structure in NGC 5128. *ApJ*, **272**, L5–L7.
- Martini, P. and Pogge, R. W. (1999). Hubble Space Telescope Observations of the CFA Seyfert 2 Galaxies: The Fueling of Active Galactic Nuclei. *AJ*, **118**, 2646–2657.
- Mateo, M. L. (1998). Dwarf Galaxies of the Local Group. *ARA&A*, **36**, 435–506.
- Merritt, D. (2006). Mass Deficits, Stalling Radii, and the Merger Histories of Elliptical Galaxies. *ApJ*, **648**, 976–986.
- Merritt, D. and Ekers, R. D. (2002). Tracing Black Hole Mergers Through Radio Lobe Morphology. *Science*, **297**, 1310–1313.

- Merritt, D., Storchi-Bergmann, T., Robinson, A., Batcheldor, D., Axon, D., and Cid Fernandes, R. (2006). The nature of the HE0450-2958 system. *MNRAS*, **367**, 1746–1750.
- Mihos, J. C. and Hernquist, L. (1996). Gasdynamics and Starbursts in Major Mergers. *ApJ*, **464**, 641.
- Mould, J. R., Ridgewell, A., Gallagher, III, J. S., Bessell, M. S., Keller, S., Calzetti, D., Clarke, J. T., Trauger, J. T., Grillmair, C., Ballester, G. E., Burrows, C. J., Krist, J., Crisp, D., Evans, R., Griffiths, R., Hester, J. J., Hoessel, J. G., Holtzman, J. A., Scowen, P. A., Stapelfeldt, K. R., Sahai, R., Watson, A., and Meadows, V. (2000). Jet-induced Star Formation in Centaurus A. *ApJ*, **536**, 266–276.
- Naab, T. and Burkert, A. (2003). Statistical Properties of Collisionless Equal- and Unequal-Mass Merger Remnants of Disk Galaxies. *ApJ*, **597**, 893–906.
- Nipoti, C. and Binney, J. (2007). The role of thermal evaporation in galaxy formation. *MNRAS*, **382**, 1481–1493.
- Norris, J. E. (1997). Wide Field Spectroscopy THE Structure of the Galaxy. In E. Kontizas, M. Kontizas, D. H. Morgan, and G. P. Vettolani, editors, *Wide-field spectroscopy*, volume 212 of *Astrophysics and Space Science Library*, page 133.
- Ohyama, Y. and Hota, A. (2013). Discovery of a Possibly Single Blue Supergiant Star in the Intra-cluster Region of Virgo Cluster of Galaxies. *ApJ*, **767**, L29.
- Oosterloo, T. A. and Morganti, R. (2005). Anomalous HI kinematics in Centaurus A: Evidence for jet-induced star formation. *A&A*, **429**, 469–475.
- Ostriker, J. P. and Ciotti, L. (2005). Active galaxies and radiative heating: One contribution of 13 to a Discussion Meeting 'The impact of active galaxies on the Universe at large'. *Royal Society of London Philosophical Transactions Series A*, **363**, 667.
- Papadopoulos, P. P., Greve, T. R., Ivison, R. J., and De Breuck, C. (2005). A sensitive search for CO J = 1-0 emission in 4C 41.17: high-excitation molecular gas at $z = 3.8$. *A&A*, **444**, 813–819.
- Perley, R. A. and Butler, B. J. (2013). An Accurate Flux Density Scale from 1 to 50 GHz. *ApJS*, **204**, 19.
- Peterson, B. M. (1997). *An Introduction to Active Galactic Nuclei*.
- Pier, J. R., Munn, J. A., Hindsley, R. B., Hennessy, G. S., Kent, S. M., Lupton, R. H., and Ivezić, Ž. (2003). Astrometric Calibration of the Sloan Digital Sky Survey. *AJ*, **125**, 1559–1579.
- Pignatelli, E., Corsini, E. M., Vega Beltrán, J. C., Scarlata, C., Pizzella, A., Funes, J. G., Zeilinger, W. W., Beckman, J. E., and Bertola, F. (2001). Modelling gaseous and stellar kinematics in the disc galaxies NGC 772, 3898 and 7782. *MNRAS*, **323**, 188–210.

- Pott, J.-U., Hartwich, M., Eckart, A., Leon, S., Krips, M., and Straubmeier, C. (2004). Warped molecular gas disk in NGC 3718. *A&A*, **415**, 27–38.
- Primack, J. R. (2015). Cosmological Structure Formation. *ArXiv e-prints*.
- Rejkuba, M. (2004). The distance to the giant elliptical galaxy NGC 5128. *A&A*, **413**, 903–912.
- Rejkuba, M., Minniti, D., Silva, D. R., and Bedding, T. R. (2001). Stellar populations in NGC 5128 with the VLT: Evidence for recent star formation. *A&A*, **379**, 781–797.
- Reshetnikov, V. and Sotnikova, N. (1997). Global structure and formation of polar-ring galaxies. *A&A*, **325**, 933–942.
- Reshetnikov, V. P. and Combes, F. (1994). Kinematics and dark haloes of polar-ring galaxies. *A&A*, **291**, 57–73.
- Ridgway, S. T., Joyce, R. R., White, N. M., and Wing, R. F. (1980). Effective temperatures of late-type stars - The field giants from K0 to M6. *ApJ*, **235**, 126–137.
- Robinson, A., Young, S., Axon, D. J., Kharb, P., and Smith, J. E. (2010). Spectropolarimetric Evidence for a Kicked Supermassive Black Hole in the Quasar E1821+643. *ApJ*, **717**, L122–L126.
- Salomé, Q., Salomé, P., and Combes, F. (2015). Jet-induced star formation in 3C 285 and Minkowski's Object. *A&A*, **574**, A34.
- Salomé, Q., Salomé, P., Combes, F., Hamer, S., and Heywood, I. (2016). Star formation efficiency along the radio jet in Centaurus A. *A&A*, **586**, A45.
- Schiminovich, D., van Gorkom, J. H., van der Hulst, J. M., and Kasow, S. (1994). Discovery of Neutral Hydrogen Associated with the Diffuse Shells of NGC 5128 (Centaurus A). *ApJ*, **423**, L101.
- Schinnerer, E., Eckart, A., Tacconi, L. J., Genzel, R., and Downes, D. (2000a). Bars and Warps Traced by the Molecular Gas in the Seyfert 2 Galaxy NGC 1068. *ApJ*, **533**, 850–868.
- Schinnerer, E., Eckart, A., and Tacconi, L. J. (2000b). Distribution and Kinematics of the Circumnuclear Molecular Gas in the Seyfert 1 Galaxy NGC 3227. *ApJ*, **533**, 826–849.
- Schwarz, U. J. (1985). H I synthesis observations of the peculiar galaxy NGC 3718 and its companion NGC 3729. *A&A*, **142**, 273–288.
- Schweizer, F. (1980). An optical study of the giant radio galaxy NGC 1316 /Fornax A/. *ApJ*, **237**, 303–318.
- Schweizer, F. (1982). Colliding and merging galaxies. I - Evidence for the recent merging of two disk galaxies in NGC 7252. *ApJ*, **252**, 455–460.

- Sérsic, J. L. (1968). *Atlas de galaxies australes*.
- Shields, G. A., Rosario, D. J., Smith, K. L., Bonning, E. W., Salviander, S., Kalirai, J. S., Strickler, R., Ramirez-Ruiz, E., Dutton, A. A., Treu, T., and Marshall, P. J. (2009). The Quasar SDSS J105041.35+345631.3: Black Hole Recoil or Extreme Double-Peaked Emitter? *ApJ*, **707**, 936–941.
- Shlosman, I., Frank, J., and Begelman, M. C. (1989). Bars within bars - A mechanism for fuelling active galactic nuclei. *Nature*, **338**, 45–47.
- Sijacki, D., Springel, V., and Haehnelt, M. G. (2011). Gravitational recoils of supermassive black holes in hydrodynamical simulations of gas-rich galaxies. *MNRAS*, **414**, 3656–3670.
- Sparke, L. S. (1996). A Dynamical Model for the Twisted Gas Disk in Centaurus A. *ApJ*, **473**, 810.
- Sparke, L. S., van Moorsel, G., Schwarz, U. J., and Vogelaar, M. (2009). The Remarkable Warped and Twisted Gas Disk in NGC 3718. *AJ*, **137**, 3976–3992.
- Springel, V., Wang, J., Vogelsberger, M., Ludlow, A., Jenkins, A., Helmi, A., Navarro, J. F., Frenk, C. S., and White, S. D. M. (2008). The Aquarius Project: the subhaloes of galactic haloes. *MNRAS*, **391**, 1685–1711.
- Suzuki, R., Kudo, T., Hashimoto, J., Carson, J., Egner, S., Goto, M., Hattori, M., Hayano, Y., Hodapp, K., Ito, M., Iye, M., Jacobson, S., Kandori, R., Kusakabe, N., Kuzuhara, M., Matsuo, T., Mcelwain, M., Morino, J.-I., Oya, S., Saito, Y., Shelton, R., Stahlberger, V., Suto, H., Takami, H., Thalmann, C., Watanabe, M., Yamada, H., and Tamura, M. (2010). Performance characterization of the HiCIAO instrument for the Subaru Telescope. In *Society of Photo-Optical Instrumentation Engineers (SPIE) Conference Series*, volume 7735 of *Society of Photo-Optical Instrumentation Engineers (SPIE) Conference Series*.
- Thomas, D., Maraston, C., Bender, R., and Mendes de Oliveira, C. (2005). The Epochs of Early-Type Galaxy Formation as a Function of Environment. *ApJ*, **621**, 673–694.
- Toomre, A. (1977). Mergers and Some Consequences. In B. M. Tinsley and R. B. G. Larson, D. Campbell, editors, *Evolution of Galaxies and Stellar Populations*, page 401.
- Torrey, P., Snyder, G. F., Vogelsberger, M., Hayward, C. C., Genel, S., Sijacki, D., Springel, V., Hernquist, L., Nelson, D., Kriek, M., Pillepich, A., Sales, L. V., and McBride, C. K. (2015). Synthetic galaxy images and spectra from the Illustris simulation. *MNRAS*, **447**, 2753–2771.
- Tueller, J., Baumgartner, W. H., Markwardt, C. B., Skinner, G. K., Mushotzky, R. F., Ajello, M., Barthelmy, S., Beardmore, A., Brandt, W. N., Burrows, D., Chincarini, G., Campana, S., Cummings, J., Cusumano, G., Evans, P., Fenimore, E., Gehrels, N., Godet, O., Grupe, D., Holland, S., Kennea, J., Krimm, H. A., Koss, M., Moretti, A., Mukai, K., Osborne, J. P.,

- Okajima, T., Pagani, C., Page, K., Palmer, D., Parsons, A., Schneider, D. P., Sakamoto, T., Sambruna, R., Sato, G., Stamatikos, M., Stroh, M., Ukwata, T., and Winter, L. (2010). The 22 Month Swift-BAT All-Sky Hard X-ray Survey. *ApJS*, **186**, 378–405.
- Tully, R. B., Verheijen, M. A. W., Pierce, M. J., Huang, J.-S., and Wainscoat, R. J. (1996). The Ursa Major Cluster of Galaxies. I. Cluster Definition and Photometric Data. *AJ*, **112**, 2471.
- van Breugel, W., Filippenko, A. V., Heckman, T., and Miley, G. (1985). Minkowski's object - A starburst triggered by a radio jet. *ApJ*, **293**, 83–93.
- van Breugel, W. J. M. and Dey, A. (1993). Induced star formation in a radio lobe of 3C 285? *ApJ*, **414**, 563–572.
- Velazquez, H. and White, S. D. M. (1999). Sinking satellites and the heating of galaxy discs. *MNRAS*, **304**, 254–270.
- Vogelsberger, M., Genel, S., Springel, V., Torrey, P., Sijacki, D., Xu, D., Snyder, G., Nelson, D., and Hernquist, L. (2014a). Introducing the Illustris Project: simulating the coevolution of dark and visible matter in the Universe. *MNRAS*, **444**, 1518–1547.
- Vogelsberger, M., Genel, S., Springel, V., Torrey, P., Sijacki, D., Xu, D., Snyder, G., Bird, S., Nelson, D., and Hernquist, L. (2014b). Properties of galaxies reproduced by a hydrodynamic simulation. *Nature*, **509**, 177–182.
- Voigt, H.-H. (1988). *Abriß der Astronomie*.
- White, S. D. M. and Rees, M. J. (1978). Core condensation in heavy halos - A two-stage theory for galaxy formation and clustering. *MNRAS*, **183**, 341–358.
- Whitmore, B. C., Lucas, R. A., McElroy, D. B., Steiman-Cameron, T. Y., Sackett, P. D., and Olling, R. P. (1990). New observations and a photographic atlas of polar-ring galaxies. *AJ*, **100**, 1489–1522.
- Wild, W., Eckart, A., and Wiklind, T. (1997). Molecular excitation in Centaurus A: the $^{13}\text{C}^{18}\text{O}$ J=1-0 map and CO line ratios. *A&A*, **322**, 419–426.
- Zacharias, N., Finch, C. T., Girard, T. M., Henden, A., Bartlett, J. L., Monet, D. G., and Zacharias, M. I. (2013). The Fourth US Naval Observatory CCD Astrograph Catalog (UCAC4). *AJ*, **145**, 44.
- Zhang, X.-G., Dultzin-Hacyan, D., and Wang, T.-G. (2007). The size of broad-line regions of low-luminosity active galactic nuclei. *MNRAS*, **374**, 691–696.



List of Figures

- 1.1 Top: A brief history of the Universe from the Big Bang to the present day. Image credit: Rhys Taylor (Cardiff University). Bottom: The CMB temperature map from the WMAP experiment with a small region of it magnified to demonstrate how the initial CMB anisotropies result in the Cosmic Web. Image credit: Berkeley Lab. 2
- 1.2 The Hubble tuning fork. Galaxy evolution is implied if one attempts to “read” this figure from the right (late-type spiral galaxies) to the left side (early-type elliptical galaxies). Image credit: Sloan Digital Sky Survey (SDSS) 3
- 1.3 Top: A large Milky Way-like spiral galaxy has a disk $\sim 100,000$ light years across and it is very small compared to its DM halo (image from the Aquarius DM simulation [Springel et al. \(2008\)](#)). Middle: The DM halo of such a galaxy is very small compared to the large-scale cosmic web (image from the Bolshoi simulation [Klypin et al. \(2011\)](#)). Bottom: Real versus synthetic Hubble Space Telescope (HST) Ultra Deep Field from [Vogelsberger et al. \(2014b\)](#). Left: HST eXtreme Deep Field image with thousands of galaxies. Right: A similar sight-line through the Illustris Simulation of galaxy formation showing that current simulations produce galaxies with colors and shapes broadly similar to observed ones. 4
- 1.4 An illustration demonstrating how disk galaxies merge to form an elliptical galaxy. The entire formation process takes $\sim 2 - 3$ Gyr to complete. Image credit: P. Jonsson (Harvard-Smithsonian Center for Astrophysics, USA), G. Novak (Princeton University, USA), and T.J. Cox (Carnegie Observatories, Pasadena, Calif., USA). 6

1.5	Reproduction of figure 1 from Kormendy (2009) . Major-axis surface brightness profiles of Virgo ellipticals NGC4486 (left) and NGC4458 (right). The black curve indicates a Sérsic (1968) fit on the outer part of the profile (between the vertical black lines). NGC4486 is a core galaxy, since the fitted function on the outer profile overestimates the data when it is inwardly extrapolated, while NGC4458 is a coreless galaxy, since the inward extrapolation of the outer profile's fit underestimates the data in the inner region.	7
1.6	Adopted from Beckmann and Shrader (2012) . Graphical illustration of our current understanding of the AGN phenomenon. Under this unified scheme, the AGN type we observe is a strong function of the angle of our line-of-sight and the object's power output.	9
1.7	Top: Atmospheric opacity across the entire electromagnetic spectrum, indicating the wavelength regimes at which ground-based observations are possible. Image credit: NASA. Bottom: Atmospheric transparency windows in the NIR and MIR. The wavelength windows at which the atmosphere is largely transparent are marked with the corresponding filters names. Image credit: Allen (1975)	13
1.8	NACO/Very Large Telescope (VLT) <i>H</i> band images showing SgrA* in its quiescent (left) and variable states (right). The white circle indicates the position of SgrA*. Image credit: Genzel et al. (2003)	14
1.9	Comparison of an optical and a NIR HST image, a perfect example of the NIR imaging potential for studying primordial galaxies. Image credit: NASA/ESA/STScI	14
1.10	A graphical illustration of an AO system. Image credit: ESO	16
1.11	Left: The GC without the use of the AO system. Right: The GC and the location of the SMBH (labeled SgrA*) with the use of the AO. Image credit: Keck Observatory/UCLA GC Group.	16
2.1	An 9.5×4.5 arcmin of NGC3718 from the SDSS survey (<i>gri</i> composite image).	20
2.2	20×20 arcsec ² reduced <i>K_S</i> band image with the sky component (left) and the sky frame that was generated from the <i>K_S</i> band image (right). Similar sky frames were generated and subtracted from the <i>J</i> and <i>H</i> band images.	23
2.3	Sky subtracted <i>J</i> (top left), <i>H</i> (top right), and <i>K_S</i> (bottom middle) band images.	23
2.4	X (left column) and Y (right column) central coordinates indicated by the fitted ellipses versus their SMAs for the <i>K_S</i> (red/top row), <i>H</i> (blue/middle row), and <i>J</i> (green/bottom row) bands. The shaded elliptical regions indicate the most prominent stable values used for the derivation of the first order approximation photo-centers of NGC3718.	26
2.5	Residual images– from the pivot and subtract operation– for the <i>J</i> (top left), <i>H</i> (top right), and <i>K_S</i> (bottom middle) bands. All images are smoothed with a 10-pixel Gaussian kernel. The mean peak residual fluxes as percentages of NGC3718's mean peak fluxes are $\sim 4.5\%$, $\sim 3.0\%$, and $\sim 3.4\%$ for the <i>J</i> , <i>H</i> , and <i>K_S</i> bands, respectively.	28

- 2.6 Examples of smoothed residual H band images after rotation around pivot points shifted by $(X_{center}^{init} - 0.5, Y_{center}^{init} + 0.5)$ (upper left), $(X_{center}^{init} + 0.5, Y_{center}^{init} + 0.5)$ (upper right), $(X_{center}^{init}, Y_{center}^{init})$ (center), $(X_{center}^{init} - 0.5, Y_{center}^{init} - 0.5)$ (lower left), and $(X_{center}^{init} + 0.5, Y_{center}^{init} - 0.5)$ (lower right). 29
- 2.7 Symmetrical light images– after the removal of the residuals– for the J (top left), H (top right), and K_S (bottom middle) bands. 30
- 2.8 The $H - K_S$ (top) and $J - H$ (bottom) NIR color maps. 33
- 2.9 Radial profiles of the $H - K_S$ (two left hand panel plots) and $J - H$ (two right hand panel plots) color maps. Measurements are performed along two perpendicular sets of directions measured counterclockwise from the north, namely, $120^\circ/210^\circ$ (blue and red points, respectively - upper row) and $170^\circ/260^\circ$ (green and magenta points, respectively - lower row). Negative→positive relative offset represents a S(E,W)→N(W,E) direction. 35
- 2.10 Top: Closeup of the $H - K_S$ map. The contours of the red blob (in red) are offset from the peak contours of the symmetrical $H - K_S$ map (in blue). Bottom: Closeup of the high pass filtered K_S band image. The peak flux of the image is offset from the K_S band photo-center. In both images, the red circle marks the peak of the offset red blob, while the blue circle marks the center of the underlying stellar bulge. Finally, the radii of the blue and red circles represent their positional uncertainties, namely, ~ 7 mas, while the yellow(top)/cyan(bottom) line represents the displacement of the offset, namely, ~ 50 mas. 36
- 2.11 The model of mixtures from [Glass and Moorwood \(1985\)](#). Moving away from the open black circle at $J - H = 0.78$ and $H - K = 0.22$ (i.e. ordinary galaxy colors) and along the horizontal lines in the grid of mixtures, indicates an increase (by 10% per vertical line) in the percentage of contribution from hot dust emission, while moving along the vertical lines of the model reflects an increase in the temperature of this dust component in the range $T \sim 500 - 1500$ K. 37
- 2.12 The e-Merlin 6 cm radio map. The third innermost contour represents the $\sim 40 - 50\%$ of the peak flux, while the outer contours ($\sim 4\sigma$ above the local background) represent $\sim 2 - 3\%$ of the peak flux. The size of the beam is shown in the upper left corner, while the red and blue dashed lines indicate the position angles of the SE-NW and the NE-SW small-scale candidate bipolar extended structures, respectively. 38
- 2.13 The 6 cm e-Merlin radio contours over-plotted on a copy of the upper image of figure 2.10. The radii of the blue and red circles represent the uncertainties of each position, namely, ~ 7 mas, while the black dashed ellipse represents the total coordinates uncertainty shown in table 2.2. (Note: This is the position of the radio emission quoted in table 2.2. The same image with the position quoted in [Krips et al. \(2007\)](#) is shown in appendix D, figure D.1). 39

- 2.14 First figure: The K_S band surface brightness profile versus the logarithm of the radius ($\log(R)$) in units of pc. The blue dashed line shows the inwardly extrapolated Sérsic profile of the bulge component, while the black dashed line shows the dual exponential disk component. The red and blue points indicate the Subaru K_S and 2MASS K_S data, respectively. Second figure: Same as the first figure, but with the different components added. In this case the black points represent the joined Subaru/2MASS data set, while the red dashed line represents the combined fitted model. Third figure: The K_S band surface brightness profile versus radius (R) in units of arcsec for the innermost ~ 3 arcsec, while the red dashed line (again) indicates the combined fitted model. Fourth figure: Same as the third figure, but showing the complete data range up to ~ 70 arcsec. The green lines show the uncertainties of the data points. 44
- 2.15 The $A4$ parameter of NGC3718 plotted as a function of radius R (in units of arcsec), for the K_S (red/top), H (blue/middle), and J (green/bottom) bands. The dashed black line shows the transition from disk to boxy galaxies. 47
- 2.16 Reproduction of figure 10e from [Ho et al. \(1997b\)](#), showing a part of the optical spectrum of NGC3718. The broad (indicated by the blue solid line) and the narrow (indicated by the red solid line) $H\alpha$ emission lines show a clear relative shift, indicating a motion of the BLR with respect to the NLR. 49
- 2.17 Six snapshots of the different evolutionary stages of the two polar ring galaxy formation scenarios adopted from [Bournaud and Combes \(2003\)](#). The merging scenario is shown in the six left hand panels, while the accretion scenario is shown in the six right hand panels. 53
- 3.1 Left: Reproduction of figure 1 from [Oosterloo and Morganti \(2005\)](#). Overplotted on an optical image of NGC5128 can be seen a) the HI cloud (black contours), b) the centimeter radio jet (white contours), c) and the filaments of ionized gas (black ellipses). The approximate position of the HST field ([Mould et al., 2000](#)) is shown by the red outlined region. Right: The green dashed rectangle represents the Subaru field, while the yellow lines on the HST $F555W$ image approximately indicate the positions of the OB associations. 60
- 3.2 The final, $\sim 20 \times 18$ arcsec² Subaru J (top left), H (top right), and K_S (bottom middle) images. 62
- 3.3 HST $F555W$ (left) and $F814W$ (right) images. This HST FoV is equivalent to the FoV of the Subaru J , H , and K_S band images ($\sim 20 \times 18$ arcsec²). The three colored circles indicate the positions of the brighter stars on the HST $F814W$ field. The A HST star (green circle) is the brightest, the B HST star (red circle) is the second brighter, and the C HST star (yellow circle) is the third brighter. . . . 64
- 3.4 Low-pass filtered with a 10 pixel Gaussian kernel Subaru J (top left), H (top right), K_S (bottom left), and the JHK_S composite (bottom right) images. The expected positions of the three brighter stars on the HST $F814W$ field are marked by the three colored circles. The statistics region is outlined by the $\sim 5 \times 7$ arcsec² yellow box. 65

3.5	Top: The $> 3\sigma$ signal at the (zoomed-in) expected position of the A HST star on the three Subaru NIR bands, namely, J (left), H (middle), and K_S (right). Bottom: A $\sim 20 \times 9$ arcsec ² region of the JHK_S composite image, in which the statistics region is outlined by the $\sim 5 \times 7$ arcsec ² yellow box. All images are clipped at 3σ above the background (blue background).	66
3.6	The Visual-NIR CMD of figure 3 from Gullieuszik et al. (2008) . The BSGs (in diamond symbols), RSGs (in triangles), RGB (in squares), and AGB (in filled circles) stars of UKS 2323-326 are shown. The three (red, green, and blue) shaded areas show the equivalent stellar sequences (see figure 12 of Rejkuba et al. (2001)) of NGC5128. The three colored (green, red, and yellow) points and their error bars show the positions of the A, B, and C HST stars, respectively, and their corresponding photometric uncertainties on the CMD. The green (dashed), the red (dashed-dotted), and the yellow (solid) lines show example isochrones (Bertelli et al., 2009) for the median ages of the three HST stars. Finally, the black solid line shows the Subaru K_S band limiting magnitude.	74
A.1	Examples of raw images of NGC3718 (top left), Cen A (top right), sky (Cen A data set – bottom left), and flat-field (bottom right) from the HiCIAO instrument, in which the 32-strip noise pattern and the bad pixels are clearly visible.	84
A.2	Examples of a BPM (left) and a 32-strip noise pattern (middle) used to correct all the raw images and an example of a corrected sky image (Cen A data set – right).	84
A.3	An example of the final image of NGC3718 (without the sky subtracted – left) and of Cen A (right).	85
B.1	The 2MASS K_S band image of NGC3718. Over-plotted are the 1) SDSS r band ($\sim 0.6 \mu\text{m}$) contours in green, 2) 2MASS K_S band contours in red, 3) Subaru K_S band contours in yellow, and 4) distance (blue dashed line, length ~ 3.5 arcsec) of the optical/NIR peak flux positions to the beginning of the dust lane (white dashed box).	87
C.1	The SDSS z band image of NGC3718. Over-plotted are the 1) SDSS z band contours in yellow and 2) Subaru J band contours in red. The black dashed ellipse and the blue dashed line mark the central ~ 4 arcsec of NGC3718, indicating the symmetry of the SDSS z band contours in this region.	89
D.1	Identical to figure 2.13, but with the radio map position calculated based on the old/outdated position of the phase reference source. This is equivalent to the peak radio position reported by Krips et al. (2007)	91



List of Tables

2.1	First order approximation photo-centers.	26
2.2	Astrometric uncertainties and coordinates.	32
2.3	E-E dichotomy parameters.	48
3.1	NIR and Visual-NIR colors.	69
3.2	Parameters for the B and C HST stars.	71



Acronyms

2MASS – Two Micron All-Sky Survey

AGB – Asymptotic Giant Branch

AGN – Active Galactic Nucleus

AIPS – Astronomical Image Processing System

AO – Adaptive Optics

APD – Avalanche Photodiode

BLR – Broad Line Region

BLRG – Broad Line Region Galaxy

BPM – Bad Pixel Mask

BSG – Blue Supergiant

Cen A – Centaurus A

CMB – Cosmic Background Radiation

CMD – Color-Magnitude Diagram

Dec – Declination

DIM – Direct Imaging Mode

DM – Dark Matter

ELT – Extremely Large Telescope

e-Merlin – Multi-Element Radio Linked Interferometer Network

EVN – European VLBI Network

FIR – Far-Infrared

FORS1 – Focal Reducer and Spectrograph

FoV – Field of View

FR-I – Fanaroff-Riley type I

FWHM – Full Width Half Maximum
GALEX – Galaxy Evolution Explorer
GC – Galactic Center
G.S.1 – SE Guide Star
G.S.2 – NW Guide Star
G.S. – unresolved Guide star
HCSS – Hyper Compact Stellar System
HgCdTe – Mercury Cadmium Telluride
HiCIAO – High-Contrast Coronagraphic Imager for Adaptive Optics
HR – Hertzsprung-Russell
HST – Hubble Space Telescope
IF – Intermediate Frequency
IGM – Intergalactic Medium
IMF – Initial Mass Function
IRAF – Image Reduction and Analysis Facility
IRAS – Infrared Astronomical Satellite
IR – Infrared
IRSA – Infrared Science Archive
ISAAC – Infrared Spectrometer And Array Camera
ISM – Interstellar Medium
ISO – Infrared Space Observatory
IST – Intermediate Spectral Type
 Λ CDM – Λ Cold Dark Matter
LG – Local Group
LINER – Low Ionization Nuclear Emission Line Region
LLAGN – Low Luminosity Active Galactic Nucleus
MAD – Multi-conjugate Adaptive optics Demonstrator
MIR – Mid-Infrared
NACO – NAOS-CONICA
NED – NASA/IPAC Extragalactic Database
NE – North-East
NIR – Near-Infrared
NLRG – Narrow Line Region Galaxy
NLR – Narrow Line Region
NML – Northern Middle Lobe
NUGA – NUclei of GALaxies
NW – North-West
PA – Position Angle
PDMF – Present Day Mass Function
PSF – Point Spread Function
QSO – Quasi-Stellar Object
RA – Right Ascension
RGB – Red Giant Branch

RSG – Red Supergiant
SDSS – Sloan Digital Sky Survey
SE – South-East
SMA – Semi-Major Axis
SMBH – Supermassive Black Hole
SNR – Signal-to-Noise Ratio
STR – Spectral Type Range
SW – South-West
UV – Ultraviolet
VLA – Very Large Array
VLBA – Very Long Baseline Array
VLT – Very Large Telescope
WISE – Wide-field Infrared Survey Explorer
YSG – Yellow Supergiant
ZP – Zero Point



Acknowledgements

This work was supported by the Max Planck Society and the University of Cologne through the International Max Planck Research School (IMPRS) for Astronomy and Astrophysics, as well as, in part, by the Deutsche Forschungsgemeinschaft (DFG) via grant SFB 956.

I would like to thank my supervisors, Prof. Dr. Andreas Eckart, Prof. Dr. J. Anton Zensus, and Dr. Emmanouil Angelakis, for giving me the opportunity to fulfill this dream and for the guidance and support they generously provided throughout the duration of my PhD studies.

This work would not be possible without the data taken with the Subaru telescope. I would like to thank the Subaru operation team, as well as, the HiCIAO instrument team for their generous support.

For the work presented in chapter 2, I would like to thank Prof. Dr. David Merritt for the enlightening discussions that helped me forge a better understanding of the nuclear dynamics of NGC3718. I would like to thank the anonymous referees for the fruitful comments that helped me clarify the description of the methods used in this work. I would like to thank the Merlin operation team and Dr. Jens Dierkes for providing and processing the 6 cm e-Merlin data, respectively. I would like to thank Prof. Dr. Andreas Eckart, Prof. Dr. Shogo Nishiyama, Prof. Dr. Thomas Muxlow, Prof. Dr. J. Anton Zensus, Dr. Jens Dierkes, Dr. Silke Britzen, Dr. Macarena García-Marín, and Dr. Matthew Horrobin for their crucial scientific advice and feedback on this project. Finally, I would like to thank Prof. Dr. Alister Graham for the fruitful discussions on the results of this work.

For the work presented in chapter 3, I would like to thank Prof. Dr. Andreas Eckart, Prof. Dr. Shogo Nishiyama, Prof. Dr. Lucas Labadie, Prof. Dr. J. Anton Zensus, Dr. Norberto Castro, Dr. Álvaro Sánchez-Monge, and Dr. Silke Britzen for their crucial scientific advice and feedback on this project. Finally, I would like to thank Ass. Prof. Dr. Elias Tsakas and M.Sc. Christos Christou for their feedback on the mathematical framework of this work.

I would like to thank our secretaries, Tanja Bodendorf, Stefanie Krämer, Bettina Krause, Dr. Petra Neubauer-Guenther, and Dr. Simone Pott, for keeping everything working “like a clock” and solving any problems that I faced during those three years.

All my studies so far would not have been possible without the support of my parents Kate and Haris and my grandparents Ioannis and Fotini, to whom I am deeply grateful for all the years of believing in me, for all their unconditional love, and for the principles by which they raised me. I love you so much!! Especially, I would like to dedicate this thesis to my beloved grandmother Stella, who passed away as those lines were being written. Rest In Peace...I will always remember you...;(

I would like to deeply thank all the members of the aegroup, with whom we shared all the stressful, beautiful, and creative moments. I would like to specially thank my office-mates: Gerold, Banafsheh, Marcus, and Balaji for having the best office in the building...;)...Angela and Silvia thank you very much for all the crucial help and info upon my arrival to Germany...Many thanks to Nadeen for providing the template for this thesis and crucial assistance in many more aspects...Lukas thank you very much for the translation of the abstract...Rebekka thank you very much for all the help with the bureaucracy...I would still be struggling with all the problems if you weren't there...:D...To my Iraqi friend Yasir: We will smoke Shisha again one day...;)...Special thanks to my mate Abhijeet for all the fun and discussions we had during those three years...and of course to my beloved cats Lucy and Sniarf for keeping me company during all the cold, German nights of endless work...miaow and pouring sweeties...:D

A big thank you to Christos, Maria, Ilias, Giannis, Vassilis, Ioannis, and Xenia for making the PhD experience in Germany often “feel like home”...;)

Finally, I big thank you, a bigger hug, and a huge kiss to Maria for all her love and support in all levels. You know why, don't you?...;)

Below is the permission granted by the A&A Editorial Office for reprinting the material of Chapter 2.

Astronomy and Astrophysics

Editor in Chief: T. Forveille

T. Forveille

Astronomy & Astrophysics
Observatoire de Paris
61, avenue de l'Observatoire
75014 Paris, France

Tel.: 33 0(1) 43 29 05 41
Fax: 33 0(1) 43 29 05 57
e-mail: aanda.paris@obspm.fr
Web: <http://www.aanda.org>

merging
Annales d'Astrophysique
Arkiv for Astronomi
Bulletin of the Astronomical Institutes
of the Netherlands
Bulletin Astronomique
Journal des Observateurs
Zeitschrift für Astrophysik
Bulletin of the Astronomical Institutes
of Czechoslovakia

Paris, May 12, 2016

Reprint Permission

Material:

All tables and figures in Markakis et al. 2015, A&A, 580, A11

To be used in:

PhD thesis, University of Cologne

Permission granted to:

Konstantinos Markakis
markakis@ph1.uni-koeln.de

I hold copyright on the material referred to above, and hereby grant permission for its use as requested herewith. The credit should be given as follows:

Credit: Author, A&A, vol, page, year, reproduced with permission © ESO.



Thierry Forveille
A&A Editor-in-Chief



Erklärung

Ich versichere, daß ich die von mir vorgelegte Dissertation selbständig angefertigt, die benutzten Quellen und Hilfsmittel vollständig angegeben und die Stellen der Arbeit – einschließlich Tabellen, Karten und Abbildungen –, die anderen Werken im Wortlaut oder dem Sinn nach entnommen sind, in jedem Einzelfall als Entlehnung kenntlich gemacht habe; daß diese Dissertation noch keiner anderen Fakultät oder Universität zur Prüfung vorgelegen hat; daß sie – abgesehen von unten angegebenen Teilpublikationen – noch nicht veröffentlicht worden ist sowie, daß ich eine solche Veröffentlichung vor Abschluß des Promotionsverfahrens nicht vornehmen werde. Die Bestimmungen dieser Promotionsordnung sind mir bekannt. Die von mir vorgelegte Dissertation ist von Prof. Dr. Andreas Eckart betreut worden.

Köln, 31.08.2015

Teilpublikationen

Markakis, K., Dierkes, J., Eckart, A., Nishiyama, S., Britzen, S., García-Marín, M., Horrobin, M., Muxlow, T. and Zensus, J. A.

Title: *Subaru and e-Merlin observations of NGC3718. Diaries of a supermassive black hole recoil?* 2015A&A, **580A**, 11M.

Markakis, K., Eckart, A., Castro, N., Labadie, L., Sánchez-Monge, Á., Nishiyama, S., Britzen, S., and Zensus, J. A.

Title: *High resolution observations of Cen A: Supergiants in a region of jet-induced star formation?* In preparation.

Weitere Publikationen

Eckart, A., Valencia-S., M., Shahzamanian, B., Garcia-Marin, M., Peissker, F., Zajacek, M., Parsa, M., Jalali, B., Saalfeld, R., Sabha, N., Yazici, S., Karssen, G. D., Borkar, A., Markakis, K., Zensus, J. A. and Straubmeier, C.

Title: *The Center of the Milky Way from Radio to X-rays*. arXiv1501.02164, 2015.

Eckart, A., Horrobin, M., Britzen, S., Zamaninasab, M., Mužić, K., Sabha, N., Shahzamanian, B., Yazici, S., Moser, L., García-Marin, M., Valencia-S., M., Borkar, A., Bursa, M., Karssen, G., Karas, V., Zajaček, M., Bronfman, L., Finger, R., Jalali, B., Vitale, M., Rauch, C., Kunneriath, D., Moultaqa, J., Straubmeier, C., Rashed, Y. E., Markakis, K. and Zensus, A. Title: *The infrared K-band identification of the DSO/G2 source from VLT and Keck data*. IAU Symposium, vol. 303, 2014.

Eckart, A., Britzen, S., Horrobin, M., Zamaninasab, M., Muzic, K., Sabha, N., Shahzamanian, B., Yazici, S., Moser, L., Zuther, J., Garcia-Marin, M., Valencia-S., M., Bursa, M., Karssen, G., Karas, V., Jalali, B., Vitale, M., Bremer, M., Fischer, S., Smajic, S., Rauch, C., Kunneriath, D., Moultaqa, J., Straubmeier, C., Rashed, Y. E., Iserlohe, C., Busch, G., Markakis, K., Borkar, A. and Zensus, A. J.

Title: *The Galactic Center as a paradigm for low-luminosity nuclei? What can be learned from SgrA* for the central engine and conditions of star formation in nuclei of Seyfert galaxies and low luminosity nearby QSOs; The K-band identification of the DSO/G2 source from VLT and Keck data*. arXiv1311.2743, 2012.

Lebenslauf

Persönliche Angaben

Name: Konstantinos Markakis
Anschrift: I. Physikalisches Institut, Universität zu Köln
Zülpicher Str. 77, 50937 Köln
Email: markakis@ph1.uni-koeln.de
Geburtsdatum und -ort: 18.06.1983 in Athen, Griechenland
Staatsangehörigkeit: Griechisch

Ausbildung und Berufserfahrung

2001 - 2007 Bachelor der Physik, Institut für Physik,
Universität von Kreta, Heraklion, Griechenland
2007-2008 Militärdienst
2008 - 2011 Master der Physik, Institut für Physik, National &
Kapodistrian Universität Athen,
Sektor der Astrophysik, Astronomy & Mechanics,
Titel:
“Variability of young massive stars in the Arches Cluster”,
Athen, Griechenland
2010 - 2012 Nationales Observatorium Athen
2012 - 2015 Promotionstudent an der Universität zu Köln und dem
Max Planck Institut für Radioastronomie
wiss. Betreuer: Prof. Dr. Andreas Eckart

Stipendium und Auszeichnungen

2012- 2014 Stipendium der
International Max Planck Research School (IMPRS)
und der *Max Planck Institut für Radioastronomie (MPIfR)*,
an der Universität zu Köln